Università degli Studi Roma TRE

e

Consorzio Nazionale Interuniversitario per le Scienze Fisiche della Materia

Dottorato di Ricerca in Scienze Fisiche della Materia
XXVI ciclo

"Experimental Study of the Phase Behaviour of Limited Valence Particles in DNA Nano-Aggregate Systems"

Tesi di dottorato della dott.ssa Francesca Bomboi

Relatore
Prof. Francesco Sciortino

Coordinatore Dottorato
Prof. Settimio Mobilio

a. a. 2012/2013

Contents

List of Figures

Introduction

"Begin at the beginning - the
King said, very gravely, - and go on
till you come to the end: then stop"
Lewis Carrol

"This structure has novel features which are of considerable biological interest". With these words, appeared in a scientific paper on the 25th of April 1953 [1], J.D. Watson and F.H.C. Crick announced to the world the discovery of the structure of DNA, the *molecule of life*.
Nine years later, in October 1962, they shared the Nobel Prize in Physiology or Medicine with M. Wilkins, for having solved one of the most crucial of all the biological puzzles. More than half a century later, relevant new implications of this outstanding scientific contribution are still emerging.
In particular, the DNA capability to hybridize in a specific and reversible fashion, due the complementarity of the nitrogen bases, well defined by the Watson and Crick pairing rules, has nowadays opened the way to an innovative field of science: structural DNA nanotechnology [2, 3].
The exploitation of DNA for material purposes constitutes a new chapter in the history of the molecule. Indeed, after the pioneering work of Nadrian Seeman in 1982 [4], there has been a progressive shift from the classical vision of DNA as a biological gene-encoding molecule to a much more innovative point of view, regarding DNA as a building block of considerable nanotechnological relevance. In fact, the specific binding between complementary DNA bases, which provides the biochemical groundwork for genetics, can be exploited as a potent molecular recognition system to guide and control the assembly of highly structured materials with precise nanoscale properties.
Moreover, the nanometric dimensions of DNA, with a diameter of around 2 nm, its short structural repeat, with a helical pitch of around 3.5 nm and its very high stiffness, with a persistence length of approximately 50 nm in its double-helical conformation, make it appealing for nanotechnological purposes also from structural standpoints.
For all these reasons, in the last years, there has been an unprecedented development in DNA-based nanotechnology: a rich variety of nanosized objects, such as geometric shapes, hollow capsules and nanomachines, as well as more complex mesoscopic and macroscopic structures with different forms and functionalities has been intelligently assembled via the rational design of specific DNA sequences [5, 6, 7, 8, 9, 10, 11, 12].

Besides the practical implications that these new materials might have, the achievement of such a high level of control on the programmed self-assembly of matter demonstrates the vast horizons opened by the possibility of building with DNA, which appear to be limited only by human imagination.
In this work, following the lines set by structural DNA nanotechnology, we introduce a new and challenging twist: DNA nano-constructs as man-designed particles to experimentally explore unconventional phase behaviours conceived so far only in charta and in silico [13, 14, 15].
In our view, DNA can be seen as a powerful tool to explore statistical physics because it enables to produce, via self-assembly, bulk quantities of identical particles with controlled mutual interactions.
As a proof of concept, we focus here on the phase behaviour of limited-valence particles (i.e. colloidal particles with a small controlled number of possible bonding opportunities), a topic which has received a considerable interest in the last few years [16], but which has so far been confined to theoretical and numerical investigations.
These investigations predict that a solution of such particles should exhibit phase coexistence, the colloidal analog of the gas-liquid coexistence in simple liquids, thus presenting a critical point, characterized by a critical temperature and a critical density.
The location of the unstable region in the temperature-concentration (T − c) plane is predicted to be significantly affected by the valence, i.e. by the number of bonds that each particle can form.
Specifically, reducing the valence should lower both the critical temperature and the critical concentration, thus shrinking the region in the T − c plane where the system is unstable with respect to concentration fluctuations.
An indirect support to these theoretical predictions comes from recent experiments [17], which have interpreted the irreversible aging dynamics of a synthetic clay, laponite, as an equilibrium gelation process [18] appealing to an effective (although unknown) limited valence of the clay particles.
However, despite such promising findings, the absence of a methodology for creating bulk quantities of particles with reversible interactions and with controlled valence has until now prevented the experimental investigation of the systematic dependence of the coexistence region on the valence.
For these reasons, we decided to exploit the selectivity of DNA binding to simultaneously realize soft particles as well as to control the inter-particle interactions.
Specifically, we realized star-shaped DNA particles (nanostars) having three or four double-helical arms, each one ending with a sticky single-strand overhang designed on purpose to provide controllable and reversible interactions between individual particles.
Therefore, in our view, such DNA nanostars can be considered as limited-valence particles, whose valence f is determined by the number of the arms.
Being the binding between sticky overhangs stronger than the other inter-particle interactions (excluded volume, van der Waals, electrostatic), these constructs represent an optimal model for highlighting the role of the valence and closely mimic the investigated theoretical model.

Besides offering the remarkable possibility of realizing bulk quantities of particles with limited valence, our approach provides a strong control over their mutual interactions, since the cohesion between the sticky terminals can be easily tuned at will by changing the temperature of the system.
The possibility of regulating the valence of the particles together with the chance of finely tuning their interactions in a reversible and controlled fashion by simply aging on the temperature provide the unprecedented opportunity of experimentally investigating novel scenarios, such as equilibrium gelation processes.
Indeed, according to numerical predictions [18], equilibrium gelation is achieved when colloidal systems are able to form stable particle networks through a series of equilibrium states without the interference of phase separation. This can be easily realized when, as in the case of our limited-valence particles, a mechanism for shifting the phase separation (and hence the critical point) to low temperatures and densities is at hand. In this situation, in fact, at low-intermediate densities, almost-ideal gel states may become experimentally accessible through a careful equilibration procedure down to very low temperatures.
Further to the remarkable prospect of exploring the eventual formation of equilibrium gels, an additional important advantage offered by our self-assembling DNA nanostars is given by their subtle sensitivity to the ionic strength. Indeed, it is known that the ionic strength of the medium affects the binding-unbinding equilibrium of the DNA strands, by modifying their bonding free energy.
Therefore, the ability to modulate the binding temperature of the overhangs with salt offers the outstanding chance of directly investigating the role of the lifetime of the sticky bonds on the dynamic behaviour of the systems.
In the specific case of limited-valence nanostars here addressed, such possibility, conjointly with the ability of tuning the binding selectivity, the strength of interaction and the valence, set the basis to predict the thermal and kinetic stability of self-assembled DNA hydrogels.
From an applicative standpoint, a similar finding has numerous and remarkable implications. For instance, being our self-assembling DNA nanostars non toxic and easily biodegradable, the gelation process could allow materials (such as drugs or proteins) to be encapsulated within the gel matrix, thus providing an innovative and effective route for drug-delivery.
Therefore, besides representing the ideal candidates to experimentally investigate open issues of statistical mechanics, our star-shaped DNA particles can be also exploited for applicative purposes, involving the design and realization of commercial complex fluids with specifically customized properties.

Thesis outline

The main aim of this work is the experimental determination of the phase diagram of solutions of DNA nanostars with limited valence, in order to test the aforementioned theoretical predictions on the phase behaviour of reduced valence systems.
Specifically, in the present thesis, we mainly focus on the behaviour of $f = 3$ nanostars. Indeed, since the project is carried out in collaboration with the research group of Prof. T. Bellini (Complex Fluids and Molecular Biophysics Lab, Department of Medical Biotechnology and Translational Medicine, University of Milan), who started the investigation of $f = 4$ systems, from the comparative analysis of the experimental results obtained on both systems we can reasonably achieve a comprehensive panorama of the phase behaviour of particles with well-defined and controlled valence.
Moreover, once determined the phase diagram for solutions of $f = 3$ nanostars, and thus located the region of thermodynamics instability at low temperatures, we also aim at investigating the dynamics of equilibrium gels and its eventual dependence on the ionic strength of the solutions.
In the following we report a detailed scheme of the present dissertation, providing a brief overview on the main topics that we will address in each chapter.

This thesis is divided in three main parts:

- in the first one we depict the theoretical framework encompassing our study;
- in the second one we describe the experimental techniques used to investigate the system;
- in the third one we present the experimental data, providing a comprehensive discussion of the obtained results.

Here is a complete list of the chapters:

1. Limited-valence colloids.
   The first chapter introduces colloidal particles, showing how they can be used to mimic the behaviour of atomic systems. Anyhow, the emphasis is on a specific class of colloids, i.e. those characterized by reduced valence, which are the protagonists of the present study. Moreover, in this chapter, we address the important issue of colloidal gelation, introducing fundamental concepts such as equilibrium gels and empty liquids.

2. DNA nano-constructs.
   In the second chapter we describe in details the physicochemical properties of DNA, particularly emphasizing the peculiarities which make it appealing for nanotechnological purposes. Furthermore, we provide a brief overview on structural DNA nanotechnology, illustrating its basic principles and showing how DNA can be exploited to design and experimentally realize a large variety of all-DNA superstructures, ranging from crystals to hydrogels.

3. Methods.
   Due to the intrinsic complexity of biological soft matter, a systematic investigation of its structure and dynamics usually requires the concomitant use of a large variety of complementary experimental techniques. In the third chapter we thus present the basic principles of the different experimental methods that we used to investigate the system, with a particular emphasis on Dynamic Light Scattering measurements, which represent the large body of our experimental studies.

4. Design and preliminary investigation of DNA nanostars.
   Chapter 4 focuses on the preparation and on the first characterization of our $f = 3$ DNA nanostars, which was done through the use of various experimental techniques, i.e. Gel Electrophoresis, UV absorption and Atomic Force Microscopy.

5. DNA goes critical.
   In this chapter, we report the results of the experimental investigation performed to determine the phase diagram for the $f = 3$ nanostars. Moreover, we also discuss the critical dynamics of such system, which was deeply investigated through a series of Dynamic Light Scattering measurements performed upon cooling the system along the critical isochore.

6. Salt effects on the nanostar dynamics.
   In the last chapter, we present a study of the ionic strength effect on the gelation process of $f = 3$ nanostars. Specifically, we address the issue of whether the ionic strength of the solutions may play an effective role on the rupture of the sticky bonds between different nanostars, thus allowing for the possibility of finely tuning their lifetime. To this aim, we present the results of a systematic light scattering investigation performed on high-density DNA samples.

Part I

Limited-valence DNA nanoconstructs

Chapter 1

Limited-valence colloids

"No matter what anybody tells you,
words and ideas can change the world"
Prof. Keating, Dead Poets Society

Colloidal dispersions are heterogeneous systems in which particles of solid or droplets of liquid with dimensions ranging from nanometers to micrometers are dispersed in a liquid medium.
An interesting class of colloids which has recently captured a lot of interest is the one represented by *patchy* colloids. From a theoretical standpoint, they can be seen as a general category of particles with strongly anisotropic, highly directional interactions given by short-range attractive spots, *patches*, located on their surface [19].
The discrete number of patches on the surface defines the valence f of the particles, i.e. the maximum number of nearest neighbours that each particle can bond. Reducing the valence, i.e. limiting the possibility of forming bonds with neighbouring particles, gives rise to unusual collective behaviours in patchy particle systems, which are illustrated in the present chapter.
As a starting point, in the first section we introduce colloidal particles, showing why they can be used as a model to reproduce the behaviour of atomic systems and to understand important mechanisms in soft matter such as phase transitions or dynamical arrest processes. Subsequently, we provide a brief overview on patchy colloids, aimed at introducing their peculiar properties and their potential relevance in the rational self-assembly of predictable and ordered structures.
Moreover, at the end of the first section, we illustrate colloidal gelation, introducing important issues such as equilibrium gels and empty liquids.
Eventually, in the second section, we focus on limited-valence particles addressing the key role played by the functionality of the particles on the phase behaviour of reduced-valence systems.

1.1 Colloidal systems

The term 'colloids' derives from the Greek words *kolla eides* (meaning "glue-form" materials) and was introduced in the 19th century by T. Graham to describe a large class of materials consisting of two separate phases: a dispersed phase composed of mesoscopic particles, with characteristic sizes ranging from nanometers to micrometers, and a continuous phase, whose particles have typical atomic length scales.
Colloids are ubiquitous in everyday life since they are involved in many applications of soft materials, spanning from cosmetics to drug delivery systems. Familiar examples of colloidal dispersions include industrial and domestic materials such as inks or foams, food products such as ketchup or ice-cream and biological fluids such as blood or milk. Due to their massive presence in daily life, their thermodynamic and dynamic properties are currently the focus of numerous investigations in a wide range of research areas, ranging from physics to biology and chemistry.

1.1.1 Colloids as superatoms

In physics, colloids can be used as model system for atoms since many of the forces that dictate the structure and behaviour of matter (e.g. van der Waals interactions, electrostatic forces, excluded volume interactions) dictate also the structure and behaviour of colloidal dispersions. Moreover, owing to their large length scales and slow time scales, their behaviour can be easily monitored via table-top experiments, which are able to provide deep insights into processes that are not handily investigable in atomic systems. For instance, the typical length scales of colloidal dispersions are comparable to the wavelength of the light: light-scattering is thus a powerful method for studying the structure as well as the dynamics of colloidal systems. Moreover, micron-scale colloids are large enough to be easily observed using optical techniques (e.g. confocal microscopy), thus offering the advantageous possibility of monitoring the individual motion of each particle in the system.
In this respect, colloids can be considered as model "superatoms" and, for such reason, spherically-interacting colloidal particles have been extensively investigated in the last years to enhance the understanding of important mechanisms in soft matter such as gelation, crystallization and glass transition [18, 20, 21].
In addition, the favorable possibility of tuning the interactions between particles makes colloidal systems extremely appealing for exploring unconventional phase behaviours. Indeed, unlike atomic and molecular system where the interactions are fixed by the electronic structure, colloidal interactions can be tuned at will by simply changing macroscopic parameters such as the ionic strength of the medium or the temperature. Consequently, thanks to the unprecedented flexibility in the control of the inter-particle potential, colloidal systems can show a variety of phase diagrams which have no counterparts in atomic or molecular systems (e.g. by decreasing the range of the attraction between colloidal particles it becomes possible to suppress the liquid phase, thus inducing solid-solid phase transitions [22]).

Despite being very complex in nature and number of components, colloidal dispersions can be easily described by using rather simple potentials. Indeed, the solvent and other additive degrees of freedom are quicker than the slow ones of the colloidal particles and they can thus be integrated out. Such eventuality provides the remarkable opportunity of describing the behaviour of colloidal dispersions through simple effective one-component models that take into account solely the colloids (e.g. the DLVO potential [23] or the Asakura–Oosawa model [24]).
For all these reasons, colloidal dispersions may be considered as model systems with desired interactions whose behaviour can be experimentally tested and systematically compared with theory and simulations.

1.1.2 Phase behaviour of spherically-interacting colloids

As mentioned in the previous section, a diversity of interactions between colloidal particles (e.g. van der Waals interactions, electrostatic double-layer forces, depletion interactions) may lead to colloids either attracting or repelling each other, giving rise to complex and interesting phase behaviours. Such phase behaviours can be viewed as the analogs of the phase behaviours of matter, with colloids playing the role of atoms.
Usually, spherically-interacting particles, in the presence of attractive interactions, undergo a gas-liquid phase separation, exhibiting a critical point characterized by a critical temperature T_c and a critical density ϱ_c.
In colloidal dispersions, such critical point is metastable, being always located in the region of the temperature-density phase diagram where the thermodynamic stable phase is a crystal.
Below the critical temperature, colloidal solutions separate into two phases differing in particle concentration: one poor in colloidal particles (gas phase) and the other one rich in colloidal particles (liquid phase).
In the liquid phase, particles try to minimize their energy by maximizing the number of nearest neighbouring particles. Anyhow, as the interactions between colloidal particles are typically short-ranged (i.e. the range of the interactions is usually smaller than the particle size), this turns out to be equivalent to maximize the number of contacts. Hence, spherically-interacting particles in solution result encircled by approximately twelve neighbours (such number is dictated by geometrical constraints) and, therefore, the coexisting liquid is a quite dense state.
At sufficiently low temperatures (i.e. for temperature values such that k_BT results lower than the interaction energy strength, where k_B indicates the Boltzmann constant) such dense state shows the typical behaviour of a glass, since all the possible motions of the colloidal particles are significantly hindered by the crowding.
Fig. 1.1 displays a schematic phase diagram for particles interacting with spherical symmetric attractive potentials, showing the field of metastability for the liquid phase, the gas-liquid coexistence region and the glass line.

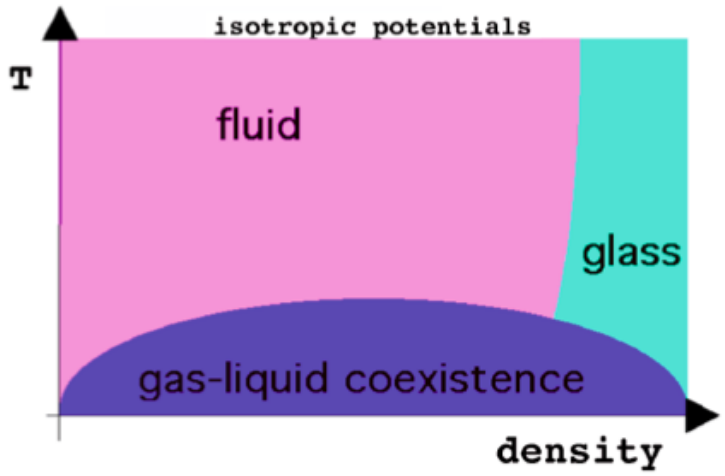

Figure 1.1: Schematic phase diagram for particles interacting with isotropic potentials. It can be seen that the glass line hits the gas-liquid spinodal at large densities. Figure from [25].

The field of metastability is the region of the temperature-density phase diagram where the equilibrium liquid phase exists for a time sufficiently long to allow for an experimental observation. Even when all the crystallization processes can be ignored (e.g. owing to the occurrence of a nucleation barrier longer than the time of the experimental measurement), the field of metastability is still delimited by the glass-line (which prevents the equilibration of the system on the time scale of the measurement) and by the liquid-gas spinodal (which prevents the equilibration of the system in eventual homogeneous structures). As it can be seen, the glass line intersects the gas-liquid spinodal on the liquid side and the phase separation process covers a large region of the phase diagram.

1.1.3 Beyond spherical interactions: from superatoms to supermolecules

In the previous sections we addressed the issue of how colloidal particles can be used as model systems for atoms, taking into account only spherically-interacting colloids. Anyhow, nowadays, a whole new generation of colloidal particles characterized by a large variety of anisotropic interactions is making its appearance. Indeed, an unprecedented progress in colloidal synthesis methods is currently providing new strategies to obtain high yield quantities of nano and micro-particles with different shapes, compositions and functionalities, thus offering a well-equipped arsenal for the fabrication of tomorrow 'supermolecules' [26, 30].
Innovative classes of colloidal particles with original shapes different from the spherical one (e.g. ellipsoidal, rod-like, cubic, polyhedral) are being conceived and synthesized in large quantities [31, 32].

At the same time, new generations of colloids with physically or chemically patterned surfaces are making their appearance [33, 34, 35, 36, 37]. The strategy of patterning the surfaces of colloidal particles with synthetic polymers or biological macromolecules (e.g. complementary DNA strands or proteins) provides valence to colloids, thus giving rise to specific anisotropies in the inter-particle interactions. The selectivity and directionality of the built-in interactions are the key elements of these new colloidal particles, which are generally named *patchy colloids* [19, 30, 33]. The number of patches (i.e. of attractive spots on the particle surface) is always limited and rather low, thus providing a well-defined coordination number of aggregation.
Beside the technological implications, understanding that anisotropic shapes and interactions via patchiness represent novel strategies for directing the self-assembly of targeted structures has greatly stimulated the research field, thanks to the outstanding possibility to go beyond spherical interactions and to shift from the colloidal atom to the colloidal molecule analog, by simply providing valence to colloids.
Such opportunity has rapidly catalyzed the research of new physical, chemical and biosynthetic methods for the synthesis of novel anisotropic building blocks. Specifically, as summarized in [35], the developed physical methods include electrified jetting, microcontact printing, emulsion drying, selective deposition, surface templating and lithography. Chemical methods include selective crystallization and deposition. Biologically inspired ones include instead the use of plant extracts, fungi and viruses to synthesize nanoparticles of various shapes.
These innovative synthesis strategies have led to the experimental realization of a broad collection of particles with specific anisotropy (Fig. 1.2), which in turn gives rise to a large variety of particles properties due to their anisotropic shapes or patchiness.
Each particle class in Fig. 1.2 represents an eventual building block for innovative self-assembled materials which could be reasonably inserted into hierarchical structures and could thus be used in a wide range of applications.
Thanks to the specificity of the built-in interactions, such innovative supermolecules with rationally designed shapes and attractive spots can be used not only to mimic the behaviour of molecular systems on larger scales, but, mostly, to investigate novel and unconventional phase diagrams. In fact, as in the case of spherical colloids where the richness offered by the possibility of modulating the interaction potential has allowed to go beyond the simple reconstruction of the atomic counterparts, the new generation of patchy colloids with different shapes and functionalities incredibly enlarges the range of possibilities. Indeed gelation [18, 21, 38, 39], gas-liquid phase separation [16, 40] and crystallization [41, 42] are greatly influenced by patchiness.
For instance, recent investigations on the phase diagrams of patchy particles have suggested that lowering the valence (i.e. the number of patches on the particle surface) has the singular effect of shifting the gas-liquid phase separation to lower temperatures and, more importantly, to lower densities [16].

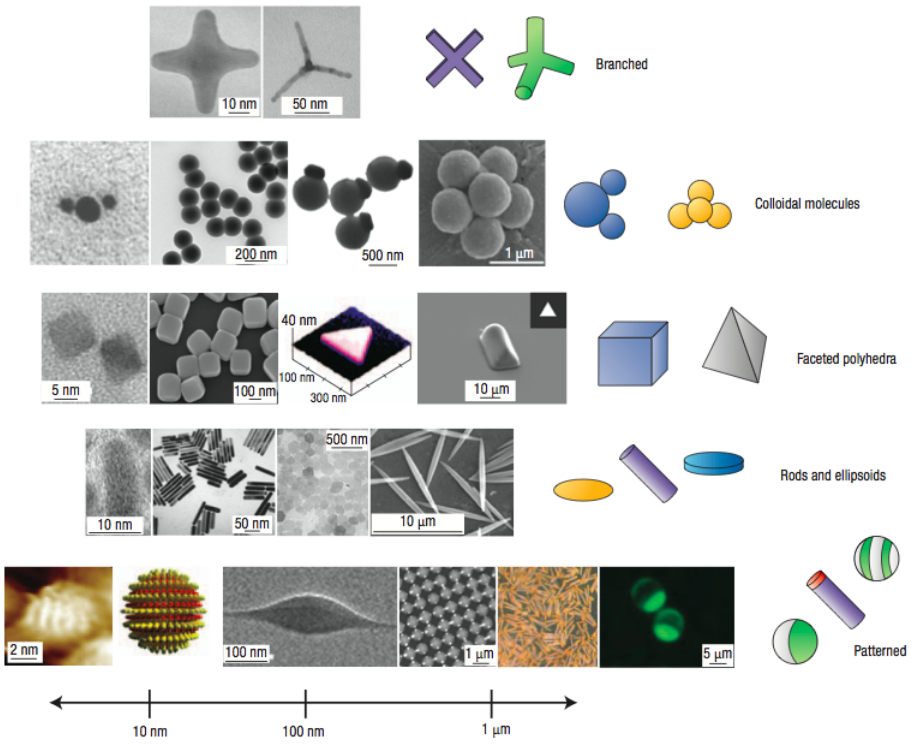

Figure 1.2: Examples of recently synthesized anisotropic building blocks. Particles are classified in rows by anisotropy type and increase in size from left to right. Figure from [35].

1.1.4 Colloidal gelation

Colloidal gels are arrested states of matter at low density or packing fraction (defined as $\phi = \pi\rho\sigma^3/6$, where σ is the diameter of the particles), i.e. arrested states in which a negligible fraction of the total volume is occupied by colloidal particles.
Similar to glasses, gels are metastable states out of equilibrium, that may interfere with the underlying stable phases. Since all the thermodynamic functions appear to be continuous upon crossing the arrest boundary, gelation cannot be considered a thermodynamic transition. It is rather a kinetic phenomenon as the system gradually slows down, not relaxing to equilibrium any longer.
Time scales are thus fundamental for determining whether a system is arrested or not. Specifically, in colloidal dispersions, one can operatively consider the relaxation time of the system, which can easily measured by Dynamic Light Scattering: if it is of the order of around 100 s it is possible to state that the system has arrested.
Like glasses, gels are disordered solids: indeed, they do not flow, their structural properties do not exhibit a long-range order and their large time scales are typically associated to the absence of long-time diffusion (even though in gels some motions are still allowed on short length scales).

Anyhow, unlike glasses, gels are dilute and always driven by attractive interactions. Indeed, because of their peculiar low density, the only possible mechanism to sustain stresses is for these systems to form stable networks of bonded particles: percolation is thus strictly necessary to obtain gels. Anyhow, percolation cannot be considered a sufficient condition since it has to be merged with dynamic information: the network of particles must persist on the time scale of the measurement.
For this reason, a fundamental concept in gelation is represented by the lifetime of the bonds between particles. According to it, it is possible to distinguish between two mechanisms of gelation: i.e. chemical or physical, the former caused by the formation of irreversible bonds between particles (i.e. bonds of infinite lifetime) whereas the latter depending on bonds originating from physical interactions of the order of k_BT (i.e. that reversibly break and form several times during the course of an experiment).
Hence, for chemical gelation, percolation corresponds to gelation, since as the network of bonds forms, it is, by definition, permanent. Therefore, in this case, where bond formation and bond duration are coupled, the percolation concept is strictly connected to the dynamics of the system and percolation theory represents the correct theoretical framework for fully describing the gel transition. In contrast, for physical gels, which are the ones usually formed by colloidal particles, the situation is much more complicated. Indeed, in this case, bondings are transient and clusters of bonded particles dissolve and form continuously. Therefore, percolation theory is only useful to depict the static connectivity properties of colloidal gels.
In the following, we will address the subtle interplay between physical gelation and phase separation as well as equilibrium routes to gelation following Zaccarelli's work on colloidal gels [18], to which we refer for further insights.

Physical gelation and phase separation

As mentioned above, percolation in physical gels does not coincide with gelation owing to the finite lifetime of the bonds among particles. In general, bonds having long lifetime require large attraction strengths. Anyhow, in all the systems characterized by an hard-core interaction integrated with a spherically symmetric attraction, large attraction strengths, further to increase the bond lifetime, lead to the onset of a gas-liquid like (colloid rich–colloid poor in colloidal systems) phase separation.
Using the Hill's work on liquid condensation, it is possible to rationalize the propensity of a system to phase separate [43]. Indeed, according to it, the free energy F_N of a cluster of N particles can be written as a sum of a bulk and a surface term, proportional to N and to $N^{2/3}$ respectively. Thus, it can be seen that $F_N/N = f_{bulk} + \gamma N^{-1/3}$, where γ is proportional to the surface tension and f_{bulk} is the free energy per particle in bulk conditions. Hence, we can distinguish two cases:

- If $\gamma > 0$, then F_N/N is minimized for $N \to \infty$ and hence a condensed liquid phase is expected.
- If $\gamma < 0$ a bulk liquid–gas like phase separation will be disfavoured.

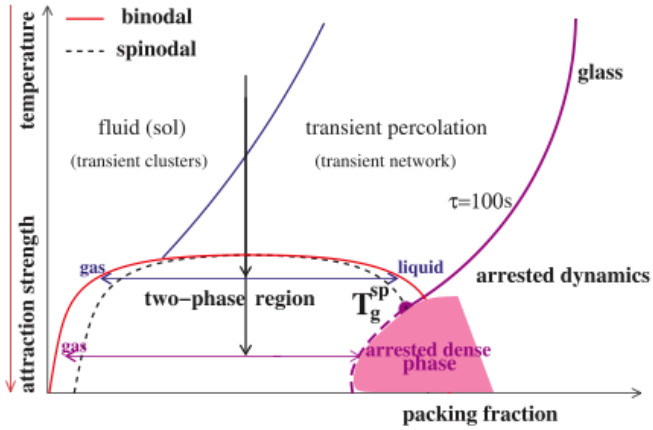

Figure 1.3: Scheme of the arrested phase separation scenario: a quench into the two-phase region may lead to an arrest of the denser phase. Figure from [18].

Interestingly, at sufficiently low temperatures, where entropic terms can be neglected, the surface tension is proportional to the energy gain of surface particles over bulk particles $\gamma \propto (e_{surface} - e_{bulk})$, where e represents the energy of a particle in a cluster. On the basis of these considerations, it is possible to make a fundamental distinction between two different kind of arrest by distinguishing whether the system undergoes gelation with or without the occurrence of phase separation.
If the phase separation boundary is crossed before that the arrest process occurs, the system undergoes liquid condensation. Specifically, the coarsening process promotes the formation of dense areas, which might arrest due to the crossing of the glass boundary. Such scenario is known as *arrested phase separation* [44] and it represents a non-equilibrium route to gelation, since it happens through an irreversible mechanism, i.e. spinodal decomposition. As it can be seen (Fig. 1.3), by performing a quench inside the spinodal in the temperature range $T_g^{sp} < T < T_C$ (where T_g^{sp} represents the intersection between the spinodal and the extrapolated glass line) the system undergoes a gas-liquid like phase separation; if the quench is deeper ($T < T_g^{sp}$), the system starts to undergo liquid condensation. However, with the progress of the coarsening process, locally dense areas could meet the nearby glass transition boundary, thus arresting.

Equilibrium approaches to gelation

If phase separation does not intervene (i.e. when the condition $\gamma < 0$ in Hill's formalism is fulfilled), the system is able to form a stable particle network through a reversible series of equilibrium states. This particular route to gelation is an equilibrium one, since, in this case, the gel state may be approached continuously from a single ergodic phase, by simply allowing an equilibration time for the system to readjust its structure. As previously mentioned, it is possible to adopt an operative definition of gelation

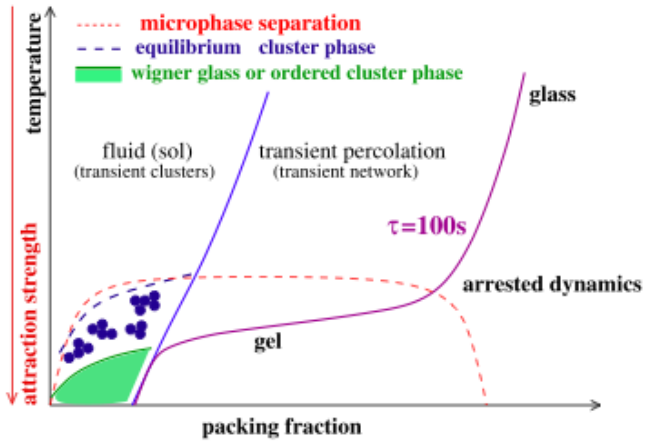

Figure 1.4: Scheme of the stabilization of of an equilibrium cluster phase and gel, through the inhibition of the phase separation region by an enhanced bond lifetime, when additional long-range repulsions are considered. At low T, equilibrium clusters are formed due to the microphase separation. At low T and larger ϕ, gelation results as percolation of the long-lived clusters. Figure from [18].

transition by considering the relaxation time of the system. According to it, a gel can only be achieved when the lifetime of the percolating network is larger than 100 s (i.e. the non ergodic behaviour persists for an observation time of 100 s). Rigorously, a true ideal gel transition should only take place when the lifetime of the network becomes infinite. Nevertheless, in the following, we will refer to equilibrium gel states as those reached continuously from the ergodic phase and exhibiting a very long, although not infinite, lifetime, maintaining the *ideal gel* concept only to those extrapolated states where the lifetime of the network becomes infinite.
In general, for equilibrium gelation, it is possible to discriminate between two diverse topological phase diagrams.
In the first case, the phase separation is moved towards higher attraction strengths [45] and it can be substituted by micro-phase separation. Such a scenario can be realized by effectively increasing the lifetime of the bonds, e.g. by inserting specific stabilizing barriers in the potential with [46] or without [47] a clear microscopic interpretation. Such a modification of the potential opens a window of stability for the equilibrium gel by pushing the phase separation at larger attraction strengths. Specifically, in the low density micro-phase separating region, equilibrium clusters can be found which merge into a percolating network at larger densities. A schematization of such scenario is shown in Fig. 1.4, where the $\tau = 10^2$ s-line indicates the slow dynamics, connecting the gel and the attractive glass line at higher densities.
In the second case, instead, equilibrium gelation is achieved when a mechanism for moving the phase separation not only to lower temperatures, but most interestingly to lower density values, is available. This can be easily realized by inducing directional

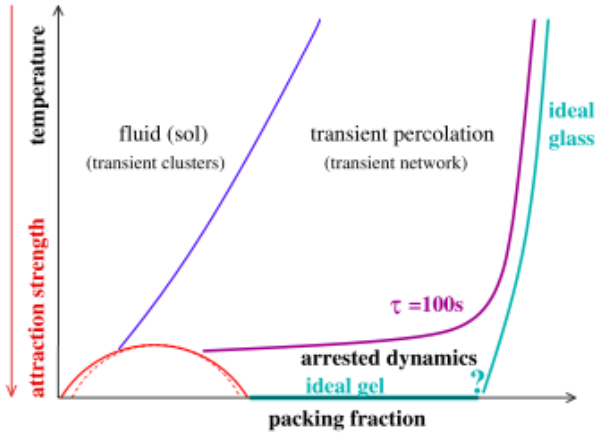

Figure 1.5: Scheme of the shift to lower packing fractions of the coexistence region with the clear insurgence of an equilibrium gel phase, as well as of the ideal gel phase at $T = 0$. The question mark refers to the unknown details of the crossover from gel-to-glass dynamics. Figure from [18].

interactions between colloidal particles, preferably of low coordination. Indeed, lowering the average coordination number (i.e. the valence of the particles) is a crucial condition to shift the critical point to lower packing fractions. In this case, $\gamma \to 0$ in the Hill's formalism since at low temperatures the energy of a particle is the same in the interior and on the surface of each cluster and the driving force for compact aggregation decreases (promoting saturated network structures). Hence, a different topology of the phase diagram is found (Fig. 1.5). As it can be seen, indeed, a wide region of stability of an equilibrium network, to become a gel at sufficiently low temperatures, opens up at low/intermediate densities. Through a careful equilibration procedure down to very low temperature, almost-ideal gel states may become accessible.

Bond lifetime as a tunable parameter

Starting from the existing literature on chemical gelation, several models were gradually developed to describe physical gelation.
The first work in which the idea of finite bond lifetimes was addressed is due to Liu and Pandey [48], who investigated, on a simple cubic lattice, the dynamics of aggregation of functionalized sites in two well-different conditions: irreversible and reversible aggregation (reversibility was taken into account by a finite bond breaking probability). Their results indicated a shift of the gel transition as a function of the bond breaking probability, associated with different scaling features and exponents.
Later on, a lattice model was introduced by Del Gado et al. [49, 50] with the specific aim of finding a relation between chemical and colloidal gelation as a function of a tunable bond lifetime. Specifically, they used tetrafunctional monomers with a fraction of randomly quenched bonds to reproduce the irradiation process of a polymer solution

that induces chemical bonds. In their model, bonds form with a specific probability and are permanent in the case of chemical gelation, while they can be broken with a finite probability in physical gelation. By defining τ_B as the lifetime of the bonds, it results that bonds break with a frequency $1/\tau_B$ so that a fixed number of bonds must always be present, thus allowing for the systematic comparison between the dynamics in the case of permanent and transient bonds. Interestingly, they found a power-law decay of the density correlation functions close to percolation for irreversible bonds (in agreement with experiments on chemical gels). On the contrary, by considering instead a finite bond lifetime, they discovered a crossover to a standard glassy dynamics, exhibiting a typical two-step decay.
A revisitation of such study, in terms of an off-lattice model, was later presented by Saika-Voivod et al [51]. Specifically, this last approach simply consisted of a variation of a square-well model with the addition of an infinitesimally thin barrier of arbitrary height u_h. To reproduce irreversible bond formation, this model was firstly analyzed in the case of infinitely high barrier [52, 53].
Advantageously, since the infinitesimally barrier has a zero measure in phase space, the thermodynamic and static properties of the system are effectively the same, either in the presence or in the absence of the barrier. Nevertheless, the dynamics of the system is highly affected by the height of the barrier.
This was demonstrated by studying the wavevector dependence of the density correlation functions $F_q(t)$ via Molecular Dynamics (MD) simulations. Indeed, the results of such investigation suggested that, in the case of infinite barrier height, the percolation transition implies a breaking of ergodicity for the system only at $q \to 0$, thus confirming that gelation in attractive systems corresponds to the development of a network of infinite connectivity. Beyond the percolation threshold, as the cluster size increases as $(p—pc)^{\beta}$, the non-ergodic behaviour is extended even to larger q, until all the particles of the system become part of the same infinite cluster and the system becomes definitely non-ergodic. Fig. 1.6 shows the behaviour of non-ergodic properties as the packing fraction of the system increases in the case of infinite barrier height. For packing fraction lower than the percolating one, all the density correlation functions at various wavevectors decay to zero, while for higher packing fraction the insurgence of a plateau can be clearly observed. The height of this plateau, i.e. the non-ergodicity factor f_q, results, at fixed packing fraction, strongly dependent on q. Moreover, by varying the packing fraction above the percolation threshold, one finds that large q-values result ergodic while small ones are not. Starting from the smallest q-value, which becomes non-ergodic slightly above the percolation threshold, the system further becomes non-ergodic at progressively larger q-values as ϕ increases. Left panel of Fig. 1.7 shows the ϕ-dependence of $F_q(t)$ at a fixed wavevector. As it can be seen, a non-ergodic behaviour is evident only well beyond the percolation threshold (ϕ_p= 0.23). Even the trend of f_q (right panel) with increasing ϕ signals the crossover from a low-q signal, revealing the non-ergodic behaviour of the network, to a non-ergodic behaviour at all investigated q. Interestingly, the α-relaxation time (i.e. the final relaxation to zero of the correlation function) at infinite barrier height diverges for each wavevector at a different packing

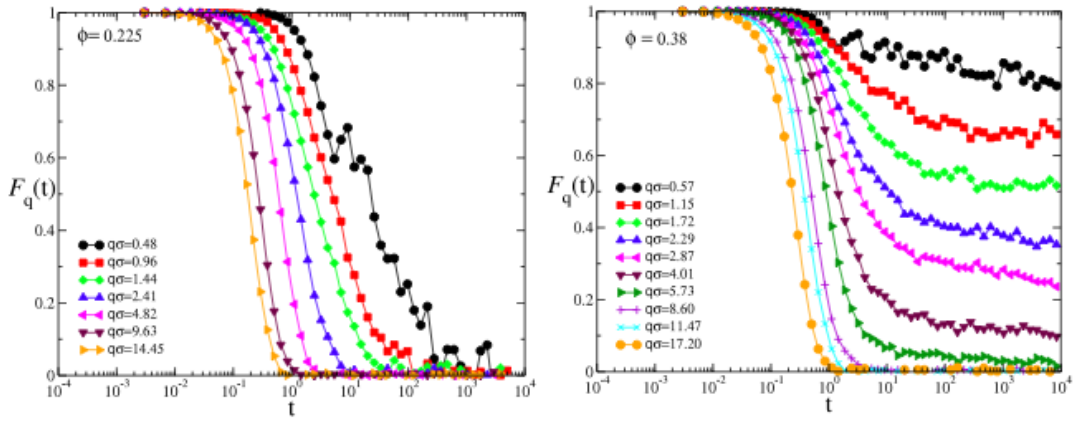

Figure 1.6: q-dependence of $F_q(t)$ for chemical gelation at two fixed values of ϕ: just below percolation (left) and well within percolation (right). ϕ_p= 0.23 for this model. Data from [51]. Figure from [18].

fraction, coinciding with the percolation one only at the lowest studied q-values. Upon increasing q, the divergence occurs when first the $F_q(t)$ shows a finite plateau. Therefore, non-ergodicity is completely dictated by percolation in the case of irreversible bonds. As the bond lifetime is reduced, the system initially follows the percolation regime, as long as τ_B is longer than α-relaxation time, and subsequently it crosses over to a glassy dynamics consistently with the model of Del Gado et al [49].
An important result of this work is that, rescaling the time by considering the different lifetimes of the bonds, all the observed curves superimpose onto a master curve. Such behaviour clearly suggests that τ_B affects only the microscopic timescale: therefore, if enough time is waited to allow bond-breaking processes to occur, the long-time behaviour becomes independent of the microscopic dynamics.

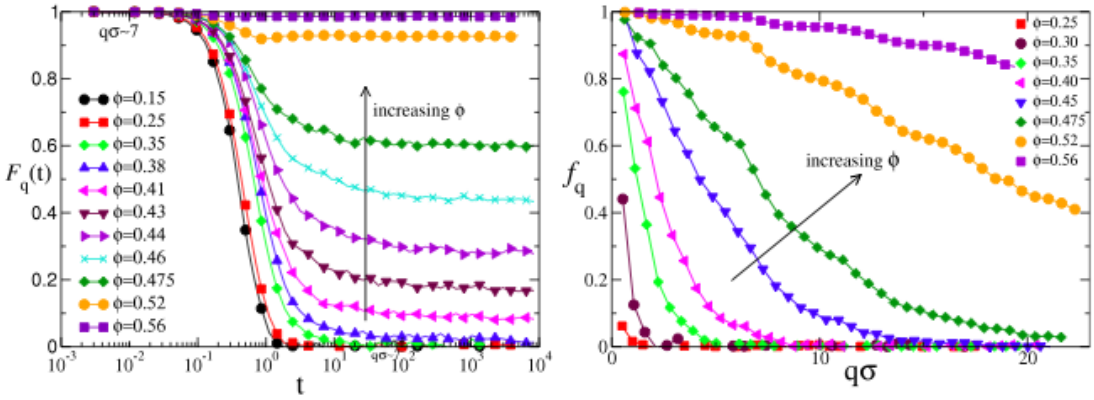

Figure 1.7: ϕ-dependence of $F_q(t)$ at the nearest-neighbour peak (left) and of the non-ergodicity parameter f_q (right) for chemical gelation. Data from [51]. Figure from [18].

1.2 Reduced-Valence Colloids

As anticipated in the previous section, an innovative category of patchy particles is that of colloids which, owing to the selectivity of the built-in interaction, have a well-defined and fixed valence [30, 33, 54], defined as the maximum number of bonded nearest neighbours. The study of simple models of reduced-valence colloids has recently been the subject of numerous investigations [16, 55, 56, 57], focalizing on both the thermodynamic and dynamic collective behaviour of such systems, as well as their out-of-equilibrium dynamics. In this context, innovative scenarios like the so-called empty liquids and the already mentioned equilibrium gels (which represent the analogy between colloidal gels and network forming liquids) have been suggested and developed. An experimental realization of limited-valence particles is reported in Fig. 1.8.

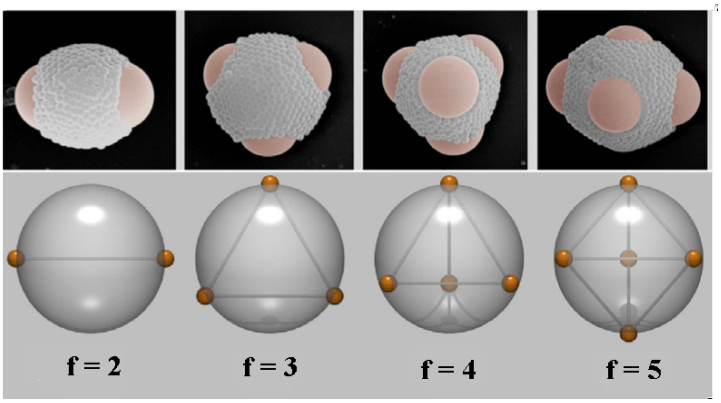

Figure 1.8: Top: Experimental realization of patchy particles from bidisperse colloids in water droplets. Bottom: Schematic representation of the location of the square-well interaction sites (centers of the small spheres) on the surface of the hardcore particle. Adapted from [18].

1.2.1 Phase Diagram

In Sec. 1.1.2 we have described the phase behaviour of colloidal particles in the presence of isotropic attraction, i.e. when each particle in solution can form bonds with any neighbouring particle within the attractive well, independently of the relative orientations. Specifically, we have showed that, upon lowering the temperature, the system tends to become as dense as possible, thus minimizing its potential energy and creating two separate phases having different densities.
In what follows, instead, we address the situation in which there is a directional attraction between colloidal particles, which can be realized by decorating only small portions of the particle surface with attractive patches (i.e. we now focus on the phase behaviour of limited-valence particles).
Indeed, in the last few years, there has been the outstanding scientific finding [16] that if the number of bonds that each particle can form is limited, then the propensity of the colloidal particles to phase separate is strongly suppressed. In particular, it has been

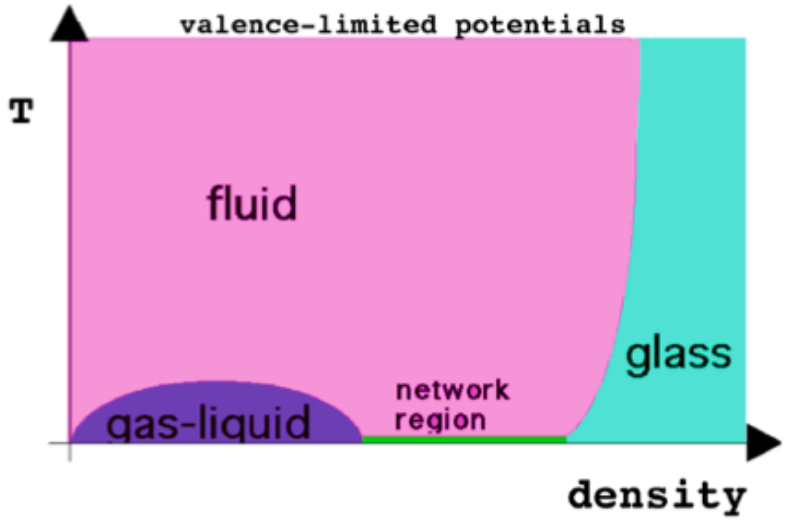

Figure 1.9: Schematic phase diagram for particles interacting with limited-valence potentials. In this case, the shrinking of the gas-liquid coexistence region opens up a window in which an extensively bonded network can form. Figure from [25].

shown that the reduction of the valence f provides an effective mechanism to shrink the gas-liquid coexistence region, thus opening a large window of intermediate densities in which there is no driving force for phase separation, as schematically shown in Fig. 1.9

Such scenario has been demonstrated theoretically (via application of the Wertheim thermodynamic perturbation theory [58, 59]) and via numerical simulations on simple patchy models. Specifically, it has been showed that the width of the liquid-gas coexistence region progressively reduces on decreasing the valence[16], gradually disappearing as the average functionality of the particles approaches two (Fig. 1.10). For small valence, Wertheim theory is helpful in offering a precise parameter-free depiction of the system in a broad window of densities and temperatures. This observed shrinking of the gas-liquid coexistence region plays a fundamental role on the phase behaviour of such systems since it provides the unprecedented opportunity to reach low temperatures without encountering phase separation (at densities in which packing is not an effective arrest mechanism). Such region of low temperatures (i.e. of long-lived bonds) and of low densities (i.e. where packing is not relevant) cannot be reached in spherical symmetric attractive potentials (Sec. 1.1.2) being usually pre-empted by phase-separation. On the contrary, in the reduced-valence case, even at low-intermediate packing fractions, most of the particles are fully bonded at low temperatures and there is no energetic gain in further increasing the density. Hence, on progressively decreasing the valence, also the critical density decreases. At coexistence, in the liquid side, the number of bonded neighbours is comparable to the valence and thus minor than in the isotropic case [60]. Therefore, the density of the liquid is lower than the one found for the case of spherically-interacting particles.

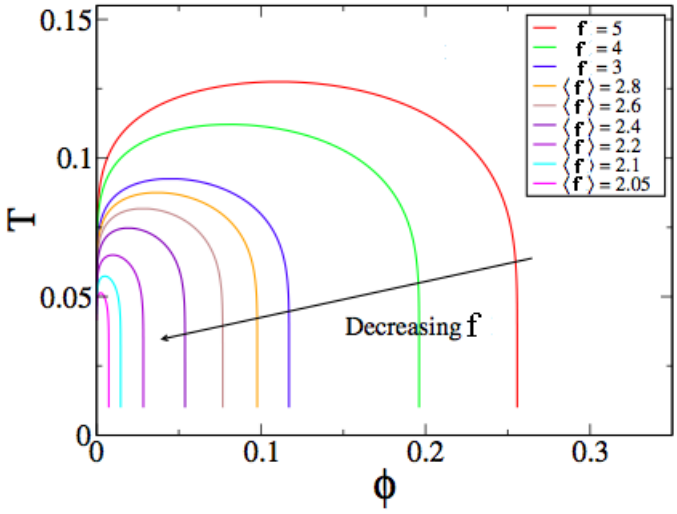

Figure 1.10: Shift of phase coexistence region with the valence f of the particles. For spherical attraction $f = 12$ from geometrical constraints; when $f < 6$ a systematic shift of both critical point and coexistence region can be observed. Adapted from [16].

As shown in Fig. 1.10, the shrinking of the region of instability hinges on the average valence per particle. In the limit of average valence approaching two (e.g. for a binary mixture of patchy particles having two and three attractive patches, in the limit of vanishing concentration of particles with valence three) the coexistence region approaches zero. Therefore, in this limit, a stable homogeneous empty-liquid phase of vanishing density can be reached, in which the system is structurally constituted by long chains of bi-functional particles cross-linked by three-functional ones [25].

1.2.2 Equilibrium Gels

The thermodynamic features that we have discussed in the previous section have singular consequences on dynamics of limited-valence systems. Indeed, as described, the empty liquid region provides the possibility of quenching the system to very low temperatures without encountering phase separation. Under these conditions, it becomes possible to approach the equilibrium gel states discussed in Sec. 1.1.4.
Indeed, empty liquids at low temperatures are composed by stable networks of particles which attempt to satisfy all the possible bonds. As a consequence, at a temperature which is rather low but finite, the system is very close to its energetic ground state (i.e. the state in which the maximum number of bonds that each particle can form is fulfilled) and, thus, upon further decreasing the temperature, the structure of system does not change anymore [55]. In this situation, the lifetime of the network is extremely long and regulated by an Arrhenius dependence on temperature, i.e. $e^{(E_A/k_BT)}$, where E_A represents an activation energy. The finite energy of the interaction guarantees that the structure of the network is not permanently frozen (as in chemical gelation) but it

can instead restructure itself, on a time scale fixed by the bond lifetime, which can be tuned at will externally.
Therefore, from this discussion clearly emerges that reduced valence is an indispensable condition for creating arrested states at low temperatures which are not driven by packing, as in the case of glassy systems, but by the development of a percolating network of bonded particles which occupies only a small fraction of the sample volume. Indeed, given the low density of the system, crowding cannot be responsible any longer for the slowing down of the dynamics upon cooling: therefore, dynamic arrest in reduced-valence systems is not due to packing but by the formation of an extensive network of particles which provides elasticity to the system.

1.2.3 A first experimental evidence

Despite this extensive theoretical and simulative work, the absence of a methodology for realizing bulk quantities of particles with reversible interactions and with controlled valence has till now prevented the experimental investigation of the systematic dependence of the coexistence region on the valence.
Anyhow, a first indirect support to the theoretical predictions about the phase diagram topology of limited-valence particles has recently been provided by a synthetic colloidal clay: laponite.
Laponite consists of a suspension of disks with an heterogeneous charge distribution, which behaves effectively as a system with a limited (although unknown) valence.
On this system, Ruzcicka et al. [17] have experimentally discovered a low-density phase separation, terminating at a finite but rather low clay concentration (significantly below close-packing). Such phase separation can be clearly observed in Fig. 1.11, which shows several photographs of Laponite samples in the concentration range $0.1 < C_W < 1.2\,\%$ for very long waiting times ($\backsim$30000 h).

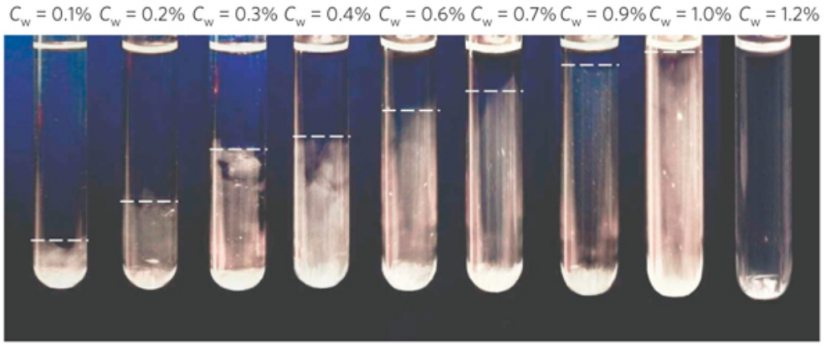

Figure 1.11: Photographs of Laponite samples in the concentration range $0.1 < C_W < 1.2\,\%$ at very long waiting times ($\backsim$ 30000 h). Figure from [17].

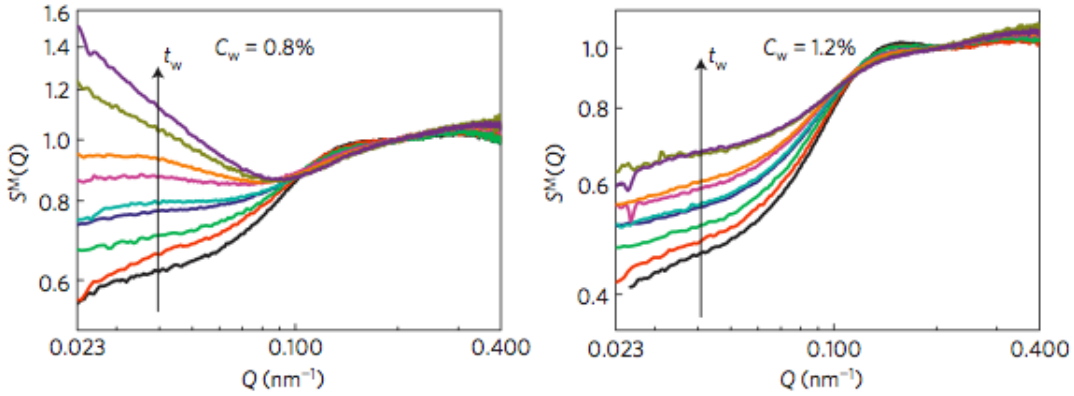

Figure 1.12: Evolution of the SAXS measured structure factor with waiting time for $Cw = 0.8\,\%$ (located inside the phase separation region) and for $Cw = 1.2\%$ (located outside the phase separation region). The curve are measured at increasing waiting time: from the bottom to the top tw = 500, 900, 1600, 2700, 3400, 4700, 6000, 8700, 11000 h). Figure from [17].

As it can be seen, all samples with $Cw < 1.0\,\%$ display two coexisting phases, separated by an interface whose height progressively increases with the clay concentration.
Above this phase transition, they found a stable gel: SAXS measurements of its structure confirmed that the system was in a stationary state consistent with equilibrium gels (Fig. 1.12).
Specifically, they investigated the behaviour of the static structure factor after a quench (used to reproduce the irreversible aging process occurring in laponite dispersions) both outside and inside the phase boundary, finding a totally different behaviour for the two samples at sufficiently long waiting times. Indeed, while the intensity scattered at small scattering angles increases continuously inside the phase separation region, it saturates to a constant value in the empty liquid one.
Such behaviour clearly suggests that the lifetimes of the bonds between particles in the system are so large that the empty liquid is arrested, thus forming an equilibrium gel. Indeed, as expected by the predictions, once the system has reached its final equilibrium configuration, where all possible bonds are fulfilled, its structure (and, hence, in turn the scattering intensity) does not change anymore.
To strengthen such results, they also performed computer simulations for a simply model of patchy disks with low valence, finding agreement with the experiments.
The phase diagram numerically obtained is reported in Fig. 1.13.
As it can be seen, it clearly indicates the phase coexistence region, the empty liquid and the equilibrium gel regions. The topology of this phase diagram is thus consistent with the one predicted for limited-valence colloids, thus providing the first experimental confirmation of the empty liquid scenario.
Anyhow, in spite of this important result, a conclusive evidence, proving the dependence of the critical parameters on the particle valence is still lacking.

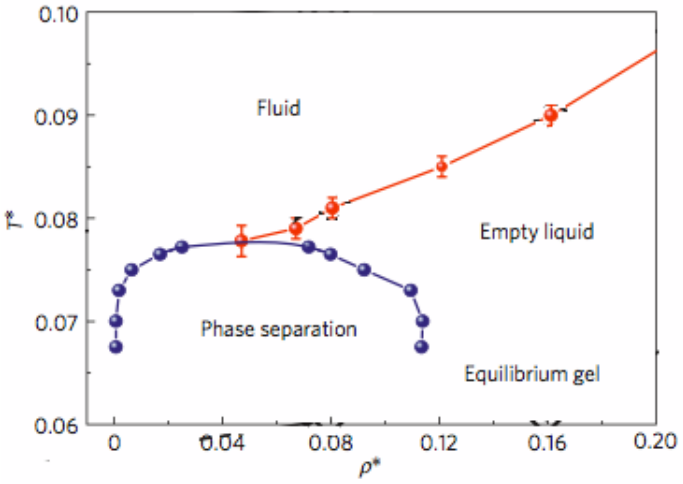

Figure 1.13: Phase diagram in the $\rho^* - T^*$ plane, where ρ^* is the number density scaled by the close-packing density and T^* is the thermal energy scaled by the bond strength. Figure from [17].

Chapter 2

DNA nanoconstructs

"At lunch Francis winged into the Eagle
to tell everyone within hearing distance
that we had found the secret of life".

James Dewey Watson

As a genetic material, DNA plays a key role in biology as the carrier of genetic information in all life forms, storing and encoding hereditary instructions.
For the last fifty year, DNA has been mainly competency of biologists or biologically oriented researchers who have deeply investigated its biological functions and its molecular configuration.
However, recently, scientists from different research fields, ranging from physics to materials engineering, have started to look at DNA from a completely different perspective, embracing the idea of exploiting its outstanding peculiarities for innovative non biological purposes.
Indeed, from material science and engineering standpoints, DNA's physical and chemical properties render it extremely useful for constructing new materials with tailored properties. In particular, its nanometric size, double-helical conformation and capability of hybridizing in a specific and thermo-reversible fashion make it appealing for designing nanoscale constructs with specific shapes and functionalities [2, 4].
Therefore, in the present chapter, we will spoil the DNA molecule from its biological gene-encoding function, focussing on its material aspects.
To this aim, in the first section, we introduce the fundamental physicochemical properties of DNA, emphasizing the aspects which allow and guide its self-assembling capabilities.
The following sections present instead the main developments in DNA-based engineering, focussing on its most recent applications to nanotechnology.
Specifically, after discussing the design parameters that can be exploited for engineering DNA materials, we present the main DNA topologies (i.e. linear, branched, dendritic and networked ones) which allow for the experimental realization of complex structures in one, two and three dimensions.

2.1 Basic Principles of DNA self-assembly

Self-assembly is the spontaneous formation - through free energy minimization - of reversible aggregates from basic building blocks. Currently, it represents one of the most promising routes for the realization of novel materials, as the possibility of tuning the shape, the valence, the flexibility and the mutual interactions of the individual building blocks provides the remarkable chance of finely control the physical properties of the designed materials.
In this field, biological interactions, characterized by specificity, directionality, reversibility and tunability, offer new ways for realizing particles with peculiar properties.
Among the most promising candidates, DNA occupies an emergent role thanks to its unique chemical/physical properties and to its incomparable molecular recognition capability which can guide the bottom-up assembly of complex materials with nanoscale precision.
In the following, we thus introduce the DNA molecule, emphasizing the main features that render it propitious as an innovative engineering material.

2.1.1 DNA structure

Deoxyribonucleic acid (DNA), the molecule of life, is a polymer consisting of monomers named nucleotides. Each nucleotide has three major components: a sugar deoxyribose (i.e. a five-carbon sugar molecule), a nitrogen base (nucleobase) and a phosphate group. There are four types of nucleotides in DNA, each one associated to a specific nucleobase: adenine (A), guanine (G), cytosine (C) and thymine (T). From a chemical perspective, adenine and guanine are purines (i.e. two-carbon nitrogen ring bases), while thymine and cytosine are pyrimidines (i.e. one-carbon nitrogen ring bases).
Each polynucleotide is characterized by a specific sequence of the nucleobases, conventionally written in the direction from the 5'-end (i.e. the end of the DNA strand that has the fifth carbon in the sugar-ring of the deoxyribose at its terminus) to the 3'-end (i.e. the end of the DNA strand which terminates at the hydroxyl group of the third carbon in the sugar-ring) of the sugar phosphate backbone.
A unique feature of the DNA polymer is that it can be either single-stranded DNA (ss-DNA) or double-stranded DNA (ds-DNA).
To form ds-DNA, two complementary strands of ss-DNA hybridize into a double helix structure in anti-parallel directions (one strand from 5' to 3' and the other from 3' to 5') [1]. The chirality conformation of the sugar moiety is responsible for the right-handedness of the helix. In its most common conformation, known as B-form (Fig. 2.1), the bases remain on average perpendicular to the axis of the helix.
Physically, in such configuration, one helical turn of ds-DNA consists of 10 base pairs (bp) with a length of around 3.4 nm and a diameter of approximately 2 nm.
Chemically, it is extremely stable, highly charged (bearing two elementary negative charges per base pair due to its phosphate groups) and thus easily water soluble.
The specific sequence of nitrogen bases is responsible for the DNA capability of carrying

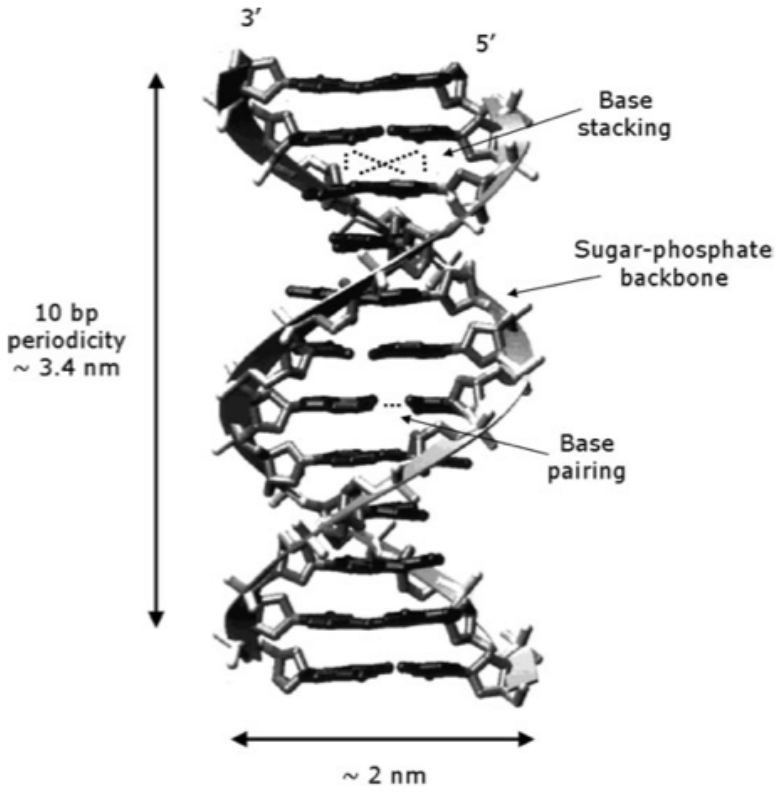

Figure 2.1: Schematic representation of the B-form of the DNA double helix. The figure shows the main forces which are responsible for the stability of the helix, i.e. base pairing and base pairing. Figure from [5].

the genetic information: to this aim it is, thus, fundamental that the nucleotides might form covalent bond chains (different nucleotides in a DNA chain are indeed bonded by phosphodiester bonds, i.e. specific covalent bonds between the 3' carbon atom of one sugar molecule and the 5' carbon atom of the neighbouring one).
Conversely, various non-covalent interactions, such as hydrogen bondings, hydrophobic interactions and electrostatic forces drive the assembly of ds-DNA.
Such weak interactions are indeed fundamental to enable the unzipping of the double helix, which represents the initial necessary step in DNA self-replication.
As we will see in the next section, two main forces are responsible for the stability double helix: hydrogen bonds between complementary nucleotides (base-pairing forces) and base-stacking interactions among adjacent aromatic nucleobases.
These forces govern the selectivity of the hybridization: indeed, as we will show, the energy of binding hinges on the degree of complementarity of the sequences along the polymers.

2.1.2 Helix stability

As mentioned, the stability of the DNA double helix depends on a fine balance of various interactions including hydrogen bonds between opposite bases and base-stacking interactions between adjacent bases. Therefore, slight variations in the DNA sequence may have deep implications on the stability of the helix.
For instance, mutations in the base sequence that result from errors that occur during DNA replication may result in mismatches that lead to relatively unstable duplexes. To gain a close insight into DNA duplex stability, and how it is affected by changes in the base sequence, scientists have studied the structure and thermodynamic stability of a variety of DNA duplexes by using a combination of physical methods including X-ray crystallography, ultraviolet (UV) melting and NMR.
In the next paragraphs, following the lines set by Ref. [5], to which we refer for further insights, we present an overview on the stability of the double helix, firstly addressing the study of the main forces (i.e. base pairing and base stacking) which guide the hybridization process and, subsequently, providing a thermodynamic description of it.

Base pairing and base stacking forces

In ds-DNA each type of nucleobase on one strand bonds just one type of nucleobase on the other strand, following a mechanism named *complementary base pairing*. Base pairing arises from the formation of hydrogen bondings between pairs of nucleotides. The strength of such interaction is maximum when the nucleobases match according to the Watson–Crick (WC) rule of complementary couples (Fig. 2.2), i.e. A-T (with the formation of 2 hydrogen bonds) and C-G (with the formation of 3 hydrogen bonds).
According to it, DNA strands with high GC-content are more stable than DNA strands with low GC-content.
As hydrogen bonds are not covalent bonds, they can be broken and rejoined relatively easily: the two strands of DNA involved in a double helix can thus be pulled apart like a zipper, either by mechanical forces or high temperatures, in a process called *denaturation*. Such reversible and specific interaction between complementary base pairs is crucial for all the functions of DNA in living organisms.

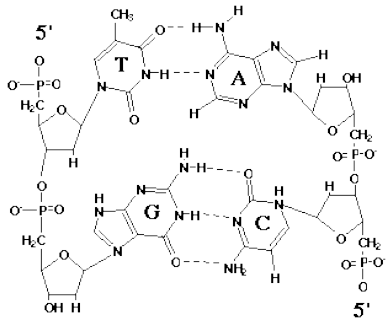

Figure 2.2: Schematic representation of the Watson-Crick pairing between nucleobases.

Clearly, the free energy associated with the formation of the double helix depends on the length of the nucleic acid chain and on the quality of the WC matching, decreasing for pairs of strands with low complementarity. Hence, base-pairing forces act to provide the necessary specificity of DNA bonds.
On the contrary, base stacking interactions are much less selective than pairing ones. Indeed, probably due to the hydrophobic nature of the nucleobases, stacking forces operate to pull the aromatic hydrocarbon rings of the nitrogen bases into mutual contact and, thus, their strength mainly depends on the overlap between the aromatic rings.
Despite being non-selective as paring ones, base-stacking represents the principal source of stability of ds-DNA.
Moreover, it is worth to note that, when combined with the geometrical constraints of the sugar-phosphate backbone, stacking forces have also a structural effect, causing a twist of each base pair of approximately 36° with respect to the neighbouring ones.
Hence, the double-helix structure of ds-DNA is the result of the synergetic action of base pairing and base stacking forces: thermodynamic studies of DNA are thus focussed on determining the combined value of stacking and pairing in the overall Gibbs free energy.

Nearest Neighbours Model

From a thermodynamic point of view, the hybridization of ds-DNA involves changes in entropy (S) and enthalpy (H) and it can be thus described by considering the overall variation in the Gibbs free energy G:

$$\triangle G = \triangle H - T\triangle S = G_D - G_U \tag{2.1}$$

where G_D and G_U refer to the free energy associated to duplexes and unbound strands, respectively.
Depending on the affinity between nucleobases and on the contribution from stacking forces, the formation of the helix results strongly sequence-dependent: hence, evaluations of ΔG must take into account the specific sequences of nucleotides involved in the process.
The simplest general way to consider them is to assume that all the effects are dominated by nearest-neighbours interactions, i.e. adopting the so called "Nearest Neighbours Model" (NN) [61, 62].
Clearly, considering only WC pairing, we can have ten of such nearest-neighbours interactions in antiparallel DNA strands, given by:

A-A	**A-T**	**T-A**	**A-G**	**G-A**	**A-C**	**C-A**	**G-C**	**C-G**	**G-G**
: :	: :	: :	: :	: :	: :	: :	: :	: :	: :
T-T	**T-A**	**A-T**	**T-C**	**C-T**	**T-G**	**G-T**	**C-G**	**G-C**	**C-C**

Indeed, since pairing and stacking act together, the minimum entity which takes into account both contributions is a quadruplet formed by two consecutive nucleotides on one strand and the corresponding nucleotides on the other strand.
For the ten possible quadruplets, the hybridization free energies $\triangle G_Q$ are tabulated together with the corresponding contributions in terms of enthalpy $\triangle H_Q$ and entropy

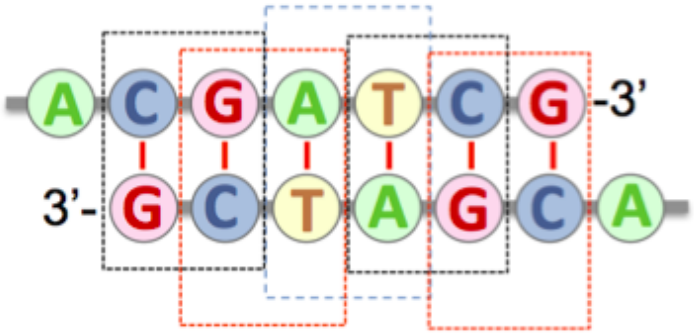

Figure 2.3: Schematic representation of the NN approach to the calculation of free energy of hybridization of a DNA sequence.

$\triangle H_Q$. On this basis, the variation of free energy involved in the formation of a double helix can be simply estimated by using:

$$\triangle G = \sum \triangle G_Q + \triangle G_{IN} \tag{2.2}$$

where the summation is on all the quadruplets of the considered sequence (for an example refer to Fig. 2.3) and $\triangle G_{IN}$ is an initiation free energy which represents the energetic cost involved in constraining the two strands in the conformational space available to them when they are bonded [63].
The scenario which arises by performing an accurate thermodynamic analysis by using the NN model is that stacking forces always promotes the formation of the helix, while base-pairing interactions only act to reinforce the correct WC pairing, by providing a free energy penalty for invalid pairings.

2.1.3 Melting temperature

As explained in the previous section, the stability of ds-DNA crucially depends on weak interactions between nucleobases which are responsible for the singular temperature behaviour of DNA double helices. Indeed, as the temperature increases, the weak non-covalent bonds between nucleobases break and the helices become gradually unstable and denatured.
Operatively, it is possible to identify a specific temperature value that characterize such behaviour by defining the melting temperature T_m of the system as the temperature where, for half of the double helices, the two strands have unbound and split (i.e., where $\Delta G = 0$).
The term is appropriate because the sharpness of the transition approaches that of a true phase transition. Indeed, for synthetic DNA, with a regularly alternating sequence of bases, the fraction of double helices can decrease from 0.75 to 0.25 in 1°C or less.

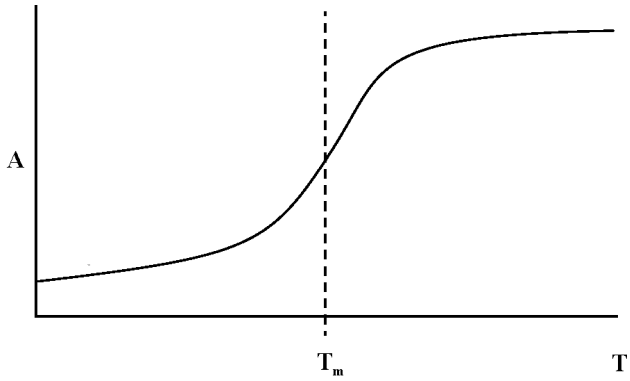

Figure 2.4: Thermal denaturation transition of a DNA helix: UV absorbance increases with temperature in a sigmoidal shape, following the unstacking of the bases.

Such transition can be monitored by optical or calorimetric methods. An example is reported in Fig. 2.4, where the UV absorbance of DNA is plotted as a function of the temperature.
As it can be seen, the UV absorbance increases with temperature, following a sigmoidal shape: T_m is thus determined as the middle point of double helix to single strand transition (corresponding to a fraction of single strands equal to 0.5). The observed melting curve is completely reversible and it is a sensitive function of environmental conditions such as ionic strength, pH and solvent characteristics.

Ionic strength dependence

As previously mentioned, DNA bears two elementary negative charges per base pair due to its phosphate groups in a wide range of pH values. As a consequence, ds-DNA has a linear charge density of approximately $-6e^-/\text{nm}$, which can be highly affected by the screening of counterions in electrolyte solutions [5].
Indeed, the ionic-strength of the media can significantly alter the binding-unbinding equilibrium of the DNA strands, by modifying their bonding free energy. In fact, DNA strands are charged polymers and, if the terminal binding sequence would be missing, would repeal each other. Such repulsive interaction is progressively screened by the addition of salt, resulting in a more favorable binding condition.
Such behaviour is evident from the strong dependence of the melting temperature on the ionic strength of the medium [62, 64]: e.g., for a 12mer, the melting temperature of the strand increases by approximately 30°C upon varying the sodium concentration from 0.05 M to 1 mM.
Interestingly, recent measurements [63] have reported that both $\triangle H$ and $\triangle S$ increase upon increasing the ionic strength of the medium.
Moreover, Yakovchuk et al. [65] have investigated how the components of the quadruplet free energy, i.e. base pairing and base stacking, are affected by the salt. Unexpectedly, they found an unforeseen dependence of the stacking parameters on the salt

concentration. Indeed, contrary to their original assumption that the base pairing term was fully responsible for the ionic strength dependence of DNA melting stability, their results clearly showed that, while base-stacking is influenced by the ionic strength of the medium, base-pairing is not. Anyhow, since numerous concomitant factors govern base-stacking interactions, it is not clear which one is mainly responsible for the evident influence of the salt concentration on DNA hybridization [65].
For practical standpoints, the ionic strength dependence can be taken into account in the evaluation of $\triangle G$ and T_m using empirical equations that present a logarithmic dependence on salt concentration which fairly reproduces the experimental data [62, 64].

2.2 Structural DNA-nanotechnology

In the previous section we have introduced the Watson-Crick pairing of adenine with thymine and guanine with cytosine, showing how it appears to be the favored type of interaction among nucleobases when the sequences permit it.
As mentioned, biology relies on the selectivity of such interaction for the expression of genetic information. Nevertheless, biology is no longer the only field of science where DNA plays a significant role. Indeed, nowadays, it has become possible to exploit the DNA complementarity to gain control over the structure of matter, in order to build innovative nanomaterials with tailored features.
Such a possibility is offered by the typical dimensions of the DNA molecule which, as previously seen, are inherently on the nanoscale. Consequently, the specific branch of science which focuses on DNA as a nanoscale building block of nanotechnological relevance is commonly named 'structural DNA-nanotechnology' and its final goal is the finest possible level of control over the spatial and temporal structure of matter.
According to the inventor of the field, N. Seeman, structural DNA nanotechnology rests on three pillars [66]:

- Convenient synthesis of designed sequences;
- Hybridization;
- Stably branched DNA.

In what follows we will see how the interplay of these three elements can be exploit to design and realize a large variety of all-DNA superstructures, ranging from crystals to hydrogels.

2.2.1 Structure design

Building with DNA involves the rational design of specific sequences that will assemble into the desired conformation.
Inspired by Seeman's work, experts in the field have developed eight empirical rules for properly designing stable branched DNA nanostructures which can be followed more or

less strictly depending on the specific needs [67]. Such rules (involving detailed instructions on sequence length, GC content, Gibbs free energy, etc.) are briefly summarized in the following:

1. **Sequence Length:**

   The sequence should be designed long enough to form a stable DNA structure. To this aim, a minimum of 8 nucleotides is required to give stability to the structure.

2. **GC content:**

   GC-content represents the percentage of nitrogenous bases on a DNA molecule that are either guanines or cytosines. Since the GC pairs are bound by three hydrogen bonds, while AT pairs are bound by only two hydrogen bonds, DNA with high GC-content is more stable than DNA with low GC-content. In general, sequences are routinely chosen so to have a GC content of around 50%.

3. **Non-Watson–Crick base pairing:**

   Sequences containing many consecutive guanines should be avoided since G-rich sequences may lead to the formation of four-stranded helical structures with G bases stacked on one another.

4. **Gibbs free energy:**

   Low or intermediate free energies are desired for designing DNA sequences that can form stable DNA duplexes. Currently, several DNA synthesis companies provide online websites for calculating the Gibbs free energy associated to a specific sequence. These online services are useful for eliminating non-desirable sequences.

5. **Secondary structure:**

   In general, sequences should be designed to achieve the least amount of secondary structure.

6. **Helix geometry:**

   It is important to take into account the helix geometry. Half-turns of the helix are the quantum of the design (5*n bp, where n = 0, 1, 2 ..., are between junctions).

7. **Symmetry:**

   To obtain stable self-assembling structures, the sequence symmetry of each arm should be avoided. For instance, biologically derived branched DNA molecules, such as Holliday junctions[1], are inherently unstable, because they exhibit sequence symmetry. Such symmetry enables an isomerization known as branch migration

[1]Holliday junctions are mobile junctions between four strands of DNA, which represent the central intermediate structures in genetic recombination. Specifically, such junctions are formed by the crossover of two strands of DNA between two helices with the same sequence.

that allows the branch point to relocate. Branch migration can be easily eliminated by choosing sequences that lack in symmetry in the vicinity of the branch point. In general, minimization of the sequence symmetry leads to greater control over the self-assembling structure.

8. **Dimerization, triplexation, Z-DNA formation:**

   The sequence should not form a self-dimer, a triplex or adopt a Z conformation.

2.2.2 Sticky-end cohesion

As a chemically-based self-assembling system, DNA plays a key role in bottom-up nanotechnology, i.e. in all those nanotechnological constructions in which molecules self-assemble in parallel steps according to their molecular recognition properties.
Such bottom-up approach dates back to the seventies, when genetic manipulation was performed for the first time by connecting molecules via the so called 'sticky ends'.
A sticky end is a single-stranded overhang sequence which protrudes from one terminal of a ds-DNA molecule. Such overhangs need a particular attention since they are commonly exploited to join DNA fragments.
Indeed, two molecules with complementary sticky ends can cohere to form a molecular complex, as shown in Fig. 2.5a, where two double-helical molecules are shown to cohere via hydrogen bonding.

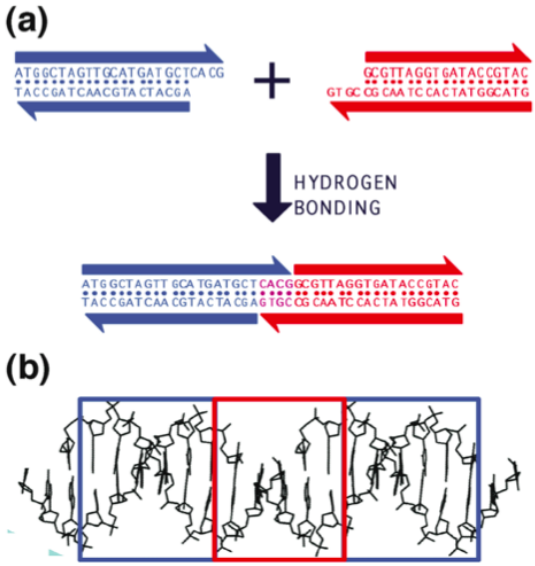

Figure 2.5: Scheme of sticky-end cohesion. (a) Two linear DNA duplexes with complementary sticky-ends are shown. Sticky-ends can bring these duplexes together through specific hydrogen bonding. (b) The product of the association is the classic ds-DNA. Figure from [66].

Sticky-ended cohesion represents a spectacular example of programmable molecular recognition. Indeed, being available four different nucleobases, there is a wide diversity to possible sticky end sequences (i.e. 4^N for a sticky end of N bases); moreover, the structure that they form at the site of the cohesion is well known since it is the classic Watson-Crick double helix (this key point is illustrated in Fig. 2.5b). Therefore, sticky terminals offer predictable control over supermolecular assembly and predictable geometry at the point of cohesion [66].
In this respect, DNA strands can be thus considered unique since they provides a programmable recognition system with unprecedented control over intermolecular interactions, together with well-known structures for their complexes.
Due to their fundamental role in the self-assembly process, sticky ends must be properly designed. To this aim, a key concept that must be taken into account is the difference between palindromic and non-palindromic sequences. Palindromic sequences allow for self-hybridization since they present the same 5' to 3' base order as their complementary strand (e.g. 5'-CGATCG-3' exhibits the same nucleobase sequence with its complementary strand: 3'-GCTAGC-5'). Palindromic sticky ends self-recognize themselves and this is useful for creating self-assembled materials such as DNA hydrogels. On the contrary, non-palindromic sticky ends offer a high control on the bondings between different DNA strands and it can be used to avoid self-ligation.

2.2.3 DNA topology

Despite the numerous possibilities offered by sticky-end cohesion, there is an additive problem that needs to be solved in order to design interesting self-assembling materials: double helices are unbranched structures. This means that connecting DNA strands via sticky-end cohesion can only result in longer structures, possibly with specific constituents arranged in a precise order in 1D.
Anyhow, to build useful materials using DNA strands, multiple-dimension synthesis is required: to this aim, branched DNA structures are needed.
Consequently, despite the fact that linear DNA is relatively easy to design, it was indispensable to create more complex DNA constructs to enlarge their efficiency as basic building blocks. In particular, branched nanostructures, e.g. Y-shaped and X-shaped DNAs, have been successfully realized [68].
Such branched structures can be rationally designed to present sticky-end sequences which allow for the binding with other branched DNA building blocks, promoting the controlled self-assembly of complex dendrimer-like structures. Moreover, they can also form two dimensional and tridimensional networked materials, such as DNA hydrogels, through the use of various physicochemical methodologies.
Hence, as for other synthetic polymers, it is possible to define several categories of DNA topologies (i.e. linear, branched and networked), each one characterized by its own properties and functions. In the next section, we, thus, present a brief overview on the main DNA topologies, following the scheme of [69], to which we refer for further insights.

2.2.3.1 Linear DNA

Linear DNA is the first topology utilized for assembling nanomaterials: it can be used to build complex structures through the combination with various elements, e.g. gold nanoparticles, carbon nanotubes and proteins.
For instance, linear DNA has been widely exploited to guide the assembly of gold nanoparticles in a broad range of applications, including biosensing [70]. Interestingly, it has also been used in the design and realization of an innovative DNA-based strategy for purifying single-walled carbon nanotubes from polydisperse mixtures of tubes differing in nanotube diameter and chirality [71]. Moreover, Niemeyer et al. [72] have demonstrated that the sequence-specific base-pairing of linear DNA can be a powerful tool to control the location of proteins at the nanoscale, by studying the binding of DNA–protein conjugates on a long ss-DNA scaffold.

2.2.3.2 Branched DNA

In order to go beyond the practical limits imposed by linear DNA, branched DNA structures have recently been developed.
The construction of a branched DNA structure was the first challenge in the field of structural DNA nanotechnology and it was overcome by Seeman [73], who succeeded in creating the first four-branched structure: a synthetic replica of the Holliday junction. Such structure is formed by four DNA partially complementary sequences of equal length, each one able to hybridize with two of the other strands.
The resulting star-shaped DNA structure has four double-helical arms flanking around a fixed branch point (Fig. 2.6).

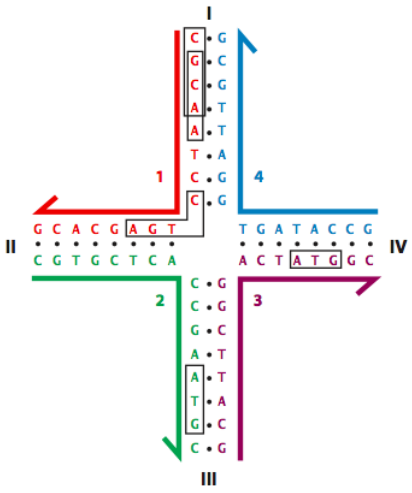

Figure 2.6: Star-shaped DNA nanostructure, resulting from the hybridization of four partially complementary sequences (blue, purple, green and red). Figure from [66].

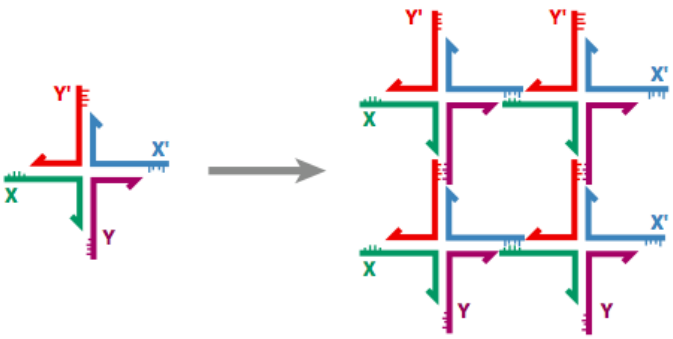

Figure 2.7: Self-assembly of branched DNA molecules to form larger arrangements. Left panel shows a four-arm branched junction made from four differently colored strands. Right panel shows how four junctions self-assemble through sticky-ended cohesion to form a quadrilateral. Figure from [66].

Interestingly, four of such constructs can further associate via sticky-ended cohesion to form larger and larger arrangements (Fig. 2.7) so that, in principle, the overall structure can be extended to create an infinite lattice.
Following this line, other branched structures with increasing number of arms and complexity have been built via the rational design of the sequences, including DNA cubes, knots, Borromean rings and tetrahedra [74, 75, 76, 77].

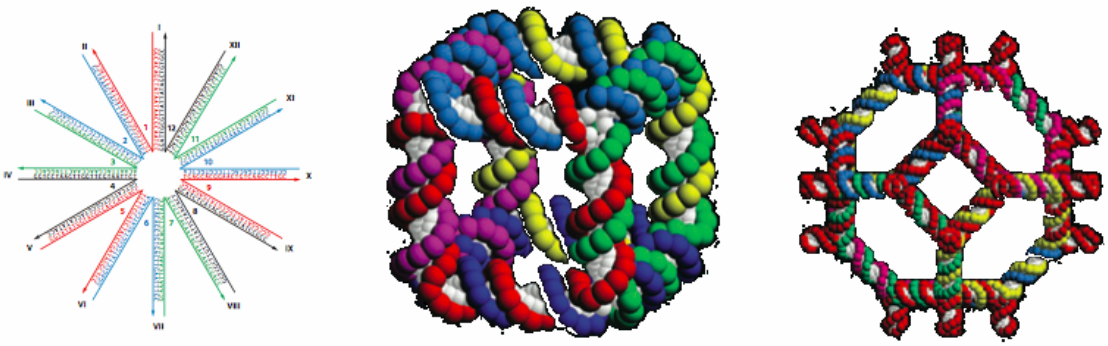

Figure 2.8: Topological constructs built using DNA strands. (a) A 12-arm junction: it is not possible to eliminate symmetry around the center of this junction, so identical nucleotide pairs are spaced at four-step intervals around the junction. Figure from [75]. (b) A cube-like molecule: such molecule is a hexacatenane; each edge corresponds to two double helical turns of DNA. Each backbone strand is drawn in a different color (each one corresponding to a given face of the cube). Figure from [76]. (c) A DNA-truncated octahedron: this molecule is a 14 catenane with each edge consisting of two turns of ds-DNA. Figure from [77].

Moreover, branched DNA can grow to highly complex structures such as dendrimers or "starbust polymers" ((i.e. nanoconstructs having highly branched but regular internal architecture) with different functionalities, including the possibility of using them as molecular cages and carriers for gene delivery in living organisms.
Such dendrimer-like DNA (DL-DNA) are typically assembled in steps by recurring unit components from several central multifunctional cores on which radially branched 'generations' are attached through covalent linkages, thus achieving the creation of nanostructures with a tree-like architecture.
DL-DNA can be used to construct anisotropic nanostructures by customizing the sticky ends. For instance, recently Luo and coworkers [78] realized well-defined DL-DNA structures by using branched Y-shaped DNA (Y-DNA) with non-palindromic sticky ends, so that it could only be ligated to another Y-shaped DNA via base pairing. The choise of using non-palindromic overhangs eliminates the possibility of self-ligations.
In this scheme, a flexible Y-DNA building block constituted the initial seed, to whom farther Y-DNA structures having sticky terminals complementary to the core Y-DNA were attached to realize the first generation, G1, of the dendrimer. Analogously, subsequent generations (namely G2, G3, etc) were created by ligating peripheral Y-DNA structures to the overhangs of the previously-formed generations (Fig. 2.9). The mentioned flexibility of the building blocks was necessary to achieve the remarkable goal of filling space with the DL-DNA. Such DL-DNAs were exploited to investigate the structure-dependent immunostimulatory activity enhancement [79].

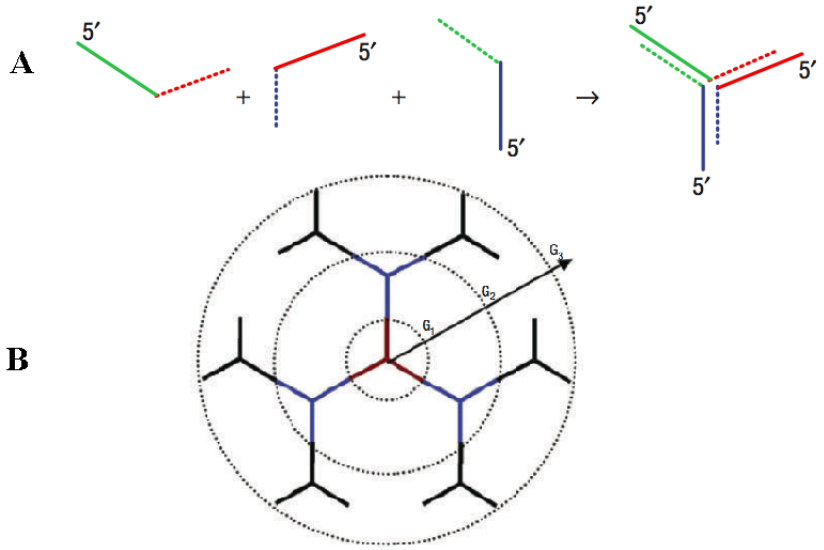

Figure 2.9: Schematic illustration of (A) Y-shaped DNA building block and (B) dendrimer-like DNA formation. Figure adapted from [78].

2.2.3.3 Networked DNA

Networked DNA structures consist of several DNA strands which are crossed or interconnected either covalently or non-covalently. Typically, networked DNA structures are characterized by an enhanced rigidity.
Indeed, while linear and branched DNA can be used to obtain complex DNA assemblies, their absence of rigidity hampers the successful self-assembly of ordered two-dimensional arrays for nanotechnological applications. In fact, all the aforementioned DNA branched structures are floppy, being characterized by variable angles between their arms.
Therefore, in order to realize useful DNA materials, rigid junctions were needed to be developed and this represented the second challenge in DNA-based nanotechnology.
Such challenge was again overcome by Seeman and collaborators, who joined two or more double helices using a ss-DNA that begins on one helix and switches onto the adjacent helix, thus resulting in a tile having a double crossover (DX molecule). In this DX-motif, paired double strands are parallel and the interactions between single units are introduced by sticky-ends located at their edges [80].
Interestingly, the persistence length of a DX motif is approximately twice that of a linear duplex.
Later on slight variations of such motif were introduced, resulting in triple crossovers (TX) and paranemic crossovers (PX), all characterized by an enhanced rigidity and a highly planar format. A scheme of such motifs is shown in Fig. 2.10.

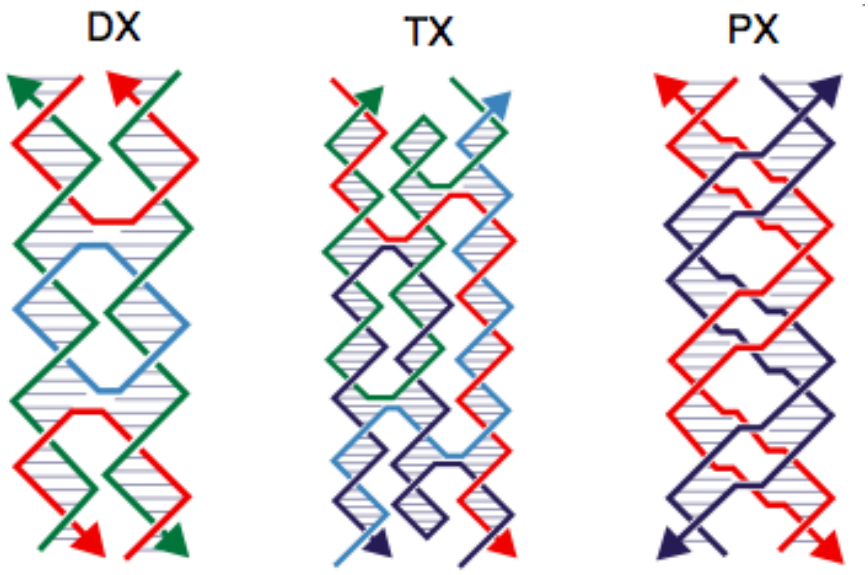

Figure 2.10: Schematic representation of double crossover, triple crossover and paranemic crossover motifs. Figure adapted from [66].

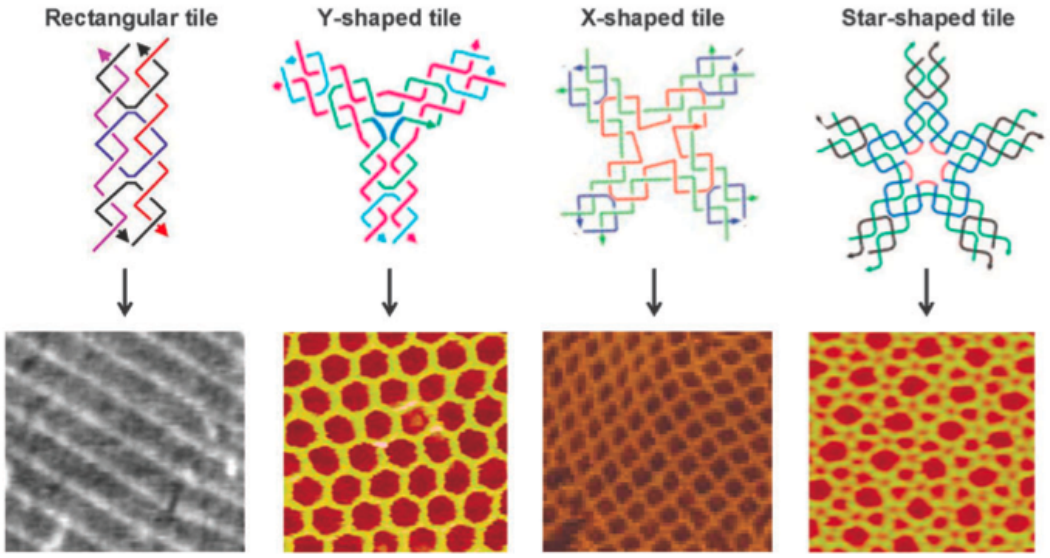

Figure 2.11: Schematic representations of several DNA tiles: rectangular, Y-shaped, X-shaped and star-shaped. The AFM images show the two-dimensional lattices achieved from the self-assembly of multiple copies of the same DNA tile. Figure from [69].

DNA tiles Combinations of these motifs were later exploited to build DNA tiles. Such tiles may have analogous shapes to the branched Y-DNA and X-DNA, but they can also exhibit more complicated arrangements, e.g star-shaped, from which more useful two-dimensional structures can be realized (Fig. 2.11).
For instance, a diversity of two-dimensional patterns, such as checkered-pattern [81], hexagonal [82], cross-shaped [83] and star-patterned [84] lattices have been rationally assembled by exploiting DX DNA tiles.
It is worth noting that one initial limitation of the first developed 2D ordered patterns was given by their limited domain size which was at most of few micrometers, making them useless for any practical applications.
Such obstacle has been successfully overcome by Mao et al. [85] who introduced an innovative approach to sequence symmetry for designing DNA structures. His approach was apparently against the general believe that to create stable DNA structures, the sequence symmetry should be minimized in order to avoid eventual undesired results in the self-assembly. Anyhow, it should be clarified that the sequence symmetry here addressed is among different DNA strands within the same motif at symmetric positions, but in each individual strand the base-pairing symmetry is still avoided.
Exploiting the four-fold symmetry of the cross-shaped tile, the three-fold symmetry of a three-point star and introducing perfect sequence symmetry in such tiles, they were able to avoid any unpredictable distortions in DNA nanostructures. This further allowed the formation of well-defined 2D DNA lattices with domain size over 1 mm.

Besides assembling two-dimensional structures, DNA tiles have been used to achieve more sophisticated three-dimensional structures with enhanced rigidity and stability.
Such achievement had a remarkable importance since three-dimensional structures built by DNA offers a large range of possibilities, including the chance to be used as molecular hosts in drug delivery systems or to encapsulate the folding and activity of encapsulated proteins.
For instance, Mao and coworkers adopted the rules of symmetry to guide the three-dimensional assemblies of building blocks with identical arms, realizing three-dimensional DNA polyhedra by exploiting multiple copies of three-point star DNA tiles [86].
All the three-point star DNA tiles were created to face in the same direction, so that their curvatures could add up and promote the formation of three-dimensional closed structures.
By controlling the flexibility and concentration of these tiles, a range of tridimensional structures including tetrahedra, dodecahedra and buckyballs were built from a minimal set of building block.
A schematic representation of such polyhedra is reported in Fig. 2.12

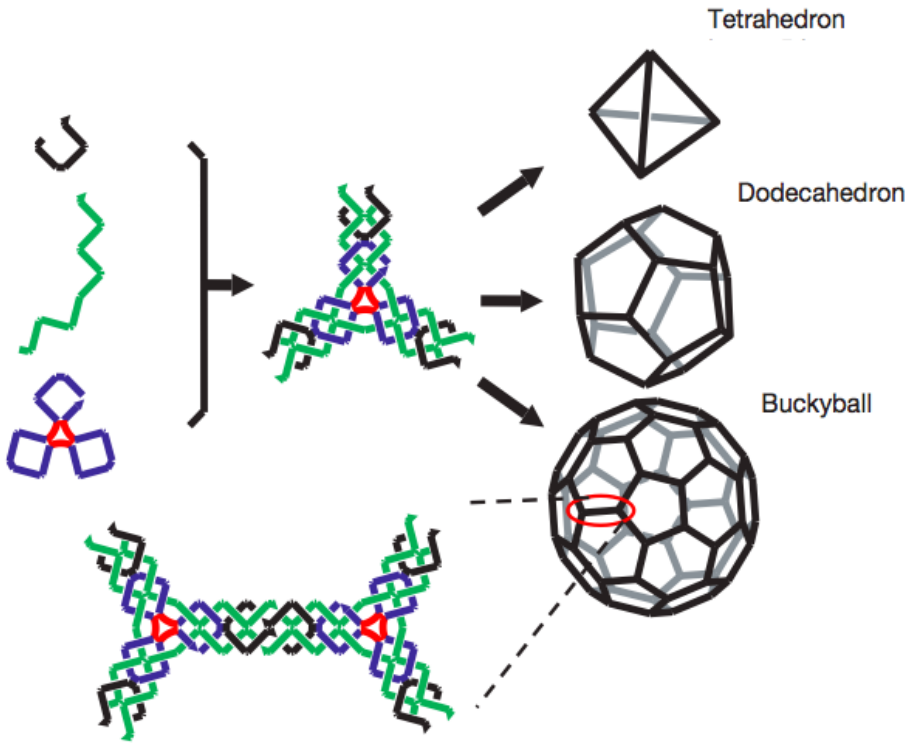

Figure 2.12: A symmetric three-arm junction assembles into a three-dimensional tetrahedron, octahedron or buckyball. Figure from [86].

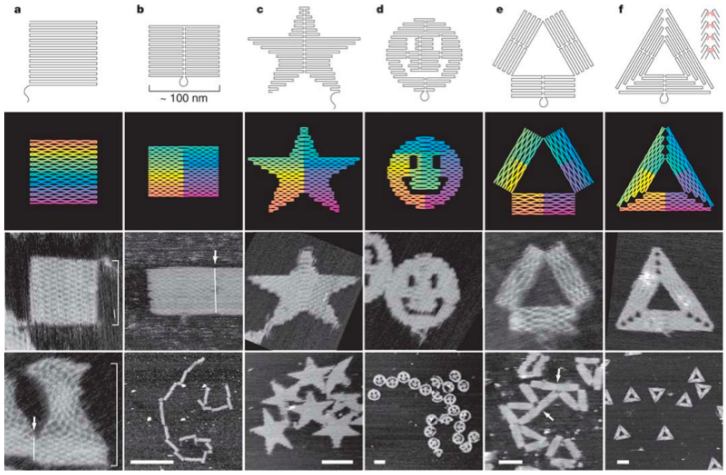

Figure 2.13: Top row: folding paths for realizing different shapes of DNA origami. Second row: diagrams showing the bend of helices at crossovers and away from them. Bottom rows: AFM visualization of the structures. Figure from [88].

DNA origami As shown, DNA tiles are useful for the assembling of ordered and periodic structures with high stability; anyhow, they do not allow for design flexibility. In this respect, the self-assembly of 2D and 3D patterns with increasing complexity was greatly facilitated by the advent of DNA origami, a completely innovative DNA-based design method able to create potentially any shape by simply programming the nanoscale folding of a single continuous ss-DNA used as a 'scaffold', using a larger number of smaller DNA strands.
The first experiment in this direction was performed in 2003 and it led to the self-assembly of multiple DNA tiles (DX molecules) around a scaffold DNA strand for the realization of a patterned DNA lattice displaying barcode information [87].
However, it was thanks to the dramatic impact of Rothermund's scaffold DNA origami [88] that this new approach to the design of self-assembled DNA patterns started to develop. Indeed, in his work, Rothermund folded a viral single stranded DNA from the bacteriophage M13 (whose sequence of 7249 has been completely sequenced) into a variety of beautiful and complex 2D structures such as squares, disks, smiley faces and stars (Fig. 2.13) by using a number of short oligomers, called staples. Such staple strands were computationally designed to selectively hybridize specific sites of the long scaffold DNA, thus forcing the long sequence to fold several times in a controllable fashion. Later on, using this technique, researchers have assembled a large variety of 3D structures including boxes, gears, and vases [89, 90, 91].
It is worth to note that many rules that need to be strictly respected for the correct self-assembly of DNA tiles are not necessary in this method, e.g. sequence design, strand purity and rigorous concentration ratios of the strands. In addition it also provides an easy way to obtain high yields of well-formed structures, thus displaying great potentialities for the extensive assembly of large DNA patterns.

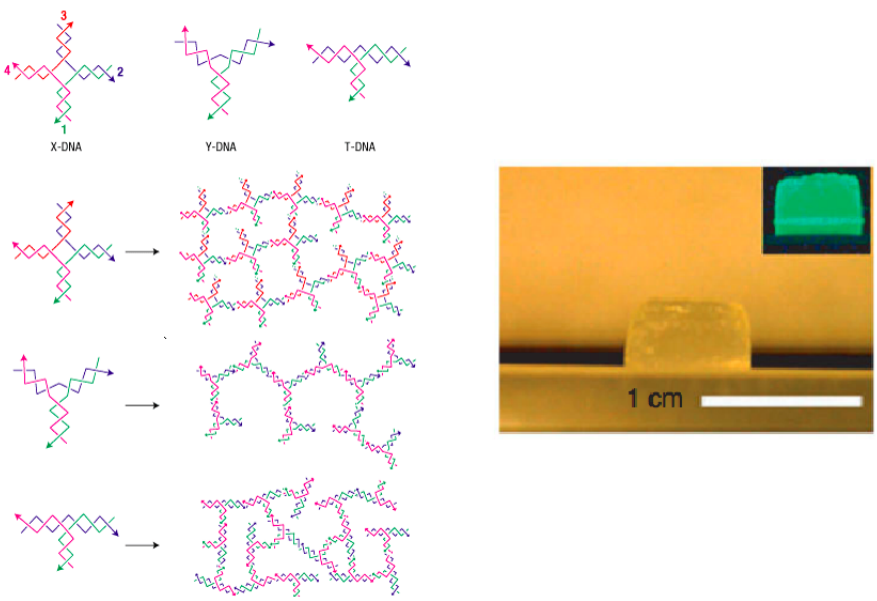

Figure 2.14: On the left: Different branched structures giving rise to network of bonded structures. On the right: X-DNA hydrogel synthesized in a cylindrical mould. The inset shows the DNA gel stained with a specific dye (SYBR I). Figure adapted from [92].

Hydrogels The last class of networked DNA structures is composed by DNA hydrogels, i.e. amorphous water-swollen cross-linked DNA networks that typically extend over macroscopic volumes.
The ability of creating networked DNA materials on a bulk scale is fundamental for real-world applications: thus, a special attention must be paid on the efficiency and on the total yield for the synthesis of DNA hydrogels.
Recently, different methods have been developed to obtain bulk quantities of such gels, including enzyme ligation, chemical crosslinking and physical interactions.
For instance, using enzyme ligation, Luo et al. realized DNA hydrogels made of branched DNAs such as X-DNA, Y-DNA and T-DNA (which acted as both monomers and crosslinkers), interacting through self-complementary sticky ends (Fig. 2.14) [92].
After the hybridization of the sticky ends, enzymatic ligation by T4 ligase under physiological conditions was used to permanently fix the bonds between different star-shaped units in the network.
Specifically, in their scheme, the gel synthesis started with the realization of branched DNA structures through base-pairing interactions among oligonucleotides; subsequently, different branched DNAs were made adhering via sticky-ended cohesion and their bonds were stabilized by the use of T4 ligase.
Interestingly, they showed that the topological properties of such gels could be easily tuned by simply adjusting the types and concentrations of the branched monomers

in the initial reaction mixture, thus allowing the hydrogels to be suitable for innovative applications such as programmable drug delivery, tissue engineering, tridimensional cell culture and a large variety of biomedical applications.
Indeed, such gelling processes were obtained under physiological conditions, enabling biomaterials (e.g. proteins, drugs and living mammalian cells) to be encapsulated within the matrix of the gel in situ, thus offering an innovative strategy for programmable drug delivery.
Moreover, the described programmability and biocompatibility make such DNA gels appealing as scaffolding systems for several biomedical applications, e.g. protein expression. Indeed, for instance, Prof. Luo's group used a DNA hydrogel (called 'P-gel'), as a scaffold for cell-free protein production resulting in a 300-fold protein yield over commercially available cell-free systems [93].

2.2.4 DNA as a smart glue for organizing nanoparticles

A conclusive remark must be made onto a completely different approach regarding DNA as a smart glue to organize nanoparticles without using pre-assembled scaffolds.
Typically, such method involves the use of a solution of surface modified gold nanoparticles (AuNP) presenting end labelled thiolated ss-DNA (DNA-coated nanoparticles) to whom complementary ss-DNA are added.
Using this approach, Mirkin et al. [94] achieved the realization of a first example of DNA-based sensing, by creating DNA–AuNP polymeric networks able to cause a red-to-pinkish/purple color change in solution after the proper hybridization to the target ss-DNA oligonucleotides, a finding which is currently at the basis of all the DNA sensors present on the market.
Later on, the attention was focussed on the possibility of self-assembling extended regular crystalline arrays. Independently, the groups of Mirkin [95] and Gang [96] reported the successful realization of tridimensional gold nanoparticle crystals, by programming the AuNP to self-assemble into face-centered cubic and body-centered cubic crystal structures of micrometrical dimensions.

Part II

Experimental Section

Chapter 3

Methods

"Truth is what stands
the test of experience"

Albert Einstein

As stated in the introduction, this thesis is mainly dedicated to the experimental study of the phase behaviour of limited-valence DNA nanostars. As we will discuss in the following chapters, such constructs represent an interesting model system to investigate from both structural and dynamical standpoints. Anyhow, given the intrinsic complexity of biological and soft systems, an accurate experimental characterization of the structural and dynamical properties of the self-assembling nanostars may result rather challenging. To overcome such challenge, we synergistically used a variety of experimental techniques, in order to achieve a complete depiction of the system through a comparative analysis of the results obtained from the different approaches.
In the present chapter we thus describe the main techniques that we used to experimentally investigate the behaviour of our limited-valence particles. Specifically, since the experiments were mainly based on Dynamic Light Scattering, we provide a detailed overview on this method, following mainly Ref. [97, 98], showing how it can be used to investigate the dynamics of network-forming systems as well as to monitor the approach to thermodynamics instability at low temperatures. Moreover, we show how the intensity scattered by the samples can be used to study critical phenomena taking place in the scattering media and to estimate the relevant critical parameters.
Subsequently, we focus on a method widely used in molecular biology to follow the hybridization processes of nucleic acids, i.e. UV absorption, explaining how it can be used to evaluate the melting temperatures of DNA strands as well as to check the purity of synthetic DNA oligomers. Furthermore, a special attention is paid on Atomic Force Microscopy, a very high-resolution type of scanning probe microscopy with a demonstrated resolution on the order of fractions of a nanometer, i.e. more than 1000 times better than the optical diffraction limit. Eventually, in the last section, we provide a very brief overview on gel electrophoresis, a technique widely used in biology for separating mixed population of nucleic acids by length.

3.1 Dynamic Light Scattering

Light is an element of primary importance for the experimental study of biological soft matter since it constitutes a direct and not perturbative probe capable of characterizing structural and dynamical properties of the investigated samples. Specifically, light scattering (static or dynamic) is a noninvasive, highly sensitive technique which allows for the analysis of the behaviour of biological macromolecules in solution. In particular, static light scattering allows to measure static properties, as the shape or the mass of the scattering particles, whereas dynamic light scattering allows to investigate dynamic properties such as diffusion coefficients and hydrodynamic radii.

3.1.1 Basic Theory of Light Scattering

All the light scattering experiments rely on a specific optical property of matter, i.e. its capability of diffusing light.
Diffusion phenomena derive from inhomogeneities in the refractive index of the scattering medium. Indeed, while in perfectly homogeneous media light is scattered only forward (i.e. along the direction of the incident beam), in non-homogeneous media, eventual variations in the refractive index may cause light to be diffused also laterally. In general, when photons impinge on a molecule they can either impart or even receive energy from its translational, rotational, vibrational and electronic degrees of freedom. The scattered light thereby suffers frequency shifts which are due to such degrees of freedom of the molecules[1].
In general, when electromagnetic radiation interacts with matter, the electric field induces an oscillating polarization of the electrons in the molecules that consequently act as secondary sources of radiation. The frequency shifts, the angular distribution, the polarization and the intensity of the scattered light are determined by the size, the shape and the molecular interactions in the scattering medium. Thus, from the characteristics of the light scattered by a given system, with the aid of electrodynamics and the theory of the time-dependent statistical mechanics, it becomes possible to extract structural and dynamical information on the investigated system.
In a typical light scattering experiment, a monochromatic beam emitted from a laser with wavelength λ_i, wavevector k_i and a well-defined polarization is focussed on a sample with unknown characteristics. The scattered light, with wavevector k_s, is collected by a detector placed at an angle θ between the incident and the scattered beam (Fig. 3.1). The volume of the sample illuminated by the incident beam is commonly named "scattering volume". Typically, in a scattering experiment, the scattering volume is controlled through the use of apertures, slits or walls of the sample cell, or by optical elements such as lenses.

[1] The present thesis deals with the characteristics of the light scattered only from translational and rotational degrees of freedom, i.e. with Rayleigh scattering (in this case the energy of the incident photon is conserved and only its direction is changed).

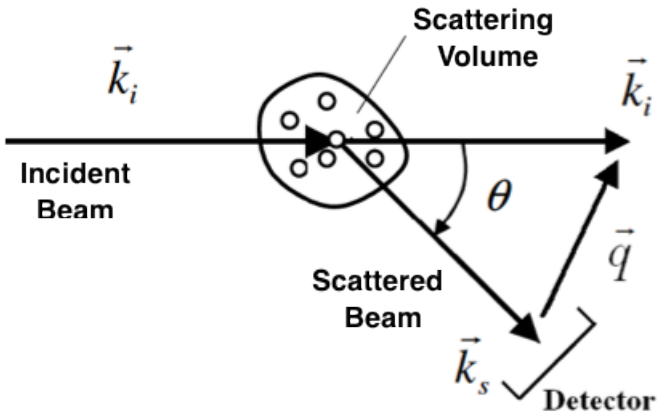

Figure 3.1: Schematic representation of a light scattering experiments, showing the scattering vector **q**.

In the description of light scattering process, a key role is played by the scattering vector $\mathbf{q} = \mathbf{k}_i - \mathbf{k}s$, which represents the transferred momentum in the light-matter interaction. Here the magnitude of the propagation vectors are given by $|\mathbf{k_i}| = 2\pi n/\lambda_i$ and $|\mathbf{k_s}| = 2\pi n/\lambda_s$, where λ_i and λ_s represent respectively the wavelengths in vacuum of the incident and of the scattered beam and n is the refractive index of the scattering medium. Assuming a "quasielastic" scattering process, we have that the wavelength of the incident light is changed very little and, hence:

$$|\mathbf{k_i}| \backsimeq |\mathbf{k_s}| \tag{3.1}$$

Thus, the triangle in Fig. 3.1 is isosceles and the magnitude of **q** is given by:

$$q = \sqrt{|\mathbf{k_i} - \mathbf{k_s}|^2} = \sqrt{|\mathbf{k_i}|^2 + |\mathbf{k_s}|^2 - 2\mathbf{k_i} \cdot \mathbf{k_s}} = \sqrt{2|\mathbf{k_i}|^2 - |\mathbf{k_i}|^2 cos\theta} =$$

$$= \sqrt{4|\mathbf{k_i}|^2 sin^2\frac{\theta}{2}} = \frac{4\pi n}{\lambda_i} sin\frac{\theta}{2} \tag{3.2}$$

Description in terms of the classical theory of electromagnetism

In an ideal experiment, the incident light can be considered as a plane-wave:

$$\mathbf{E}_i(\mathbf{r}, t) = \mathbf{p}_i E_0 e^{i(\mathbf{k_i r} - \omega_i t)} \tag{3.3}$$

where $\mathbf{p}_i$ is the polarization, E_0 the amplitude, $\mathbf{k_i}$ the propagation vector (or wave vector) and ω_i the angular frequency of the incident electric field. Such plane-wave impinges on a medium with a local dielectric constant:

$$\boldsymbol{\varepsilon}(\mathbf{r}, t) = \varepsilon_0 \mathbf{I} + \delta\boldsymbol{\varepsilon}(\mathbf{r}, t) \tag{3.4}$$

where $\delta\boldsymbol{\varepsilon}(\mathbf{r},t)$ is the dielectric constant fluctuation tensor at position $\mathbf{r}$ and time t, ε_0 is the average dielectric constant of the medium and $\mathbf{I}$ is the second-order unit tensor. In the following description of light scattering, we assume that the scattering is weak, which means that:

1. most of the photons pass through the sample undeviated (and few of them are scattered only once) so that the probability of multiple scattering is negligible;

2. the incident beam is not significantly distorted from the medium (Rayleigh-Gans-Debye approximation);

3. the scattering process is "quasielastic", causing only a very small variation in the frequency. Hence, as seen, the propagation vector of the scattered beam is equal, in modulus, to the propagation vector of the incident beam.

An important factor for the realization of a light scattering measurement is the refractive index of the particles. Indeed, if the refractive index of the particles is too different from that of the surrounding fluid, it can produce a significant phase shift of the incident wave between the region of the medium and the one inside a particle. In order to avoid it, the phase shift must be:

$$\Delta\phi = 2\pi[n_p - n_s]\frac{a}{\lambda_0} \ll 1 \tag{3.5}$$

where n_p denotes the refractive index of the particle, n_s the one of the solvent, a the radius of the particle e λ_0 the wavelength of the light in vacuum. Eq. 3.5 also ensures that refraction of light at the interface fluid/particle is negligible. Therefore, the direction of the incident wave is undeviated inside the scattering volume and eq. 3.3 gives a good description of the incident wave also inside the sample.
On the other hand, a refractive index too similar to the one of the medium must also be avoided since molecules optically indistinguishable from the medium do not diffuse light.
Indeed, light scattering is intrinsically related to the optical properties of the sample, which are described by its local dielectric constant. Therefore, by applying the Maxwell's equations to the problem of a plane electromagnetic wave propagating in a medium with a local dielectric constant given by Eq. 3.4, it is possible to demonstrate [97] that the amplitude $E_s(\mathbf{R},t)$ of the electric field of the radiation scattered to a point detector at position $\mathbf{R}$ in the far field is given by:

$$E_s(\mathbf{R},t) = \frac{E_0}{4\pi\varepsilon_0}\frac{e^{i(ksR-\omega_i t)}}{R}\int_V e^{-i\mathbf{q}\cdot\mathbf{r}}[\mathbf{p}_s\cdot[\mathbf{k}_s\times(\mathbf{k}_s\times(\delta\boldsymbol{\varepsilon}(\mathbf{r},t)\cdot \mathrm{p}_i))]]d^3\mathrm{r} \tag{3.6}$$

where V indicates the scattering volume, $\mathbf{q}$ the scattering vector and $\mathbf{p_s}$ the polarization of the scattered electric field.
Last equation embodies all the fundamental physics of light scattering. The scattered field consists of a spherical wave emanating from the scattering volume with a

q-dependent amplitude which is the spatial Fourier transform of instantaneous variations in the dielectric constant of the sample. Indeed, Eq.3.6 clearly shows that, if the medium is totally homogeneous, i.e. $\delta\boldsymbol{\varepsilon}(\mathbf{r},t)=0$, there cannot be any scattering process. In other words, such equation suggests that light scattering is due to the spatial fluctuations in the dielectric properties of the scattering medium.
Eq. 3.6 can be simplified by working out the vector cross products, by using the identity $A\times(B\times C)=B(A\cdot C)-C(A\cdot B)$:

$$E_s(\mathbf{R},t)=-\frac{k_s^2E_0}{4\pi\varepsilon_0}\frac{e^{i(ksR-\omega_it)}}{R}\int_V e^{-i\mathbf{q}\cdot\mathbf{r}}\delta\varepsilon_{is}(\mathbf{r},t)d^3\mathrm{r} \tag{3.7}$$

where $\delta\varepsilon_{is}(\mathbf{r},t)\equiv\mathbf{p}_s\cdot\delta\boldsymbol{\varepsilon}(\mathbf{r},t)\cdot\mathbf{p_i}$ is the component of the dielectric constant fluctuation tensor along the initial and final polarization directions.
Eq. 3.7 can thus be rewritten as the sum of the amplitudes of the fields $dE_s(\mathbf{R},t)$ scattered by the volume elements $dV\equiv d^3\mathrm{r}$ at position r:

$$E_s(\mathbf{R},t)=\int_V dE_s(\mathbf{R},t) \tag{3.8}$$

where:

$$dE_s(\mathbf{R},t)=-\frac{k_s^2E_0}{4\pi\varepsilon_0}\frac{e^{i(k_sR-\omega_it)}}{R}e^{-i\mathbf{q}\cdot\mathbf{r}}\delta\varepsilon_{is}(\mathbf{r},t)d^3\mathrm{r} \tag{3.9}$$

It is interesting to note that eq. 3.6, 3.7 and 3.9 have been written in general tensor notation and are therefore independent from the laboratory coordinate system used for the scattering experiment.
Later on, we will show how the scattering intensity (that can be calculated from the scattered field by using the relation $I_s(\mathbf{R},t)=|E_s(\mathbf{R},t)|^2$), averaged over time, can provide information on the structure and dynamics of the investigated samples, by simply looking at the spatial correlations between particles. Indeed, variations in time of the local dielectric constant are directly reflected in temporal variations of the amplitude and intensity of the scattered field.

Discrete Scatterers

In the case of a sample containing discrete scattering particles suspended in a liquid, it possible to write the scattered electric field as a function of:

- the position $\mathbf{R_j}(t)$ of the center of mass of the particle j at the time t;
- the position $\mathbf{r_j}(t)$ of the infinitesimal volume elements ($dV_j=d^3\mathrm{r}_j$) in particle j relative to its center of mass (Fig. 3.2).

Considering N particles suspended in a scattering volume V, it is possible to show [98] that eq. 3.7 becomes:

$$E_s(\mathbf{R},t)=-\frac{k_s^2E_0}{4\pi}\frac{e^{i(k_sR-\omega_it)}}{R}\times\sum_j^N\left\{\int_V[\frac{\varepsilon_P(\mathbf{r_j},t)-\varepsilon_L}{\varepsilon_0}]e^{-i\mathbf{q}\cdot\mathbf{r_j}}d^3r_j\right\}e^{-i\mathbf{q}\cdot\mathbf{Rj}(t)} \tag{3.10}$$

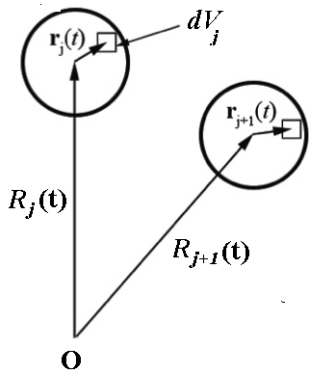

Figure 3.2: Coordinates for discrete scatterers. Relative to an arbitrary origin O, $\mathbf{R_j}(t)$ is the position of the center of mass of particle j at time t and $\mathbf{r_j}(t)$ is the position of volume element dVj in particle j, relative to its center of mass.

where $\varepsilon_P(\mathbf{r_j}, t)$ is the local dielectric constant in the position $\mathbf{r_j}$ in particle j, ε_L the average dielectric constant of the liquid and ε_0 the average dielectric constant of the entire suspension.
Eq. 3.10 can be rewritten by introducing:

$$\triangle\rho(\mathbf{r_j}, t) = \frac{k^2}{4\pi}[\frac{\varepsilon_P(\mathbf{r_j}, t) - \varepsilon_L}{\varepsilon_0}] \tag{3.11}$$

so that:

$$E_s(\mathbf{R}, t) = -E_0\frac{e^{i(k_sR-\omega_it)}}{R} \times \sum_j^N \left\{ \int_V \triangle\rho(\mathbf{r_j}, t)e^{-i\mathbf{q}\cdot\mathbf{r_j}}d^3r_j \right\} e^{-i\mathbf{q}\cdot\mathbf{Rj}(t)} \tag{3.12}$$

Assuming that the "background" scattering due to spontaneous fluctuations in the liquid itself is negligible, it is evident that the strength of the scattering depends on the difference between the dielectric properties of the particle and those of the liquid. The quantity $\triangle\rho(\mathbf{r_j}, t)$ can be regarded as a measure of the *local density of scattering material*.
Moreover, by defining the *scattering length* of particle j as:

$$b_j(\mathbf{q}, t) = \int_{V_j} \triangle\rho(\mathbf{r_j}, t)e^{-i\mathbf{q}\cdot\mathbf{r_j}}d^3r_j \tag{3.13}$$

(where V_j is the volume of particle j) it is possible to rewrite eq. 3.12 as:

$$E_s(\mathbf{R}, t) = -E_0\frac{e^{i(k_sR-\omega_it)}}{R} \times \sum_j^N b_j(\mathbf{q}, t)e^{-i\mathbf{q}\cdot\mathbf{R_j}(t)} \tag{3.14}$$

Such equation clearly indicates that the total scattered field is given by the sum of the fields scattered by the individual particles. Each of these terms is the product of a

scattering length, determined by the instantaneous distribution of material within the particle, and a phase factor determined by the instantaneous position of the particles in the sample.
Actually, in a light scattering experiment, one directly measures the scattered intensity rather than the electric field. In this respect, considering that $I_s(\mathbf{q},t) = |E_s(\mathbf{q},t)|^2 = E_s(\mathbf{q},t)E_s^*(\mathbf{q},t)$, it is possible to obtain an expression for the instantaneous scattered intensity:

$$I_s(\mathbf{q},t) = \frac{E_0^2}{R^2}\sum_j^N\sum_k^N b_j(\mathbf{q},t)b_k^*(\mathbf{q},t)e^{-i\mathbf{q}\cdot[\mathbf{R_j}(t)-\mathbf{R_k}(t)]} \tag{3.15}$$

Structural information on the investigated sample can be obtained by the ensemble average of the intensity, which is equivalent to the time average when the scattering medium is ergodic:

$$< I_s(\mathrm{q}) >= \frac{E_0^2}{R^2} < \sum_j^N\sum_k^N b_j(\mathbf{q})b_k^*(\mathbf{q})e^{-i\mathbf{q}\cdot[\mathbf{R_j}-\mathbf{R_k}]} > \tag{3.16}$$

By writing the averaged scattered intensity as a function of the modulus of the scattered vector, we have assumed that the sample is on average spatially isotropic (as expected for a "liquid-like" dispersion or solution).

Scattering from non interacting particles

Let us consider a dilute system, i.e. a system composed by individual particles which are, on average, widely spatially separated. If the concentration of such particles is low enough, scatterers are independent from each others and their behaviours can be considered uncorrelated. Neglecting the pre-factor, eq. 3.16 can be written as:

$$< I_s(\mathbf{q},\mathrm{t}) >= \sum_j^N < |b_j(\mathbf{q},\mathbf{t})|^2 > + \sum_j^N\sum_k^N < b_j(\mathbf{q},\mathrm{t})e^{-i\mathbf{q}\cdot[\mathbf{R_j}(t)]} >< b_k^*(\mathbf{q},\mathrm{t})e^{-i\mathbf{q}\cdot[\mathbf{R_k}(\mathbf{t})]} > \tag{3.17}$$

Considering that over time, the particle j can occupy any position in the sample, unaffected by the position of the other ones, the exponential terms are randomly distributed around zero and $< b_j(\mathbf{q},\mathrm{t})e^{-i\mathbf{q}\cdot[\mathbf{Rj}(t)]} >= 0$.
Hence, in the limit of non interacting particles, the averaged scattered intensity is given by the sum of the averaged intensities scattered by the individual particles.
Moreover, assuming that the particles are identical (i.e. that the averaged intensities scattered by the particles are the same) last equation becomes:

$$< I_s(\mathbf{q}) >= N < |b(0)|^2 P(\mathbf{q}) > \tag{3.18}$$

where $P(\mathbf{q}) = \frac{<|b(\mathbf{q})|^2>}{<|b(0)|^2>}$ is the **form factor** of the particle, which gives information on the size, structure and shape of the particle, averaged over orientation and over any distribution of size and shape.

Focussing on the scattered fields in the simple case of identical non-interacting spherical particles, eq.3.14 can be rewritten as:

$$E_s(\mathbf{q},t) = \sum_j^N e^{-i\mathbf{q}\cdot\mathbf{R_j}(t)} \tag{3.19}$$

where we have omitted the pre-factors and considered that all the scattering lengths $b_j(\mathbf{q},t)$ have the same time-independent value $b_j(\mathbf{q}) = b(q)$.
The scattered electric field, given by the vectorial sum of N electric fields generated by the scattering of randomly distributed particles, can be thought as a 2D random walk of N vectors. Indeed, since the positions of the particles are totally uncorrelated, the phase angles are homogeneously distributed in the interval $[0 : 2\pi]$. Moreover, due to the the Brownian motion of the scatterers the positions $\mathbf{R_j}(t)$ and the phase angles $\mathbf{q}\cdot\mathbf{R_j}(t)$ change and the fluctuations of the scattered fields become completely uncorrelated over time. In such conditions, the average value of the scattered field is:

$$< E_s(\mathbf{q},t) >= \sum_j^N < e^{-i\mathbf{q}\cdot\mathbf{R_j}(t)} >= 0 \tag{3.20}$$

while the average scattered intensity becomes:

$$\begin{aligned} < I_s(\mathbf{q},t) >=< |E_s(\mathbf{q},t)|^2 >= \sum_j^N \sum_k^N < e^{-i\mathbf{q}\cdot[\mathbf{R_j}(t)-\mathbf{R_k}(t)]} >= \\ = \sum_j^N 1 + \sum_{j\neq k}^N < e^{-i\mathbf{q}\cdot\mathbf{R_j}(t)} >< e^{-i\mathbf{q}\cdot\mathbf{R_k}(t)} >= N \end{aligned} \tag{3.21}$$

where, in averaging the cross-terms ($i \neq j$) separately, we have used the assumption that in dilute systems particle positions are uncorrelated.

Scattering from interacting particles

In a highly concentrated solution of particles, mutual interactions prevail on thermal fluctuations. As a consequence, particles interact with each other, assuming positions that are correlated to one another. This reciprocal interaction is formally expressed through the structure factor $S(q)$, defined as:

$$S(q) = \frac{1}{N}\sum_j^N \sum_k^N < e^{-i\mathbf{q}\cdot[\mathbf{R_j}(t)-\mathbf{R_k}(t)]} > \tag{3.22}$$

which modulates the shape of the scattering intensity:

$$< I_s(\mathbf{q}) >= Nb(0)^2 P(\mathbf{q}) S(q) \tag{3.23}$$

where, for simplicity, we have assumed that the particles are homogeneous identical spheres, so that all $b_j(\mathbf{q}) = b(q)$. Clearly, in dilute systems where particle positions are uncorrelated, cross-terms in eq. 3.23 vanish and $S(q) = 1$.

3.1.2 Dynamic Light Scattering

Dynamic Light Scattering (DLS) or Photon Correlation Spectroscopy (PCS) is one of the most powerful techniques to investigate the dynamics of colloids, emulsions, polymers and biological macromolecules.
Its basic principle is rather simple: a scattering medium, e.g a solution of colloidal particles, is illuminated by monochromatic light and a detector, located at a scattering angle θ, collects the fluctuations of the scattered intensity. At any instant, the pattern of scattered light collected by the detector is constituted by a grainy random diffraction or "speckle" pattern (Fig. 3.3).

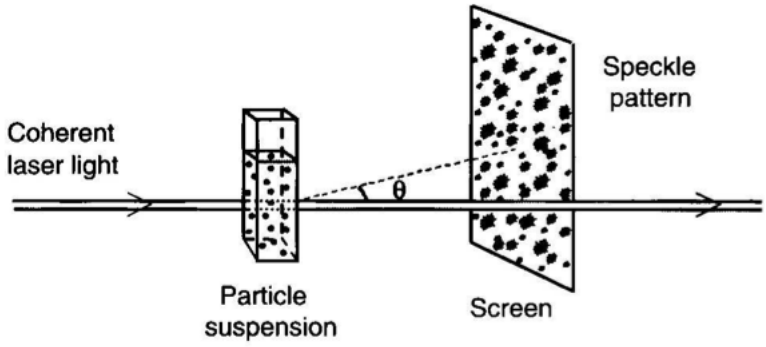

Figure 3.3: Schematics of a DLS experiment, showing the speckle pattern. Figure from [98].

Indeed, phase interference between the light scattered by the individual particles usually yields to regions of large and small intensities. Moreover, since the scattering medium is constantly changing with time (as the particle positions $\mathbf{R}j(t)$ change due to Brownian motion), the speckle pattern is not static but it rather fluctuates from one random configuration to another.
In a typical dynamic light scattering experiment, one focus on a small group of speckles, analyzing the intensity fluctuations in the specific region of the collector surface. Such random fluctuations encode structural and dynamical information about the positions of the scattering particles.

Fluctuations and time-correlation functions

In order to obtain information from the intensity fluctuations, we can simply consider the time average:

$$< I_s(\mathbf{q}, t_0, T) >= \frac{1}{T} \int_{t_0}^{t_0+T} I_s(\mathbf{q}, t) dt \tag{3.24}$$

where t_0 is the starting time of the measurement and T is the time over which the measurement is averaged (therefore, T must be larger than the period of the fluctuations).

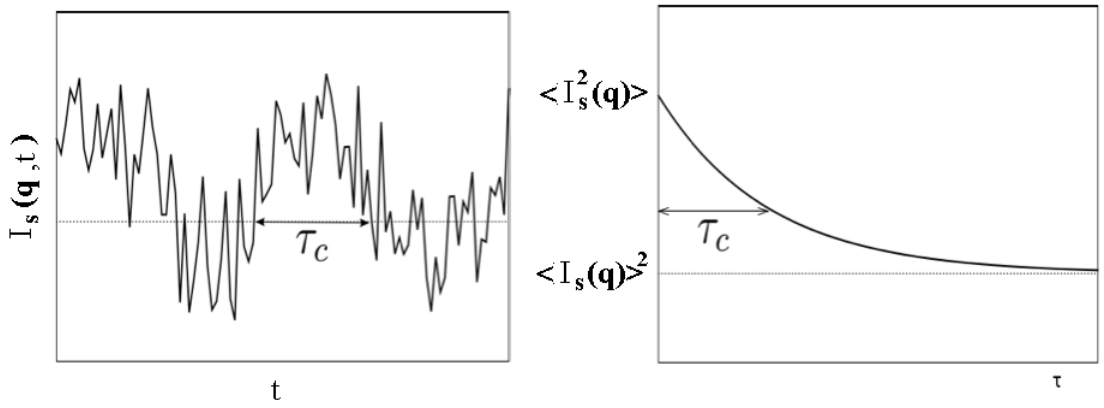

Figure 3.4: Fluctuations of the scattering intensity (left panel) and intensity correlation function (right panel). The time-dependent part of the correlation function decays with a time constant τ_c which is equal to the characteristic time of the intensity fluctuations.

Clearly, in an ideal experiment the average would be done over an infinite time:

$$< I_s(\mathbf{q}, t_0, T) >= \lim_{T\to\infty} \frac{1}{T} \int_{t_0}^{t_0+T} I_s(\mathbf{q}, t)dt \tag{3.25}$$

It can be shown that this infinite time average is independent from the starting time t_0 (i.e. the scattering intensity is a stationary property of the system since its average is independent of t_0 []). Subsequently, eq. 3.25 can be written as:

$$< I_s >= \lim_{T\to\infty} \frac{1}{T} \int_{0}^{T} I_s(\mathbf{q}, t)dt \tag{3.26}$$

In general, the intensity of the light scattered at two different instants will give two different values $I_s(\mathbf{q}, t+\tau) \neq I_s(\mathbf{q}, t)$. Anyhow, if τ is very small compared to the characteristic time $\tau_{_C}$ of the fluctuations (Fig. 3.4, left panel), $I_s(\mathbf{q}, t+\tau)$ will result very close to $I_s(\mathbf{q}, t)$.. As τ increases, the deviation of $I_s(\mathbf{q}, t+\tau)$ from $I_s(\mathbf{q}, t)$ will be larger. Hence, the two values are correlated when τ is small, while the correlation is lost as τ becomes larger than $\tau_{_C}$. Such behaviour, typical of stochastic variables, is well-described by the intensity autocorrelation function, which is defined as:

$$< I_s(\mathbf{q}, 0)I_s(\mathbf{q}, \tau) >= \lim_{T\to\infty} \frac{1}{T} \int_{0}^{T} I_s(\mathbf{q}, t)I_s(\mathbf{q}, t+\tau) \tag{3.27}$$

For zero delay eq. 3.27 reduces to:

$$\lim_{\tau\to 0} < I_s(\mathbf{q}, 0)I_s(\mathbf{q}, \tau) >=< I_s^2(\mathbf{q}) > \tag{3.28}$$

For delay times much greater than τ_c, $I_s(\mathbf{q}, t)$ and $I_s(\mathbf{q}, t+\tau)$ are uncorrelated and the average in Eq. 3.27 can be separated:

$$\lim_{\tau\to\infty} < I_s(\mathbf{q}, 0)I_s(\mathbf{q}, \tau) >=< I_s(\mathbf{q}) >< I_s(\mathbf{q}, \tau) >=< I_s(\mathbf{q}) >^2 \tag{3.29}$$

The scattered intensity is a nonconserved and nonperiodic property of the system: its autocorrelation function, thus, decays from the mean of the squared intensity $< I_S^2(\mathbf{q}) >$ to the square of the mean intensity $< I_S(\mathbf{q}) >^2$ in the course of time. The characteristic time of the decay is a measure of the typical time of the intensity fluctuations (Fig. 3.4, right panel).

3.1.3 Dynamic Investigation using Dynamic Light Scattering

In a typical light scattering experiment, the output provided by the instrument is the intensity auto-correlation function, which is directly calculated from a digital correlator through a discrete representation of eq. 3.27:

$$g_2(\tau) = \lim_{N\to\infty} \frac{1}{N} \sum_{i}^{N} I_s(t_i) I_s(t_i + \tau) dt \tag{3.30}$$

Actually, the interesting physical information are contained in the auto-correlation function of the scattered fields, which can be defined as:

$$g_1(\mathbf{q}, \tau) \equiv \frac{< E_s(\mathbf{q}, 0) E_s^*(\mathbf{q}, \tau) >}{I_s(\mathbf{q})} \tag{3.31}$$

where $I_S(\mathbf{q}) =< E_S(\mathbf{q}, 0) E_S^*(\mathbf{q}, 0) >$ is a normalizing factor.
By substituting eq. 3.19 in eq. 3.31, we obtain for $g_1(\mathbf{q}, \tau)$ the expression:

$$g_1(\mathbf{q}, \tau) = \frac{1}{N} \sum_{j}^{N} < e^{-i\mathbf{q}\cdot[\mathbf{R_j}(0) - \mathbf{R_j}(\tau)]} >=< e^{-i\mathbf{q}\cdot[\mathbf{R}(0) - \mathbf{R}(\tau)]} > \tag{3.32}$$

where we have assumed that the average motions of identical particles are equal.
In order to find the relation between g_2, which is determined experimentally , and g_1, which contains the physical information, the intensity autocorrelation function must be explicitly calculated:

$$< I_s(\mathbf{q}, 0) I_s(\mathbf{q}, \tau) >= \sum_{j,k,l,m}^{N} < e^{-i\mathbf{q}\cdot[\mathbf{R_j}(0) - \mathbf{R_k}(0) + \mathbf{R_l}(\tau) - \mathbf{R_m}(\tau)]} >= \tag{3.33}$$

$$= N^2 + N^2 | < e^{-i\mathbf{q}\cdot[\mathbf{R_j}(0) - \mathbf{R}(\tau)]} > |^2 \tag{3.34}$$

By using the definition of the normalized intensity autocorrelation function

$$g_2(\mathbf{q}, \tau) \equiv \frac{< I_s(\mathbf{q}, 0) I_s(\mathbf{q}, \tau) >}{| < I_s(\mathbf{q}, 0) > |^2} \tag{3.35}$$

together with eq. 3.21, 3.31 and 3.33, it is possible to obtain the so-called *Siegard relation:*

$$g_2(\mathbf{q}, \tau) = 1 + |g_1(\mathbf{q}, \tau)|^2 \tag{3.36}$$

To take into account the experimental conditions, eq. 3.36, must be modified to:

$$g_2(\mathbf{q},\tau) = 1 + \beta|g_1(\mathbf{q},\tau)|^2 \tag{3.37}$$

where β is a parameter which represents the degree of spatial coherence of the scattered light on the detector surface. Specifically, β depends on the ratio between the detection area and the area of one speckle: if such ratio is much smaller than 1 (point detector), $\beta \to 1$; if, instead, the detector collects many independently fluctuating speckles $\beta \to 0$. In DLS experiments, the detector aperture is usually chosen to accept approximately one speckle so that $\beta \sim 1$.
Moreover, another important parameter that is commonly introduced in eq. 3.36 is the baseline value (B), which correspond to the value that the intensity autocorrelation function assumes for long times:

$$g_2(\mathbf{q},\tau) = B(1 + \beta|g_1(\mathbf{q},\tau)|^2) \tag{3.38}$$

Intermediate scattering function

One important point to stress is that, although eq. 3.36 was derived in the hypothesis of no spatial correlations between particles, it can be applied to every system in which the range of spatial correlations is much smaller than the linear dimension of the scattering volume. Indeed, in this case, the scattering volume contains a large number of correlation volumes (i.e. portions of space where the positions of the particles are correlated) and the derivation proceeds essentially in the same way (with the correlation volumes taking the role of the independent particles).
Hence, we can extend the use of eq. 3.36 to solutions of interacting, non-identical and non spherical particles. In this case, the field correlation function, commonly named *measured intermediate scattering function* $f_M(\mathbf{q},\tau)$, can be written as:

$$g_1(\mathbf{q},\tau) = \frac{\sum_j^N \sum_k^N < b_j(\mathbf{q},0) b_j^*(\mathbf{q},\tau) e^{-i\mathbf{q}\cdot[\mathbf{R_j}(\mathbf{0}) - \mathbf{R_k}(\tau)]} >}{\sum_j^N \sum_k^N < b_j(\mathbf{q}) b_j^*(\mathbf{q}) e^{-i\mathbf{q}\cdot[\mathbf{R_j}(\mathbf{0}) - \mathbf{R_k}(\mathbf{0})]} >} \equiv f_M(\mathbf{q},\tau) \tag{3.39}$$

which, for spherical identical particles ($b_j^*(\mathbf{q},\mathbf{t}) = b(\mathbf{q})$), becomes:

$$f_M(\mathbf{q},\tau) \equiv f(\mathbf{q},\tau) \equiv \frac{F_c(\mathbf{q},\tau)}{S(\mathbf{q})} \tag{3.40}$$

where $f(\mathbf{q},\tau)$ is the normalized intermediate scattering function, $S(\mathbf{q})$ is the static structure factor and

$$F_c(\mathbf{q},\tau) = \frac{1}{N} \sum_j^N \sum_k^N < e^{-i\mathbf{q}\cdot[\mathbf{R_j}(\mathbf{0}) - \mathbf{R_k}(\tau)]} > \tag{3.41}$$

is the collective dynamic structure factor.
In experiments, $f_M(\mathbf{q},\tau)$ can be directly obtained from $g_2(\mathbf{q},\tau)$, by inverting eq. 3.38:

$$f_M(\mathbf{q},\tau) = \sqrt{\frac{(g_2(\mathbf{q},\tau)/B) - 1}{\beta}} \tag{3.42}$$

Characteristic time of the fluctuations

In the following, we discuss how it is possible to relate the brownian motion of the scatterers to the field autocorrelation function.
In first approximation, we consider only identical non-interacting spheres. By rewriting eq. 3.32 in terms of the particle displacement $\triangle\mathbf{R}(\tau) = \mathbf{R}(\tau) - \mathbf{R}(0)$ we obtain:

$$g_1(\mathbf{q},\tau) =< e^{[i\mathbf{q}\cdot\triangle\mathbf{R}(\tau)]} > \tag{3.43}$$

The particle displacement $\triangle\mathbf{R}(\tau)$ is a casual variable with a Gaussian probability distribution:

$$P(\triangle\mathbf{R}(\tau)) = \left[\frac{3}{2\pi\triangle\mathrm{R}^{\mathbf{2}}(\tau)}\right]^{\frac{3}{2}} e^{-\frac{3\triangle\mathrm{R}^{\mathbf{2}}(\tau)}{2<\triangle\mathrm{R}^{\mathbf{2}}(\tau)>}} \tag{3.44}$$

The mean square displacement of the particle is:

$$< \triangle\mathrm{R}^{\mathbf{2}}(\tau) >= 6D_0\tau \tag{3.45}$$

where D_0 is the diffusion coefficient of a free particle, given by the Stoke-Einstein relation:

$$D_0 = \frac{k_B T}{6\pi\eta R_H} \tag{3.46}$$

where k_B is the Boltzmann constant, T the absolute temperature, η the viscosity of the suspension medium and R_H the hydrodynamic radius of the particle.
The average value of eq. 3.43 calculated on the probability distribution 3.44 gives for $g_1(\mathbf{q},\tau)$ the following expression:

$$g_1(\mathbf{q},\tau) = e^{-\left[\frac{q^2}{6}\triangle\mathrm{R}^{\mathbf{2}}(\tau)\right]} = e^{-q^2 D_0\tau} = e^{-\frac{\tau}{\tau_c}} \tag{3.47}$$

where $\tau_c = \frac{1}{q^2 D_0}$ is the characteristic time of the fluctuations.
Eq. 3.47 finally gives the relation between the field autocorrelation function and the radius of the particles. By using such equation, it is thus possible to obtain the hydrodynamic radius of the particles, i.e. the radius of an equivalent particle which diffuses with the same diffusion coefficient that is experimentally determined.
Anyhow, in real experiments, particles may have slightly different dimensions: it is thus important to take into account the polydispersity of the size distribution of the particles.
In the presence of polydisperse particles, eq. 3.47 becomes:

$$g_1(\mathbf{q},\tau) = \frac{\sum_j b_j^2(q) e^{-q^2 D_j\tau}}{\sum_j b_j^2(q)} \tag{3.48}$$

where D_j is the diffusion coefficient of the particle j and the terms $b_j(q)$ represent the contribution of each particle to the scattering process. Passing to the continuum:

$$g_1(\mathbf{q},\tau) = \int P(D) e^{-q^2 D\tau} dD \qquad \int_0^1 P(D) dD = 1 \tag{3.49}$$

where $P(D)$ is the intensity-weighted distribution of the diffusion coefficients.
One important point to stress is that the the polydispersity of the size distribution implies a broadening of the characteristic times τ_c.
Indeed, in presence of polidispersity:

$$g_1(\mathbf{q},\tau) \propto e^{-\left(\frac{\tau}{\tau_c}\right)^{\beta}} \tag{3.50}$$

In such case, the mean relaxation time is given by:

$$< \tau_C >= \int_0^{\infty} e^{-\left(\frac{\tau}{\tau_c}\right)^{\beta}} dt = \frac{\tau_c}{\beta}\Gamma\left(\frac{1}{\beta}\right) \tag{3.51}$$

In eq. 3.50 we have used a stretched exponential to describe the decay of the $g_1(\mathbf{q},\tau)$, where β is commonly known as stretching exponent. In general, stretching exponents provide important indications on the steepness of the associated relaxation processes. When the stretching exponent assumes values between 0 and 1, the graph of the function results characteristically stretched (whence the name of the function). In physics, stretched exponential functions are typically used in the phenomenological description of relaxation processes in disordered systems.

3.1.4 Ornstein-Zernike theory of the scattering amplitude

Light scattering is also a powerful tool to investigate critical phenomena. Indeed, sufficiently close to a critical point, the correlation length of a system usually increases, becoming as large as the wavelength of the light used to investigate the sample. In such condition, density inhomogeneities in the scattering medium diffuse light strongly, causing a peculiar phenomenon, named "critical opalescence". Specifically, on approaching the critical point of the system, three interrelated effects can be observed:

- increase in the intensity fluctuations, which corresponds to an increase of fluctuations in the particles concentration along the $\mathbf{q}$ direction;
- increase in the isothermal compressibility of the system $K_t = -\frac{1}{V}\left(\frac{\partial V}{\partial P}\right)_{T,N}$, which can be directly related to the fluctuations in the total number of particles in the system [99]:

$$\frac{K_t}{K_t^0} = \frac{< (N - < N >)^2 >}{< N >} \tag{3.52}$$

  where $K_t^0 = \frac{1}{nk_BT}$ is the compressibility of an ideal gas;
- increase in the range of the density autocorrelation function which measures the correlations of the fluctuations of the density from its average value:

$$G(\mathbf{R_i},\mathbf{R_j}) \equiv < \{n(\mathbf{R_i}) - < n(\mathbf{R_i}) >\}\{n(\mathbf{R_j}) - < n(\mathbf{R_j}) >\} > \tag{3.53}$$

where $n \equiv < \frac{N}{V} >$. Assuming that the investigated system is spatially uniform (i.e. translationally invariant), it is possible to demonstrate that :

$$\frac{K_t}{K_t^0} = \frac{1}{n} \int G(\mathbf{r}) d\mathbf{r} \tag{3.54}$$

which shows that a divergent compressibility near the critical point corresponds mathematically to an increase in the range of the correlation function.

Therefore, in the investigation of the critical phenomena, the density correlation function plays an important role. Specifically, using eq. 3.23 and eq. 3.18 it is possible to show that [99]:

$$\frac{I_s(\mathbf{q})}{I_s^o(\mathbf{q})} = \frac{S(\mathbf{q})}{n} = \frac{1}{n} \int d\mathbf{r} e^{-iq\cdot\mathbf{r}} G(\mathbf{r}) \tag{3.55}$$

where $I_s^o(\mathbf{q})$ indicates the scattering intensity predicted if the particles of the medium were not interacting and the structure factor $S(\mathbf{q})$ is written as the spatial Fourier transform of the density-density correlation function.
Such equation shows that the intensity of the radiation scattered by the medium is changed from the value $I_s^o(\mathbf{q})$ (that it should have if the particles were not interacting) by an amount which is proportional to the Fourier transform of the density autocorrelation function.
Therefore, when the critical point is approached, the integral in eq. 3.55 becomes extremely large for small values of q. This dependence upon q is displayed in Fig. 3.5 for scattering from a binary alloy at several temperatures in the critical region.
Quantitatively, the Ornstein-Zernike theory (for an accurate description refer to [99]) demonstrates that, in the limit of $q \to 0$, $I(q)$ has a Lorentzian shape:

$$\frac{I_s(\mathrm{q})}{I_s^o(\mathrm{q})} = \frac{S(\mathrm{q})}{n} = \frac{R^{-2}}{(\xi^{-1})^2 + q^2} \tag{3.56}$$

where R^{-2} is a phenomenological parameter introduced in the derivation (sometimes called Deybe persistence length) and ξ the correlation length, that diverges as the temperature approaches the critical value.

3.1.5 Light scattering setup

A He-Ne laser having a wavelength of $\lambda = 633$ nm and a power of 17 mW has been used. The laser beam is vertically polarized (perpendicular to the plane of the paper) with a polarization ratio of 500:1. The full angle beam divergence is 0.82 mrad and its longitudinal mode frequency is approximately 252 MHz.
The laser beam is accurately focussed on the sample through the use of a lens having a focal length of 125 mm. The optical chamber is a transparent glass cell, containing deionized milli-Q water which is used as an index matching fluid with the specific aim of minimizing the refraction of the scattered light through the walls.

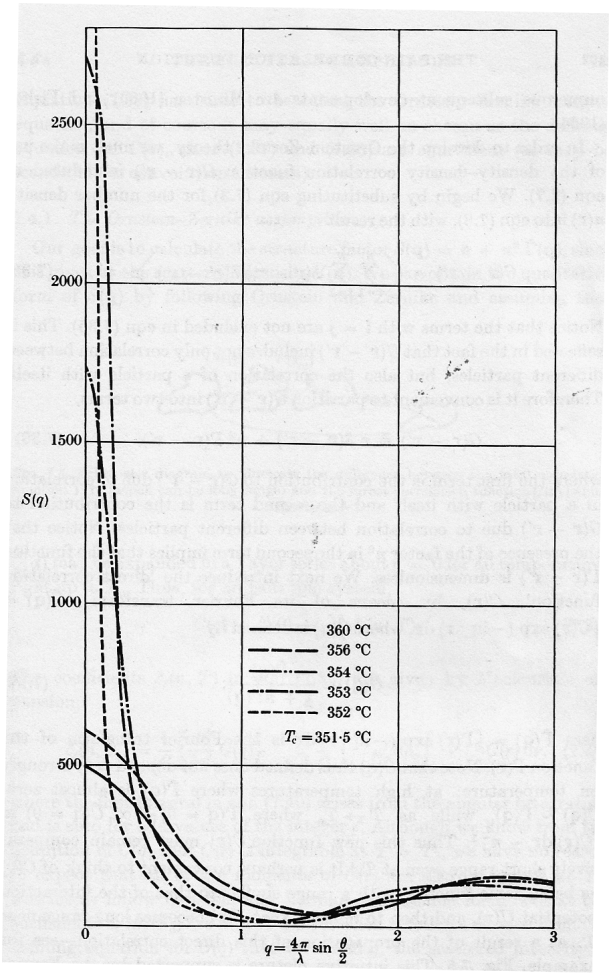

Figure 3.5: q-dependence of the structure factor for several temperatures just above the critical temperature of the system ($T_c = 351.5°C$). Figure from [99].

A NMR cylindrical, borosilicate glass tube containing the sample ($d_{ext} = 3\,\text{mm}$, $d_{int} = 2.4\,\text{mm}$, $h = 30\,\text{mm}$) is inserted in the center of the optical chamber. The focal point is in the center of such optical geometry.
The multi-angle scattering apparatus can simultaneously measure the time correlation functions and the scattering intensity at different values of the scattering vector and it is accurately designed to handle microliter-sized samples.

3.2 Ultraviolet absorption

The absorption of ultraviolet (UV) and visible (Vis) light represents one of the most common techniques used to investigate the structure of biopolymers.

It can be exploited for several purposes, ranging from the determination of the concentration of a given substance to the resolution of complex structural issues.

3.2.1 Basic Theory of UV Absorption

As all the spectroscopic techniques, UV absorption is based on the energy exchange between matter and radiation. When an electromagnetic radiation impinges on a molecule, it causes an oscillation of its electrons. Such electrons may have different energies, depending on how tightly they are linked to the nuclei of the atoms that compose the molecule. Energetic levels are discrete, each one corresponding to a specific electronic state.
If the energy of the incident photon is equal to the difference between two different electronic states, it is probable that the molecule will absorb the photon, passing from an electronic state to another with an higher energy. Typically, the energetic separation between different states is in the range $1 - 10$ eV: electronic transitions, thus, require radiations in the visible or in the UV. UV-VIS spectroscopy (200-700nm) exploits transitions of electrons of the valence shell, which can be either free or involved in a bond.
Electronic transitions in a molecule are always accompanied by vibrational and rotational transitions. Indeed, for each electronic state E_e exist vibrational states with energy E_ν, which are associated to numerous rotational states E_r, both due to the motion of the nuclei of the molecule (Fig. 3.6). Neglecting the coupling between the various contributions, the total energy of the molecule is given by:

$$E = E_e + E_\nu + E_r \tag{3.57}$$

Hence, an electronic transition gives rise to a set of frequency bands:

$$\nu = \nu_e + \nu_\nu + \nu_r \tag{3.58}$$

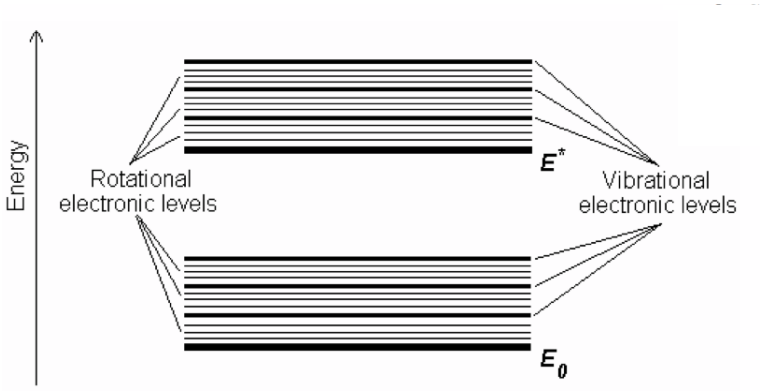

Figure 3.6: Energetic levels: for each electronic state E_e exist vibrational states with energy E_ν which are associated to numerous rotational states E_r.

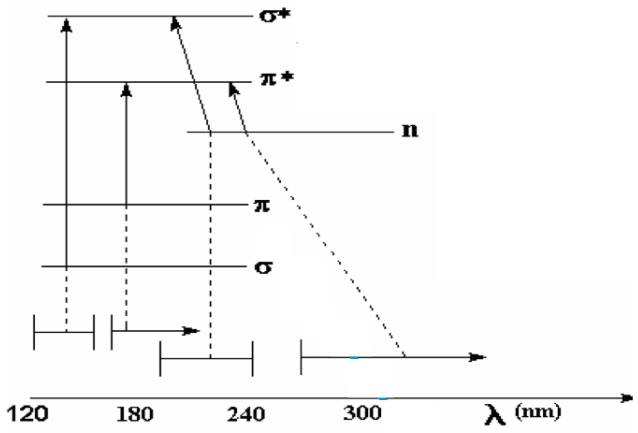

Figure 3.7: Energetic levels corresponding to molecular orbitals with the respective electronic transitions.

Since $\nu_e > \nu_\nu > \nu_r$ ($\triangle E_e \cong 10^3 \triangle E_\nu \cong 10^6 \triangle E_r$), the wavelength λ of the maximum of the band is essentially determined by the frequency ν_e , i.e. by the electronic transition. As the energies of the electronic states are not negligible (30 - 70 Kcal·mol^{-1}), all the electronic transitions start from the fundamental electronic level, which is the only populated at room temperature (as stated by Boltzmann distribution).
Absorption spectra in the UV-VIS region are thus composed by a large number of marked spectral bands, associated to the electronic, vibrational and rotational transitions of the delocalized bonding electrons. Such delocalization can extend to the entire molecule or it can be limited to some specific groups of atoms, separated by saturated bonds which avoid the delocalization. In the former case, the absorption spectrum is unique and hardly understandable through simple rules; in the latter case, it can be considered as the sum of multiple absorptions due to various unsaturated groups, commonly named cromophores.
In order to quantitatively study the absorption by cromophores in the UV-VIS region, one needs to define the energetic levels in complex molecules. For polyatomic molecules, the calculation methods to determine the molecular energetic levels are based on various approximations; the most common one is the molecular orbital method. Such approximation uses linear combinations of independent atomic orbitals (LCAO) that must have similar energy and appropriate symmetry to give maximum interaction (overlap). Combinations with lower energy give rise to bonding orbitals (σ, π) while combinations with higher energy give rise to antibonding orbitals (σ^*, π^*). Moreover, there can be orbitals occupied by an electron pair which do not interact with other orbitals, named non-bonding orbitals (n). The final result gives a complete set of molecular energetic levels, each one characterized by its symmetry properties with respect to the symmetry elements of the molecule. Fig. 3.7 shows energetic levels corresponding to molecular orbitals with the respective electronic transitions. The most studied electronic transitions are those from the Highest Occupied Molecular Orbital (HOMO) to the Lowest

Unoccupied Molecular Orbital (LUMO).

3.2.2 Lambert-Beer law

The experimental law describing absorption phenomena of electromagnetic radiations is commonly known as the Lambert-Beer law.
In order to introduce such law, consider a beam of light with intensity I_0 and wavelength λ that impinges on a sample (usually a solution of absorbing molecules with a concentration of C mol·l^{-1}) for a path length of 1 cm.
The light that is not absorbed by the sample emerges with intensity I. If the sample is orthogonal to the direction of light propagation and slight enough (dl) so that the intensity of the light inside the sample is essentially constant, the fraction of absorbed light (dI/I) is given by:

$$-\frac{dI}{I} = C\epsilon' dl \tag{3.59}$$

where ϵ' is the molar extinction coefficient.
Such quantity is independent from the concentration for a given set of non interacting molecules and it contains the dependence from the wavelength of the absorption spectrum.
By integrating eq. 3.59 on the entire sample:

$$ln\left(\frac{I_0}{I}\right) = C\epsilon' l \tag{3.60}$$

that, by converting the logarithm to the base 10, becomes:

$$A(\lambda) \equiv log\left(\frac{I_0}{I}\right) = C\epsilon(\lambda) l \qquad \epsilon = \epsilon'/2.303 \tag{3.61}$$

The quantity A is called absorbance.
The range in which the relation between absorbance and concentration is linear, i.e. in which the Beer-Lambert law is valid, goes from A $\approx$ 0.1 to A $\approx$ 0.8.

3.2.3 Spectroscopic Analysis of DNA

The concentration of nucleic acids in solution are routinely determined from their strong absorbance at 260 nm. Indeed, amounts of nucleic acids are often given in terms of 'A_{260} units'. The intensity and the right position of this absorbance peak are functions not only of the base compositions but also of the state of the base-pairing interactions present, the salt concentration of the solution and its pH.
The absorption arises almost entirely from complex electronic transitions in the purine and pyrimidine components. Indeed, being aromatic, purine and pyrimidines strongly absorb between 250-300 nm, where they undergo a series of overlapping $n \rightarrow \pi^*$ and $\pi \rightarrow \pi^*$ transitions.

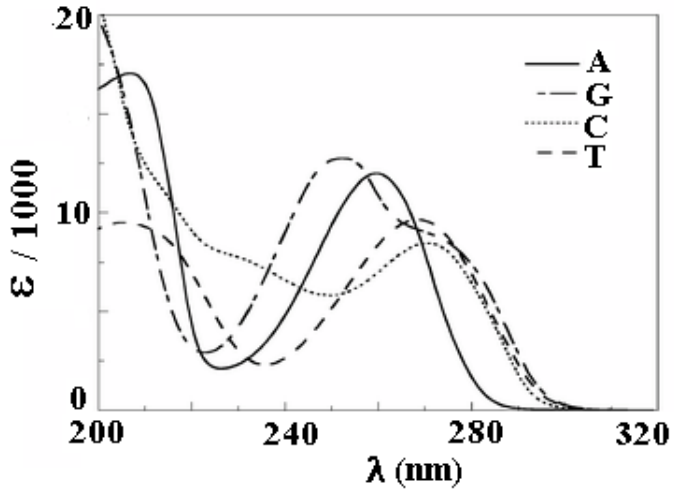

Figure 3.8: Absorbance bands for purines and pyrimidines: when considered together, their spectra merge into a single band with $\lambda_{max} \sim 260$ nm.

Such absorption is relatively strong due to inherently low symmetry among nucleosides[2] (Tab. 3.4) and it gives rise to the four absorbance bands reported in Fig. 3.8. Despite their rather simple appearance, these four bands result from a number of different electronic transitions taking place in the four aromatic rings. As it can be seen, purines have an absorbance maximum slightly below 260 nm, while pyrimidines have a maximum slightly above 260 nm. When considered together, their spectra merge into a single band with $\lambda_{max} \sim 260$ nm so that it is not easy to separate the different contributions. As a consequence, the extinction coefficient of DNA may vary depending on the specific sequence. Anyhow, very long DNA sequences are usually composed by roughly the same amount of each nucleoside, so for each of them, it is possible to use an average molar extinction coefficient of $1.1 \times 10^4 M^{-1} cm^{-1}$. Such assumption is not true for short DNA chains: thus, in this case, the molar extinction coefficient of the sequence must be evaluated by accurately weighting the extinction coefficient of each type of nucleoside for its proper extent in the sequence [100].

Nucleoside	$\epsilon_{(260\,nm)}\,(M^{-1}cm^{-1})$
Adenosine	14,900
Cytidine	9,100
Guanosine	9,000
Thymidine	9,700

Table 3.1: Extinction coefficients relative to each nucleoside.

[2]Nucleosides consist of a nucleobase bound to a deoxyribose sugar via glycosidic linkage.

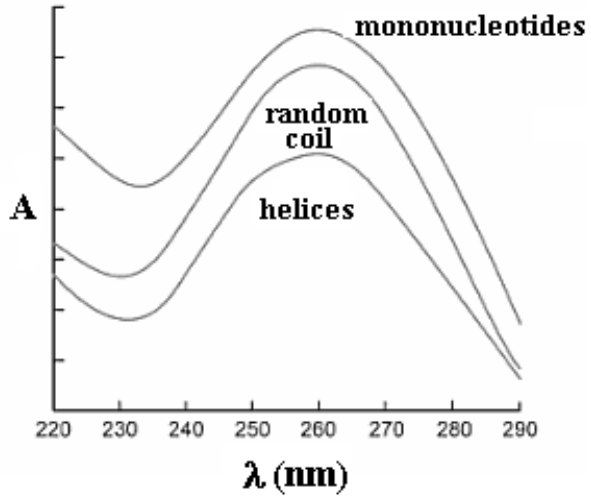

Figure 3.9: Typical example of hypochromicity observed in DNA solutions.

.

DNA hypochromicity

An important point to stress is that, when two ss-DNAs hybridize to form a ds-DNA, their extinction coefficient (and hence their absorbance) decreases due to stacking interactions between neighbouring bases. Indeed, base stacking results in a decrease of ϵ, a situation commonly known as hypochromicity. This arises from dipole-dipole interactions that depend on three-dimensional structure of an oligonucleotide and ranges in magnitude from 1-11% for deoxyribonucleoside phosphates to 30% for most helical polynucleotides. As a result, the absorbance for ss-DNA will be effectively higher than that for ds-DNA at the same concentration (Fig. 3.9).

Experimental determination of DNA purity

In order to determine the purity of DNA oligomers, it is possible to compare the absorbance at 260 nm with the absorbance at the maximum absorbance peaks of proteins, i.e. $\lambda = 280$ nm (which is the wavelength at which the aromatic rings on tryptophan and tyrosine absorb).
As a useful rule, DNA samples are considered pure for $A_{260}/A_{280} > 1.8$. For lower ratios, DNA is badly contaminated with protein and may not behave well in subsequent experiments. Moreover, the ratio A_{260}/A_{230} is used as a secondary measure of nucleic acid purity. Expected A_{260}/A_{230} values are commonly in the range of 2.0 - 2.2. If the ratio is appreciably lower than expected, it may indicate the presence of contaminants which absorb at 230 nm (as, for example, residual phenol from nucleic acid extraction or residual glycogen used for oligo precipitation).

3.2.4 Melting experiments

UV absorption is a convenient way to monitor the melting behaviour of DNA. Indeed, the stability of DNA complexes is often measured by thermal denaturation experiments. Heating a sample always results in a change in absorbance properties, which in turn reflects a conformational variation of the molecules in solution. One may perform thermal denaturation experiments using a UV-visible spectrophotometer by recording absorbance at 260 nm as a function of the temperature. The resulting plot is commonly named *melting curve*. The principle of such an experiment is presented, for instance, in Ref. [101]. A typical UV-absorbance melting curve is shown in Fig. 3.10.
As it can be seen, such curve allows for a quantitative analysis of the melting process since:

- the transition from the associated duplexes to the unfolded single strands takes place in a relatively narrow temperature interval. Since such transition is obtained at moderate temperatures, it is possible to accurately measure a number of experimental points both below and above the observed melting temperature;

- the Y-signal variation is relatively important (both in absolute terms $\triangle A$ and relative terms $\frac{\triangle A}{A}$);

- duplex denaturation results in a hyperchromism of 15% – 20%. This seems modest, but the variations in the absorbance at 260 nm are hardly ever higher.

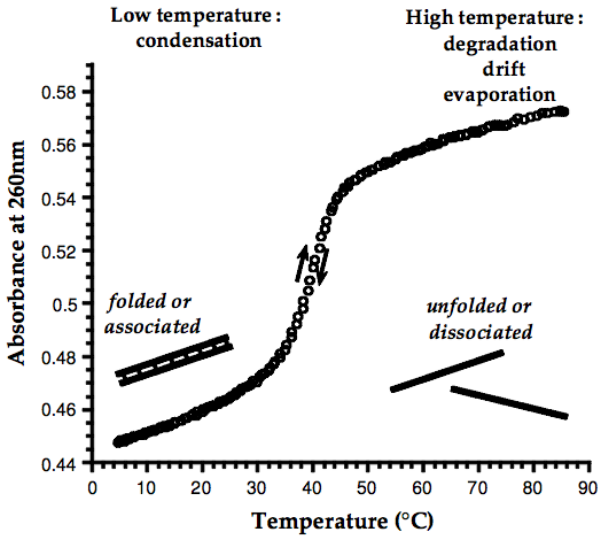

Figure 3.10: A thermal denaturation curve corresponding to a parallel bimolecular duplex at pH 6.5. Figure from [102].

A very popular method to calculate T_m from a melting curve is simply to determine the maximum of the first derivative of the absorbance signal (dA/dT or dA/dT^{-1}).
This approach is simple and user-independend, and several softwares allow for an automatic T_m calculation by using this method, usually claiming a precision of ± 0.1°C.
No subjective baseline choice is required.

3.2.5 UV absorption setup

The instrument used for the melting experiments is a commercial dual-beam spectrophotometer JASCO v-570 UV/VIS/NIR.
Its resolution is of 0.1 nm in the UV-VIS region and 0.5 nm in the NIR region.
The light source consists of a deuterium discharge tube in the UV region (190-350 nm) and of an iodine tungsten lamp in the region between 330-2500 nm.
The detector is composed by a photomultiplier tube and a photoconductive cell, which operate in the UV/VIS and in the NIR range, respectively.
Such apparatus allows to operate in several photometric modes, i.e. absorption, reflection, transmission. In particular, it allows for the collection of the absorption spectrum for $190 < \lambda < 2500$ nm.
The operation diagram of the instrument is rather simple: light from the source is conveyed on a monochromator and subsequently it impinges on a mirror, which divides it into two beams: one incident on the investigated sample and the other incident on a reference sample. Such reference sample represents the background of the measured spectrum and it must be removed from the spectrum to elaborate.
The light, after having crossed the sample, impinges on the detector, where is converted in an electric signal and digitized to be elaborated by a micro-computer. The elaborated signal is then visualized on the output device.
Absorption measurements can be also realized as a function of the temperature. In such case, one can use a thermostated *Peltier* cell (Fig. 3.11).
Such cell uses a thermal panel and exploits the *Peltier effect*[3] to keep the temperature constant within a certain accuracy.
Equipped with a stirrer, the thermal panel allows for a uniform temperature control inside the cell. The temperature setting varies between -10°C and +110°C, with a sensibility of 0.1°C.
All measurements that we will report were taken in a thin quartz cell (optical path length: 1 mm).

[3] *Peltier Effect:* In a bimetallic circuit containing a generator that makes current flows, one observe that one junction heats up and the other one cools down. By inverting the direction of the current, one can observe the opposite phenomenon, which is thus independent from the Joule effect. Indeed, the latter, quadratic in the current, is the same whatever is the current direction. If I is the intensity of the current, the power that needs to be exchanged in a junction to keep the current constant is: $P = \pi_{1,2} I$ where π is the Peltier coefficient related to the metals; it depends on the temperature and on the materials, but it is independent from the geometric characteristics of the contact and from the current intensity. If we invert the current direction the power remains equal in modulus but it changes sign $\pi_{1,2}$ (i.e. Peltier effect is reversible).

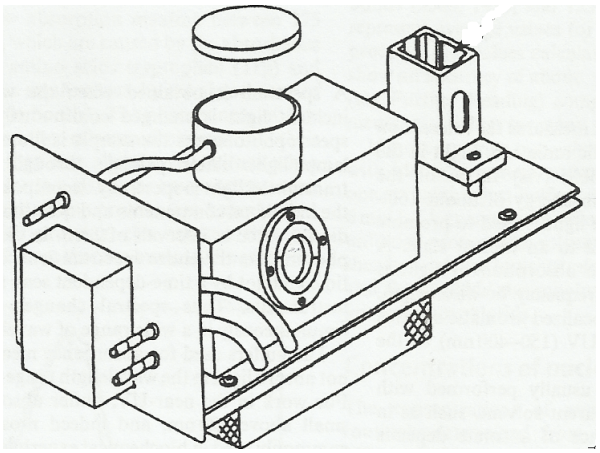

Figure 3.11: Schematic representation of the thermostated Peltier cell used in UV-VIS spectroscopy.

3.3 Atomic Force Microscopy

Atomic Force Microscopy (AFM) is a powerful technique that allow us to visualize and measure surface structures with exceptional resolution and accuracy. For instance, an Atomic Force Microscope allows for the visualization of the arrangement of individual atoms or the structure of individual molecules in a sample.
AFM is completely different from other microscopies, since it does not create an image by focussing light or electrons onto a surface, as in other optical or electron microscopies. Indeed, an Atomic Force Microscope scan the surface of the sample using a sharp probe, thus building up a map of the height of the surface. This is different from any other imaging microscope, which only measures a two-dimensional projection of the sample's surface. In the following we only provide a brief introduction to this technique, referring to Ref. [103] for further insights.

3.3.1 Basic Theory of AFM

AFM is the most commonly used kind of the Scanning Probe Microscopy (SPM) classes of techniques. The growth of such techniques started with the development of the scanning tunneling microscope in 1981 by researchers at IBM [104]. The ability of the STM to visualize the surface of the investigated samples with atomic resolution earned the inventors the Nobel Prize in 1986.
However, a general limitation of the STM is that it could only be used for conductive or semiconductive specimens.
In order to exploit this kind of microscopy to study also insulators, the Atomic Force Microscope was developed as a collaboration between IBM and Stanford University in 1986 [105].
Typically, an AFM measurement is performed by scanning a sharp tip on the end

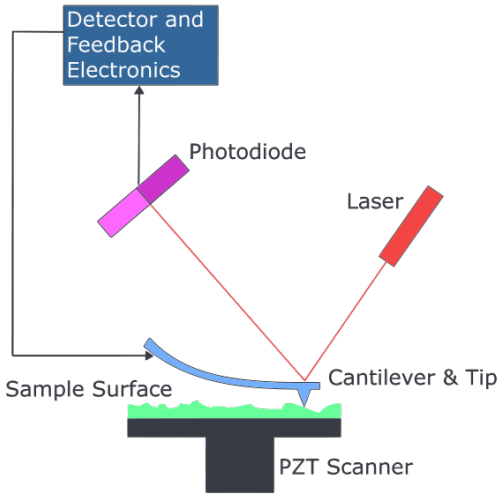

Figure 3.12: Schematic representation of the major components of an Atomic Force Microscope.

of a flexible cantilever across a sample surface, while maintaining a small, constant force. The tips generally have a radius of curvature of 5-10 nm, although this can vary depending on the tip type.
The scanning motion is controlled by a piezoelectric tube scanner which scans the sharp metallic probe over the surface in a raster pattern (Fig. 3.12).
When the tip is brought into proximity of the sample surface, forces between the tip and the sample (e.g. van der Waals, capillary, electrostatic or magnetic) lead to a deflection of the cantilever according to Hooke's law. The tip-sample interaction is monitored by reflecting a laser spot from the top of the cantilever onto a split-photodiode detector.

Topographic Modes

The basis of AFM as a microscopic technique is that it measures the topography of the investigated sample: as already mentioned, in fact, the resulting datasets are not conventional images, as those obtained by optical microscopy, but a map of height measurements. These are later transformed into more naturalistic images using light shading, perspective, etc. to help in depicting the shape of the samples.
In order to make such height measurements, a variety of modes have been developed. The two most commonly used modes of operation are contact mode AFM and Tapping Mode TM-AFM, which can be performed in air or in liquid environments.
In contact mode AFM, a constant deflection of the cantilever is maintained by a feedback mechanism that moves the piezoelectric scanner vertically at each lateral data point to generate the topographic image.
By keeping the deflection constant during scanning, a steady vertical force is maintained between the probe and the sample. Applied forces during imaging typically range

between 0.1 and 100 nN. Even though contact mode is currently exploited in a wide range of applications, it is not suited for soft samples. Indeed, close to the surface of the sample, attractive forces can be so strong to cause the tip to adhere to the surface. On the contrary, TM-AFM consists of oscillating the cantilever at its resonance frequency (typically around 300 kHz) and scanning over the surface with a constant, damped amplitude.
The feedback loop uses the piezoelectric actuator to control the height of the cantilever above the sample, continuously adjusting the height to maintain constant the oscillation amplitude as the cantilever is scanned over the sample. The topographic profile is thus generated by imaging the force of the intermittent contacts of the tip with the sample. The advantage of TM-AFM is that it operates with lower vertical forces than the contact mode AFM, eliminating lateral, shear forces that can damage samples. Thus, TM-AFM is currently the favorite technique for imaging soft, fragile or adhesive samples

Non-Topographic Modes

All the Scanning Probe Microscopies can be used to obtain more than just topographic informations. In this respect, a large variety of non-topographic modes in AFM imaging have been developed, each one useful to probe a particular property of the sample (different from its topography).
Among this non-topographic modes, a remarkable role is played by "phase imaging". Such approach in AFM refers to the possibility of recording the phase shift signal in intermittent-contact AFM: such phase signal is particularly sensible to variations in composition, adhesion, friction and viscoelasticity and it also reflects topometric differences of the investigated samples.
This is because the phase provides an effective indication of the energy dissipation involved in the contact between the probe and the sample which depends on a number of factors, including adhesion and contact area.
Despite various complications involved in its proper interpretation, phase imaging is one of the most commonly used techniques for the mechanical characterization of sample surfaces, being easy to obtain and not requiring post-processing of the data.

3.3.2 AFM on nucleic acids

AFM can be exploited to generate highly accurate images of nucleic acids under physiological conditions with nanometric resolution.
Hence, AFM can be considered a potent analytical technique to study DNA [106].
Such methodology has been used to characterize nucleic acid structures such as supercoiled, kinked and looped DNA as well as DNA-protein complexes [107, 108, 109].
In order to be properly resolved by AFM, samples must necessarily be immobilized onto smooth stationary substrates. For this reason, some kind of surface modification may be required to immobilize biomaterials biological materials for AFM studies.

In the case of DNA, its negatively charged backbone can be utilized for immobilization onto charged substrates by means of electrostatic interactions: muscovite mica is the most widely used substrate for this purpose.
Divalent cations are typically used as a sort of bridge for immobilizing charged DNA molecules onto mica substrates [110]. The cations must be water soluble and they must bind tightly to both the backbone of the DNA and the mica surface in order to bear the force applied by the AFM probe during imaging. Typically, Nickel (Ni^{2+}) and Magnesium (Mg^{2+}) are utilized for this purpose since since they meet these criteria.

3.3.3 AFM setup

Atomic force microscopy (AFM) was performed with a Dimension Icon (Bruker AXS) instrument. AFM images were acquired in air, at room temperature and under ambient conditions, by employing two oscillating imaging technique, Tapping mode and Scan AsystTM mode.
The Scan AsystTM mode is a Bruker-proprietary imaging mode which continuously monitors the quality of the image and self-optimizes the acquisition parameters by using an algorithm operating in Peak Force TappingTM. In this algorithm is the peak force which is used by the feedback as its control signal. By applying a precisely controlled force response curve at every pixel, Peak Force TappingTM permits the use of ultra-low imaging forces than Tapping mode, protecting soft samples from damage without compromising the image resolution.
In Tapping mode, we employed high resolution RTES (Rotated Tapping Etched Silicon) probes (VEECO Probes, US).
These probes have a sharp tip (radius of curvature specified by the manufacturer R $\sim$ 2 nm) which is asymmetrically connected to the rectangular cantilever (length 125 m, nominal resonant frequency 300 kHz, nominal spring constant 40 N/m).
Such asymmetry (the front angle is 15° and the back one is 25°), that justifies the adjective "rotated" in the probe name, partially compensates for the cantilever inclination angle, providing a more symmetric representation of features over 200 nm.
For the images in ScanAsystTM mode, we employed dedicated probes characterized by an ultra-sharp silicon tip (nominal radius of curvature 2 nm) that, analogously to the RTESP probes, are mounted asymmetrically on a silicon nitride cantilever.
In this case the cantilever is triangular, with a very low spring constant (0.4 N/m) and a nominal resonant frequency of 300 kHz, allowing for the required high level force control on soft samples in air.
Images have been analyzed using the Gwyddion 2.28 free soft- ware (http://gwyddion.net/) and are presented as raw data, except for flattening.

3.4 Gel electrophoresis

Gel electrophoresis is a technique widely used in biology for the separation of biological macromolecules (e.g. nucleic acids and proteins) based on their size and charge. For what concerns nucleic acids, the basic principle is rather simple: DNA or RNA molecules are separated by applying an electric field that cause the motion of the negatively charged molecules through the matrix of a gel.
Indeed, following a phenomenon commonly named as sieving, the short molecules move quickly in the gel (since they can easily migrate through the pores of the matrix) and they thus migrate farther than the longer ones.
In most cases, the gel is a crosslinked polymer whose composition and porosity is chosen on the basis of the specific weight and composition of the target to be analyzed.

3.4.1 Types of gels

Commonly, two types of gel are most typically used to run electrophoretic experiments, i.e. agarose and polyacrylamide gels. In both of them, the size of the pores of the gel matrix depends on the specific concentration of the element used to create the gel. Clearly, each kind of gel is appropriate for specific species and sizes of analytes.

Agarose gel

An agarose is a polysaccharide polymer material, able to form a gel matrix without the need of additional cross-linkers.
Agarose gels are three-dimensional matrices composed by helical agarose molecules aggregated into supercoiled bundles which present structural pores of non-uniform but rather large size through which biological macromolecules can pass.
Agarose gel electrophoresis is commonly used for the separation of DNA fragments ranging from 50 bp to several megabases (even if the largest ones need a specialized apparatus).
As the DNA migrates through the gel, the different fragments form bands: each band is composed by several identical copies of a specific-size sequence of DNA.
The distance between DNA bands of different lengths is affected by the percentage of agarose in the gel, with higher percentages requiring longer run times.
Most agarose gels contains a percentage of agarose between 0.7% (high resolution for large DNA fragments, i.e. 5–10 kb) and 2% (high resolution for small DNA fragments, i.e. 0.2–1 kb).

Polyacrylamide gel

Unlike agarose gels, polyacrylamide gels are usually obtained by mixing different concentrations of acrylamide with a crosslinker, thus producing different sized mesh networks of polyacrylamide.

In this kind of gel matrix, samples usually run in denaturing conditions.
Advantageously, the size of the pores can be tuned at will by controlling the concentrations of acrylamide and bis-acrylamide powder used in creating a gel.
In contrast to agarose gels, polyacrylamide ones usually present a uniform pore sizes which make them appealing for the purification of DNA oligomers.
Indeed, such gels are particularly suited for oligomer purification since traditional DNA sequencing techniques such as Maxam-Gilbert or Sanger methods use polyacrylamide gels to separate DNA fragments differing only by a single base-pair in length.

Part III

Results and Discussion

Chapter 4

Design and preliminary investigation of DNA nanostars

"Putting what you want
where you want it in three dimensions,
when you want it there"

Nadrian Seeman

As already discussed in the second chapter, it is possible to exploit the selectivity of DNA interactions to design self-assembling structures with controlled mutual interactions.
In this study, following the lines set by structural DNA nanotechnology, we have introduced a challenging twist: the realization of DNA nanoconstructs as man-designed particles to experimentally explore unconventional phase behaviours conceived so far only in charta and in silico [14, 15]. Specifically, we took advantage of the recently built knowledge on programmable DNA self-assembly, to design mutual interacting particles with controlled valence, to experimentally investigate the limited-valence issue described in the first chapter.
In this respect, in the first section of this chapter, we introduce the protagonists of our investigation: self-assembling DNA nanostars with four and three sticky terminals (having valence four and three respectively), showing how they can be design to mimic the collective behaviour of limited-valence particles. As explained in the introduction, being the work in collaboration with the group of Prof. Bellini, who was already working on DNA tetramers in Milan, here we mainly focus on DNA nanostars with valence three, i.e. DNA trimers. In particular, in the second section, we describe the experimental preparation of DNA nanostar samples, describing the developed procedures to obtain the maximum yield of well formed structures. The last part of this chapter is instead dedicated to the preliminary characterization of our systems. Indeed, via the combination of different experimental methods (gel electrophoresis, UV absorption, AFM) it was possible to check whether the protocol of structure formation was effective as well as to monitor the self-assembling process.

4.1 Structure design

To generate DNA nanostars with specific valence, we dissolved equimolar quantities of ss-DNA 49-mers, designed to self-assemble around $T_{sa} \approx 65°C$ (in 50 mM NaCl) into star-shaped particles with f double-stranded arms of 20 bases each (Fig. 4.1).

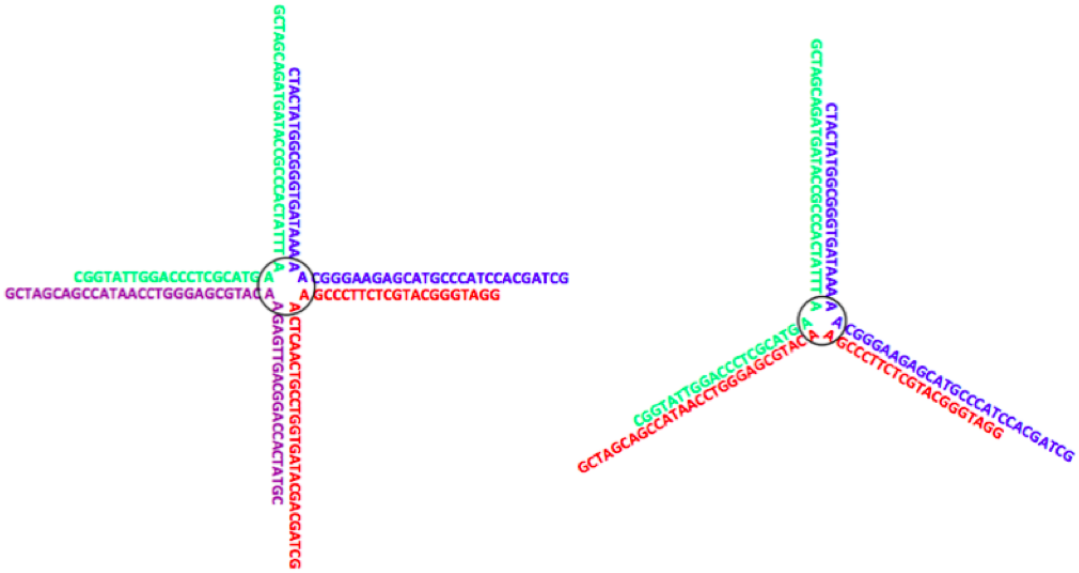

Figure 4.1: Schematic representation of the pairing of the DNA sequences in (a) $f = 4$ and (b) $f = 3$ nanostars.

To enable angular flexibility between different arms, bases with no complementary partner were inserted between the arm-forming sequences. To control the inter-particle binding, each arm terminates with an identical ss overhang six bases long with sequence CGATCG. This self-complementary sequence allows for mutual association via Watson-Crick pairing of the overhangs of close-by structures.
The use of the same overhang sequence for $f = 3$ and $f = 4$ provides an identical interaction strength in structures of different f, enabling us to ascribe eventual differences in the phase behaviour of the systems to the different valence.
Since the binding between sticky overhangs is stronger than all other inter-particle interactions (excluded volume, van der Waals, electrostatic), DNA nanostars provide an optimal model for highlighting the role of the valence. Similar DNA nanostars were studied by Luo and colleagues [78] to investigate their gelation in the presence of enzymatic catalysis. Here, we operate instead in the absence of any enzymes to benefit of the reversibility of the DNA interaction and systematically investigate the equilibrium phase behaviour.
As mentioned, star-shaped DNA nanostructures are formed from the controlled self-assembly of complementary oligomers. Each nanostar is thus composed by a number of sequences which is equal to the number f of double-helical arms.

In particular, $f = 4$ nanostars are self-assembled starting from the following four 49mer sequences:

1. 5'-CTACTATGGCGGGTGATAAAAACGGGAAGAGCATGCCCATCCACGATCG-3'
2. 5'-GGATGGGCATGCTCTTCCCGAACTCAACTGCCTGGTGATACGACGATCG-3'
3. 5'-CGTATCACCAGGCAGTTGAGAACATGCGAGGGTCCAATACCGACGATCG-3'
4. 5'-CGGTATTGGACCCTCGCATGAATTTATCACCCGCCATAGTAGACGATCG-3'

The three sequences forming $f = 3$ nanoconstructs are instead:

1. 5'-CTACTATGGCGGGTGATAAAAACGGGAAGAGCATGCCCATCCACGATCG-3'
2. 5'-GGATGGGCATGCTCTTCCCGAACTCAACTGCCTGGTGATACGACGATCG-3'
3. 5'-CGTATCACCAGGCAGTTGAGAATTTATCACCCGCCATAGTAGACGATCG -3'

Each strand is designed to bind to two other strands with two 20 bases long segments, leading to the formation of the double helical arms of the structure.
As already mentioned, two A bases without complementarity are placed in between the arm-forming segments to release angular constraints between the arms arising from the crowding of paired strands at the center of the constructs, thus creating a branch point. With such choice, arms are allowed some flexibility in their mutual angles. For the same reason, another A base with no complementary partner is added before the six bases overhangs. In this way each overhang is allowed to rotate. This minimizes the constraints on the mutual orientation of two bound constructs, since each can freely rotate around the axis connecting the centers of the two structures.
Despite the flexibility of the structures, electric charges on the phosphate groups tend to keep the construct arms away from each other, favouring a nearly 3D tetrameric shape for the $f = 4$ constructs and an open flat structure for the $f = 3$ constructs.

4.1.1 Temperature behaviour

It is worth to note that, being the structure of our DNA nanostars characterized by two different length scales (i.e. the length of the double helical arm and the length of the sticky terminal), the system exhibits a very-well defined temperature behaviour.
Indeed, the melting temperature of a DNA chain crucially depends on its length, i.e. on the number of nucleobases forming the strand. In general, the longer the sequence, the higher the melting temperature will be. Therefore, since the length of the overhangs - 6 bases - is much smaller than the length of the arms - 20 bases - the binding between overhangs of different nanostars should start becoming relevant at $T_b \approx 42°C \ll T_{sa}$. Hence, a large temperature interval $T_b < T < T_{sa}$ is found in which in which nanostars with desired valence are well-formed but weakly interacting.
As a consequence, upon decreasing the temperature from high values, the system changes from a mixture of single strands at $T > T_{sa}$, to a solution of independent

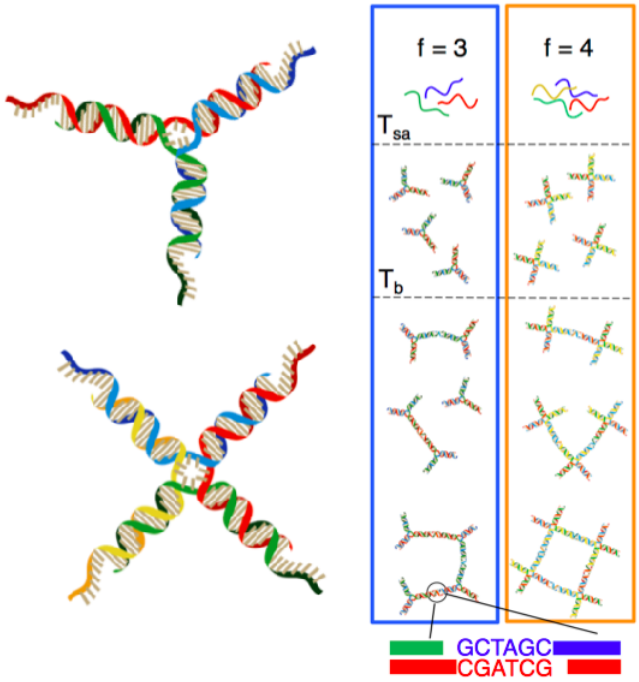

Figure 4.2: Right: Representation of $f = 3$ (top) and $f = 4$ (bottom) nanostars. Left: Schematic of the temperature behaviour of the systems.

constructs in the interval $T_b < T < T_{sa}$ to a state in which the nanostars are bound in a three-dimensional network when $T < T_b$ (Fig. 4.2). Indeed, for $T < T_b$, the number of bonded overhangs progressively increases, giving rise to a tridimensional network of bonded nanostars.

4.1.2 Estimate of $\triangle G$ and T_m for nanostar overhangs

By using the NN model (Sec. 2.1.2), one can provide an estimate of the free energies and the melting temperatures for the sticky terminals from database values. Specifically, by adopting the values for ΔH_Q and ΔS_Q listed in Ref. [62], it is possible to determine the enthalpy and entropy associated to the hybridization of the sticky ends, thus providing the interaction energy between the DNA structures.
Specifically, by summing up all quadruplet contributions one finds:

$$\Delta H(CGATCG) = \sum_{N-1} \Delta H_Q + \Delta H_{INIT} = \tag{4.1}$$

$$= (-10.6 - 8.2 - 7.2 - 8.2 - 10.6 + 0.2)\, kcal/mol = -44.6\, kcal/mol$$

and

$$\Delta S(CGATCG) = \sum_{N-1} \Delta S_Q + \Delta S_{INIT} + \Delta S_{SALT} = \tag{4.2}$$

$$= (-27.2-22.2-20.4-22.2-27.2-5.7-6.7)\, cal/molK = -132\, cal/molK$$

The term ΔS_{SALT} represents a correction due to the fact that tabulated values refer to 1 M NaCl while our experiments are mostly performed at a total ionic strength of around 50 mM [62].
Moreover, the hybridization energy and enthalpy estimates enable us to predict the melting temperature T_m of the duplexes. Indeed, the melting temperature of the sticky ends is a crucial parameter in designing the structures and in determining the proper length of the overhang sequences. When dealing with self-complementary sequences, as the 6-mer forming the overhangs, T_m can be simply expressed as:

$$\frac{1}{T_m} = \frac{R}{\triangle H} ln(f[c]) + \frac{\Delta S}{\triangle H} \tag{4.3}$$

where $[c]$ is the molar concentration of the DNA nanostars.
As we will see in the following chapter, the critical concentration for our $f = 3$ nanostars will be $c_{DNA} = 4.5\, mg/ml$: for such value, the calculated melting temperature in 50mM NaCl results equal to $T_m = 26.7$°C.

4.2 Sample preparation

In order to realize DNA nanoconstructs with specific valence, the first step was to define a systematic and reproducible protocol of sample preparation. Given the necessity of creating only nanostars with the correct valence, sample preparation resulted highly tricky. After numerous trials, it was possible to develop and progressively optimize a standard procedure which guarantees the correct formation of the desired structures.
The developed protocol for structure formation consists of 4 steps: purchase, reconstruction, deposit and sealing, annealing.

1. Purchase:

DNA sequences were purchased from two different companies, PRIMM and IDT, with different degrees of purification. Both companies provided us samples of dehydrated synthetic oligomers.
Purchasing DNA oligomers from different companies was useful to create a robust protocol of sample preparation, independent from the way in which the synthetic DNA was delivered. Moreover, such choice allowed a direct comparison between the yields of well-formed structures achieved by following slightly different protocols of sample preparation (due to the differences in DNA oligo delivery) and it provided a quantitative evaluation of the reproducibility of our measurements.
One crucial point to achieve a significant yield of DNA nanostars with the correct valence was the definition of the proper degree of purification suited for our synthetic DNA sequences. Indeed, during DNA synthesis, each nucleotide is sequentially attached to the growing chain of synthetic nucleobases: thus, in each attaching cycle, a small

percentage of the oligo chains may not be extended. As a consequence, the resulting final product is always a mixture of full length sequences and truncated ones. Therefore, after the chemical synthesis, some truncation products and small organic impurities typically contaminate the final oligomers. In order to avoid it, companies provide different methods of oligo purification which result in different degrees of purity of the final products. In general, higher degrees of purification guarantee a much cleaner sample, in term of length polidispersity and synthesis impurities, but this reflects in a much lower oligo yield. Typically, companies provide three options for oligo purification:

- Polyacrylamide Gel Electrophoresis (PAGE): This method of purification uses high percentage acrylamide gels to separate and elute the full-length product from all shorter species with great efficiency. PAGE is the most efficient means of purification for oligonucleotides that are unmodified. PAGE purification does result in an unavoidable loss of mass because it is physically impossible to recover every bit of full-length product from a gel slice. However, the loss of mass is typically an acceptable trade for the increase in purity. This kind of purification selectively separates oligonucleotides as a function of their length. The accuracy of the procedure ensures a very high purity level of product (up to 95-99% of full-length product) and control quality measurements can be done by using ESI (a particular kind of mass spectrometry). This degree of purification is highly recommended for oligomers longer than 60 bases.

- High Performance Liquid Chromatography (HPLC): HPLC is a form of column chromatography that utilizes a column to hold a stationary phase while the sample is applied within a mobile phase. The analyte's motion through the column is slowed by specific chemical or physical interactions with the stationary phase as it passes through the length of the column. The amount of retardation depends on the nature of the analyte, stationary phase and mobile phase composition and, thus, retention time is unique for each analyte. This kind of purification helps to remove truncated synthesis products and to enrich purity. Such degree of purification is recommended for oligos greater than 40 bases in length and for many modified oligos. Again, there will be an unavoidable loss of mass due to purification but this will be offset by the gain in purity. HPLC purification typically results in approximately 85% purity. Purity guarantees are issued on sequences up to 60 bases as long as they are not heavily modified or do not contain significant secondary structures. In general, HPLC tends to produce oligonucleotides that are slightly less pure than PAGE, but typically, with a higher guaranteed yield.

- STANDARD DESALTING: This procedure represents the basic oligo purification: it only removes residual by-products from the synthesis, cleavage and deprotection procedures. For many applications, standard desalting is acceptable for oligos less than or equal to 35 bases in length since the overwhelming abundance of full-length oligo outweighs any contributions from shorter products.

Finding the purification suited for our specific aims was a difficult task. Basically, we tried to find a compromise between the need to work with very high DNA concentrations (which in turn requires a very high oligo yield) and the necessity to minimize the number of ill-formed structures (which can achieved by having more than 95% of full-length oligos). After numerous experimental trials, PAGE purification, providing the higher percentage of full length product, emerged as the best solution to reduce the amount of ill-formed structures.

2. DNA Reconstruction

Since both companies provided us dehydrated DNA oligomers, the second step of our protocol for sample preparation consisted of DNA dissolution in appropriate quantities of NaCl electrolyte solutions with controlled ionic strength. In particular, experiments were performed at different salt concentrations, ranging from 50mM to 500 mM NaCl. NaCl solutions were prepared using degassed ultra-pure deionized water with an electroresistance above 18 $m\Omega\, cm^{-1}$ obtained by a Milli-Q system present in our chemical laboratory.
$f = 3$ nanostars were formed by mixing equimolar quantities of the three strands involved in the structures. To minimize the amount of ill formed nanostars we took particular care to ensure that the f distinct oligomers were present in equal stoichiometric amount in all samples. In the case of PRIMM oligomers, the company pre-mixed the f sequences, preparing a single starting solution by mixing the sequences in equal ratios. The obtained homogeneous mother solution was then divided into several aliquots, which were then dried for subsequent use and delivered. IDT, on the other hand, did not pre-mix the f sequences: we thus received f different aliquots each one containing a specified amount of only one of the three sequences in a dehydrated form. In this case, after redissolving the aliquots, we could prepare the solutions of nanostars by directly mixing equimolar quantities of the three sequences.

3. Deposit and Sealing

DNA samples were inserted into cylindrical, borosilicate glass tubes, commonly used in NMR preparation (inner diameter d = 2.4 mm). Such tubes are equipped with little home-made teflon caps, endowed with a very narrow hole in their center which acts like a guide for a syringe needle. This expedient helped in achieving a very accurate preparation of the samples, allowing the correct deposit of all the DNA solutions on the bottom of the cuvette, without the risk of losing part of them on the cuvette walls. All samples were topped with about 30 µl of silicon oil in order to avoid evaporation and condensation on the tube walls and flame sealed using a butane lamp.

5. Annealing

Solutions were inserted in a oven, brought to 90°C for 20 minutes (thermal denaturation) and slowly cooled to room temperature in approximately 8 hours.

4.3 Preliminary Investigation

Once defined the procedure for structure formation, the following step was to check whether the self-assembling nanostars behave as expected. To this aim, we carried out a preliminary investigation on our DNA samples, with the specific aim of testing the validity of the sample preparation procedure. Specifically, in collaboration with the Biology Department of the University of Milan, it was possible to run gel electrophoresis experiments to evaluate the percentage of well formed nanostars. Moreover, using UV absorption measurements, it was possible to monitor the two-step melting profile of our $f = 3$ DNA nanostars, thus confirming both the formation of the structures as well as the binding of different nanostars via Watson-Crick base pairing of the sticky terminals. Interestingly, using this technique, was also possible to investigate how the melting process was affected by the ionic strength of the medium. Eventually, AFM measurements allowed for the visualization with nanometric resolution of both isolated and bonded DNA nanostars.

4.3.1 Gel electrophoresis

In order to verify the formation of the desired structures, $f = 4$ and $f = 3$ nanostars were dissolved in NaCl electrolyte solutions (considering that each phosphate dissociates one cation, the ionic strength of the solution was chosen so that the resulting counterions concentration of the sample is approximately 48 mM NaCl), diluted in TBE buffer to a concentration of $\approx$ 100 ng/ml (maintaining the same ionic strength), marked with ethidium bromide and inspected via gel electrophoresis (4.3). Electrophoretic runs were performed under non-denaturing conditions in 3% agarose gel at temperatures between $33°C$ and $35°C$ to minimize interactions between the sticky-ends. The temperature could not be increased further because the agarose gel melts at $40°C$.

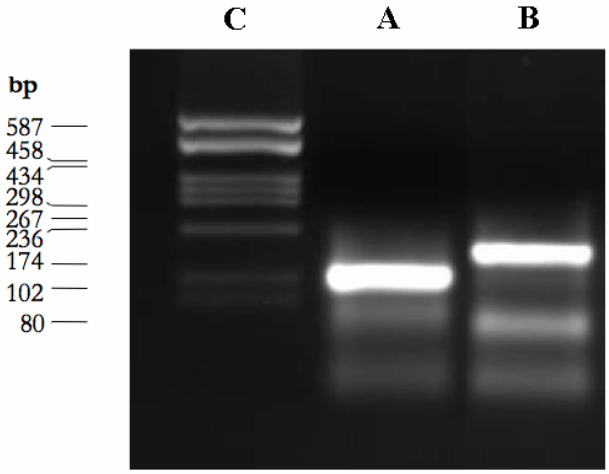

Figure 4.3: Gel electrophoresis of $f = 3$ nanostars after running for 20 minutes in agarose gel.

In lane C a ds-DNA size marker (pUC8 HaeIII fragment lengths varying from 587 to 80 bp) was used to approximately gauge the position of the DNA structures. In lane A and B a solution of $f = 3$ nanostars and of $f = 4$ nanostars were respectively loaded. From the analysis, performed by the group of Prof. Bellini, emerged that fully formed structures involve about 93% of the total DNA for both $f = 3$ and $f = 4$ nanostars.

4.3.2 UV melting profiles

As explained in Sec. 4.1.1, our DNA nanostars are designed to undergo a well-defined two-step self-assembling behaviour. In particular, the hybridization process leading to the formation of the nanostars should take place at temperature values significantly higher than those at which the mutual interactions between overhangs start to occur. In order to verify such presumed behaviour, we performed UV absorption measurements to experimentally evaluate the melting temperatures of our system, aiming at confirming the presence of a temperature gap in which nanostars are formed but weakly interacting. For these measurements, DNA solutions of $f = 3$ nanostars were prepared at a very low concentrations (0,075 mg/ml) in order to operate in the range in which the relation between absorbance and concentration is linear, i.e. in which the Beer-Lambert law is valid (for $0.1 < A < 0.8$). For the same reason, we also decide to use a spectrophotometric cuvette with a very short optical path (1 mm). To properly monitor the structure formation, samples were annealed directly in the spectrophotometric cuvette. For each investigated sample, we equilibrated the DNA solution at 90°C for 20 minutes with the specific aim of thermally denaturing any possible mismatched ds-DNA randomly formed before the annealing, obtaining an homogeneous solution of ss-DNA. Fig. 4.4 shows the absorption spectrum acquired after a waiting time of 20 min at 90°C on a solution of $f = 3$ nanostars (50 mM NaCl).

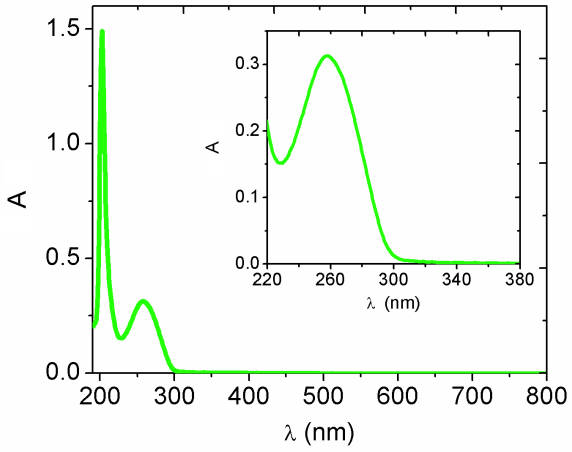

Figure 4.4: Absorption spectrum at 90°C on a solution of $f = 3$ nanostars (50 mM NaCl).

The reported spectrum is the typical absorption spectrum for ss-DNA: as expected purine and pyrimidines bases absorb strongly only in the near ultraviolet region. Specifically, saving the peak at approximately 200 nm, where nearly everything absorbs, one can clearly observe the typical absorbance band of DNA between 240 and 380 nm, with the expected peak at $\lambda \sim 260$ nm (inset of Fig. 4.4).
As discussed in Sec. 3.2.3, the position of such peak depends on several factors (including the base composition of the sequence) and can be thus slightly shifted from the aforementioned value. Indeed, in our case, the wavelength corresponding to the maximum absorbance is $\lambda = 258.5$ nm.
Once obtained the absorbance spectrum at 90°C, where the system is entirely composed by single strands in solution, the next step was to acquire the same spectrum at a lower temperature (e.g. $T = 5$°C), where most of the DNA sample is supposed to be in a double helical conformation. Indeed, as previously shown in Fig. 3.9, we expected a change in the absorption spectrum due to hypochromicity.
Fig. 4.5 shows the result of the comparison between the two spectra acquired at 90°C and 5°C. Interestingly, a marked hyperchromism of around 20% results from the comparative analysis of the two spectra, thus allowing for the investigation of the melting processes.
After this important confirmation, it was possible to perform a melting experiment by monitoring the absorbance at 258.5 nm as a function of the temperature. Specifically, after equilibrating the sample at 90° for 20 minutes, we slowly lower the temperature to 5°C, with a cooling rate of 0.32 °C/min (since, below room temperature, condensation may occur we gently blew a stream of liquid nitrogen through the sample compartment). The choise of such a low temperature gradient is due to several reasons. Firstly, thermal equilibrium must be reached between the Peltier temperature controller and the

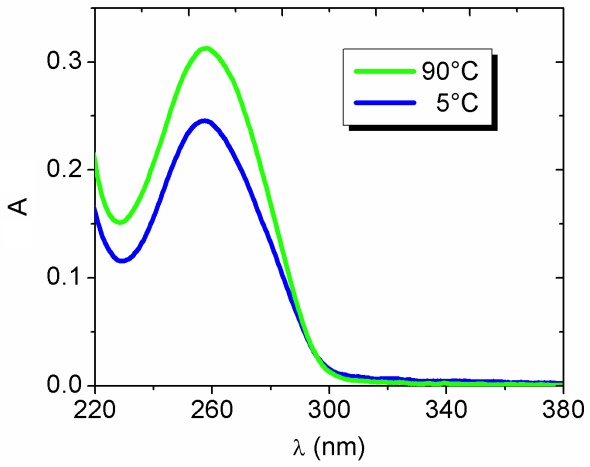

Figure 4.5: Comparison between spectra at 90°C and 5°C for $f = 3$ nanostars (50mM NaCl).

solution in the cuvette. In fact, despite many experimental settings simply assume that the Peltier controller temperature is equivalent to the temperature of the sample, this assumption is often inaccurate. Actually, the temperature of the sample may differ by as much as 6–7°C (especially at very high or very low temperatures). Transmission of heat to the cuvette (to reach thermal equilibrium) is also not instantaneous. With temperature gradients above 0.5°C/min, the sample temperature may thus not reach equilibrium. Moreover, not all association processes are as fast as Watson-Crick duplex formation . Rapid decrease in temperature may thus lead to experimental curves that do not correspond to the equilibrium curves. This may in turn lead to an inaccurate T_m determination (overestimated by the heating profile, underestimated by the cooling profile). For such reasons, following [102], we decided to work with temperature gradients in the 0.1–0.4°C/min range (i.e. 6–24°C/hour).
Fig. 4.6 shows the normalized cooling profile (in the 70°-5°C temperature range) for a solution of $f = 3$ nanostars (NaCl 50 mM). The molar concentration of NaCl was chosen so that the melting temperature of the two processes (i.e. nanostars formation and overhang hybridization) should fall in the investigate temperature window. Indeed, numerical prediction from http://www.nupack.org, suggested that, at the investigated DNA concentration, the melting temperature for the structure formation should be $T_m \sim 64$°C, while the one for the sticky end hybridization should be approximately $T_m \sim 11$°C. As it can be observed, the temperature behaviour of the system follows our expectations: starting from high temperatures, the melting curve clearly shows two distinct decays. By determining the maximum of the first derivative of the absorbance signal (Fig. 4.7), one can easily observe that the experimental $T_m = 61.0$°C is in a good agreement with the aforementioned numerical predictions. The first melting can

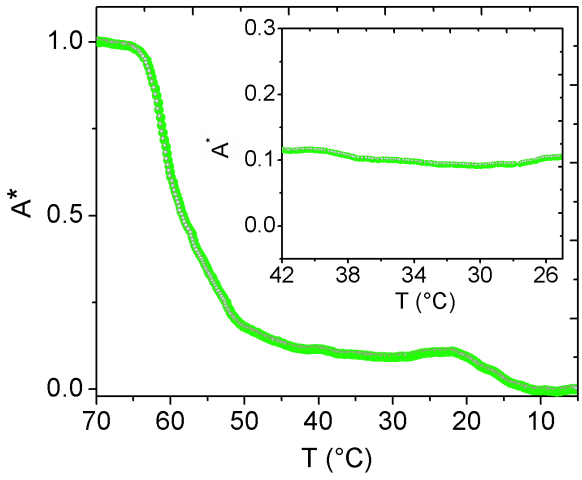

Figure 4.6: Cooling profile for a solution of $f = 3$ nanostars (NaCl 50 mM). The inset shows the T-interval in which the absorbance remains nearly constant.

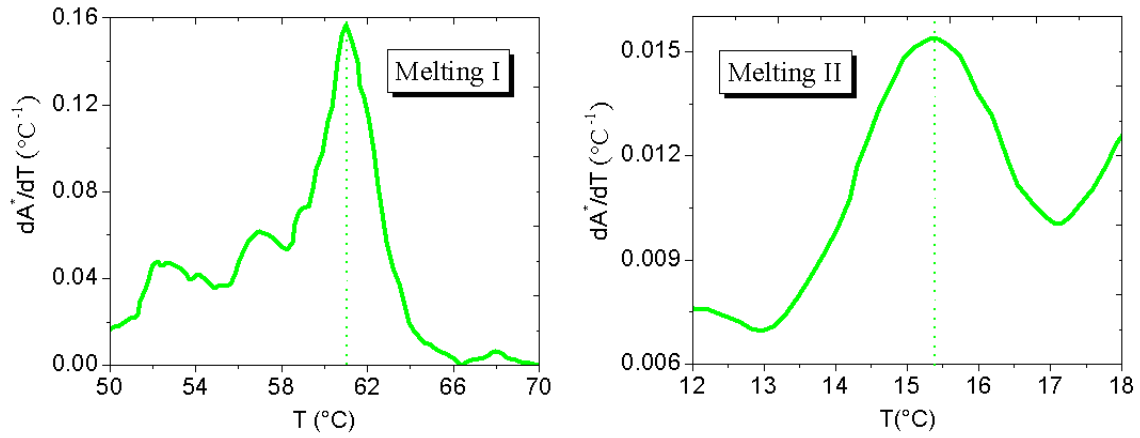

Figure 4.7: First derivative of the absorbance signal for both the observed melting processes (50 mM NaCl).

be thus be ascribed to the formation of DNA nanostars from the solution of complementary ss-DNAs. By further lowering the temperature, one can find a well-defined temperature interval, ranging roughly from 45°C to 25°C (inset of Fig. 4.6), in which the absorbance values remain constant. Such region confirms the presence of a temperature interval in which DNA nanostars are formed but not yet interacting. At lower temperatures, a further decrease in the absorbance indicates the formation of bonds between different structures through the hybridization of the sticky terminals. Clearly, as this hybridization process involves only six bases, the associated absorbance decrease is much less pronounced than the previous one. Nevertheless, it is still enough to evaluate the experimental melting temperature for this process, which results $T_m = 15.4$°C

Ionic strength dependence

Once established the validity of the melting protocol, we performed a series of analogous cooling experiments, aiming at investigating the effect of the ionic strength on the temperature behaviour of our system.
Indeed, as already discussed, the melting temperature of a DNA strand crucially depends on the salt concentration of the medium: in low salt, a given DNA sequence will melt at a lower temperature than in a higher salt concentration. Such behaviour can be ascribed to the polyanionic nature of the DNA molecule. In fact, the salt has an effective role in "shielding" the negative charges of the phosphate groups: when such charges are not shielded, the electrostatic repulsion makes it energetically more favorable to separate the strands, lowering the melting temperatures.
Therefore, in principle, the temperature behaviour of the system may be tuned by simply changing the ionic strength of the medium.
In order to check the validity of such assumption, we prepared several solutions of DNA nanostars, fixing the DNA concentration to 0.075 mg/ml and progressively increasing

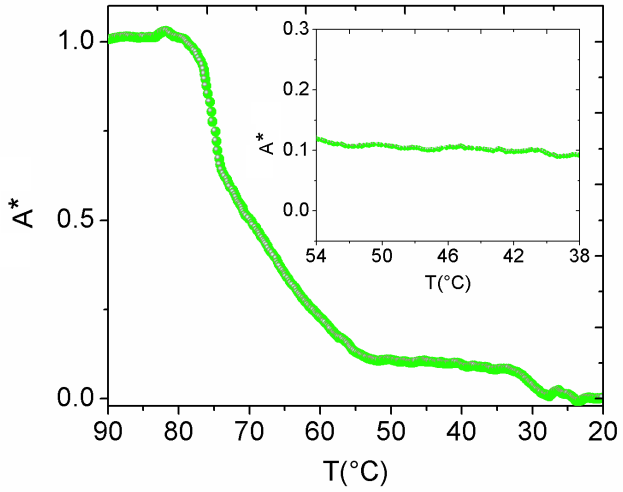

Figure 4.8: Cooling profile for a solution of $f = 3$ nanostars (500 mM NaCl). The inset shows the T-interval in which the absorbance remains nearly constant.

the ionic strength of the solutions (up to 500 mM NaCl). As a significant example, we discuss in the following the cooling profile (90° - 20°C) of a DNA sample having a 500mM NaCl ionic strength. The experimental melting curve is reported in Fig. 4.8. As it can be easily seen, the higher ionic strength results in a significant shift of both melting processes towards higher temperatures (Fig. 4.9). As a consequence, the temperature interval in which the nanostars are well-formed but weekly interacting is still present, but it also shifted towards higher T values (inset in Fig. 4.8).

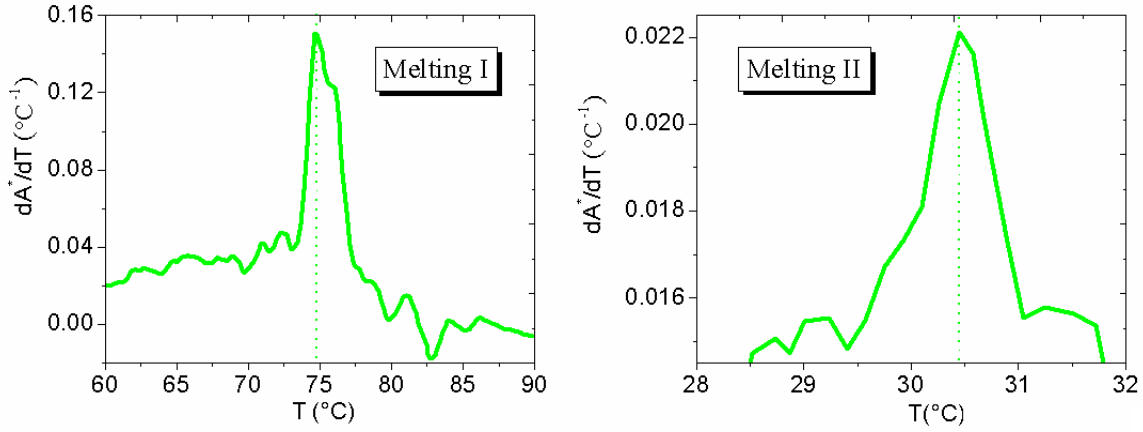

Figure 4.9: First derivative of the absorbance signal for both the observed melting processes (500 mM NaCl).

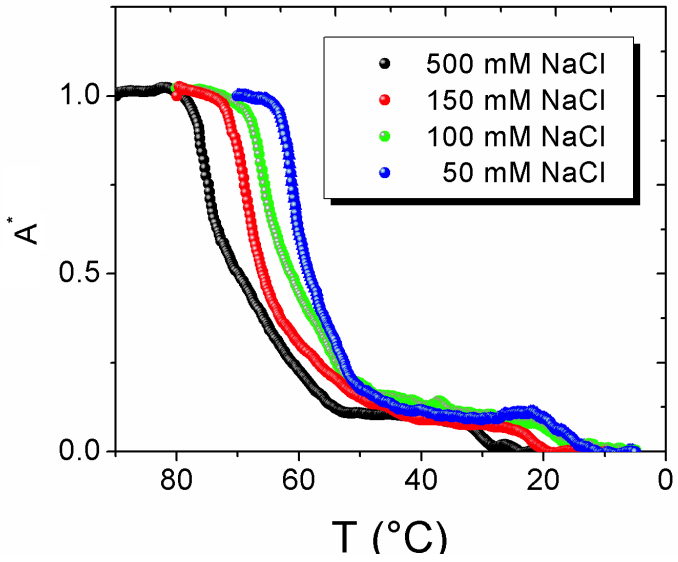

Figure 4.10: Cooling profile for a solution of $f = 3$ nanostars at different salt concentrations.

Therefore, as expected, the ionic strength of the solutions plays a very thin role on the temperature behaviour of our system which can be successfully monitored via UV absorption.
A comparative summary of the experimental cooling profiles at different salt concentrations is reported in Fig. 4.10.
As we will show in the following, such results provided a robust reference for subsequent experiments on the dynamic behaviour of $f = 3$ DNA nanostars at different salt concentrations.

$[Na^+]$ (mM)	T_m^I(°C)	T_m^{II}(°C)
50	61.0	15.4
100	65.7	19.3
150	68.8	21.9
500	74.6	30.4

Table 4.1: Summary table of the experimental melting temperatures for $f = 3$ nanostars.

Reversibility

So far, we have shown how UV absorption measurements can be used to experimentally verify the programmed self-assembly of the desired structures as well as to control the

effects of the ionic strength on the melting processes.
Anyhow, a crucial point that still needs to be investigated is related to the thermo-reversibility of the observed temperature behaviour. Indeed, a fundamental and widely exploited feature of programmable DNA interactions is given by their thermo-reversible nature, which make them appealing for the design of innovative smart materials.
In this respect, following our purpose of creating a thermo-reversible equilibrium gel of limited-valence DNA nanostars, we performed further melting experiments to directly evaluate the reversibility of the assembling processes.
Being our samples chemically resistant to heat degradation, we carried out a simple reversibility test, which consists of a melting cycle (cooling→ heating) starting with a cooling experiment. Indeed, starting from a low temperature implies that the initial state corresponds to a thermodynamic equilibrium state, and it is often difficult to estimate the incubation time required to achieve it. At high temperature, on the other hand, the samples should be denatured, and the dissociated state is thus well defined. An example of such a cooling-heating experiment is presented (80°C $\rightarrow$ 10°C $\rightarrow$ 80°C) in Fig 4.11.
As it can be seen, the heating and cooling profiles are perfectly superimposable. Such behaviour indicates that any experimental problems, e.g., presence of air bubbles in the solution, evaporation at high temperature, sample degradation, have been successfully avoided and that the observed transitions are both kinetically reversible.

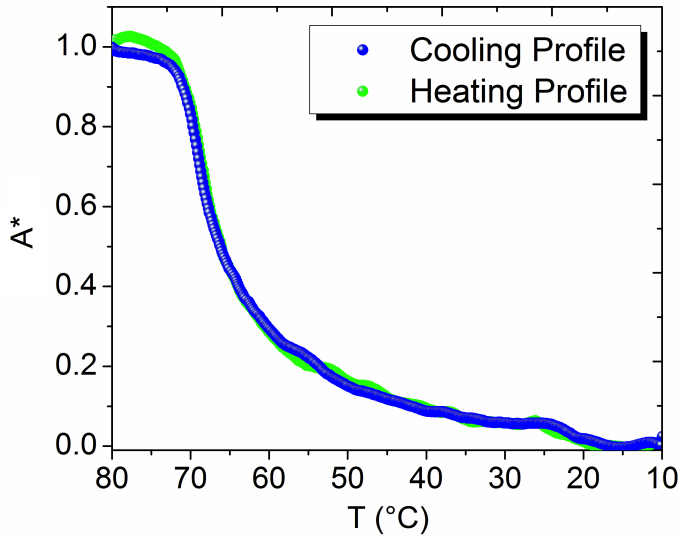

Figure 4.11: Superimposable heating and cooling profiles for f=3 nanostars (150mM NaCl).

4.3.3 AFM Visualization

Once verified the validity of our protocol of structure formation, we performed a series of AFM measurements on samples of DNA nanostars in order to visualize both the structure of the isolated DNA constructs as well as the texture of the self-assembled samples. Due to the nanometric dimensions of the individual nanostars (the double helical arms consists of 20 bp, i.e. approximately 8 nm), such measurements required special attention to obtain good resolution images. Anyhow, AFM visualizations of nanometric DNA structures (such as Y-shaped, H-shaped or DNA polyhedra) previously reported in literature [109, 110] ensured the feasibility of such delicate measurements.
As already mentioned, in order to be properly resolved by AFM, samples must be immobilized onto flat, smooth, stationary substrates. To this purpose, after numerous trials, we developed a specific protocol for the immobilization, incubation and visualization of our DNA samples. Specifically, such method involved the use of divalent cations (i. e. Mg^{2+}) as bridges to immobilize charged DNA molecules onto mica surfaces.
The main steps of the protocol are schematically summarized in the following:

- Sample dilution with 2mM $MgCl_2$ solution;
- Deposit onto freshly cleaved mica;
- Overnight incubation to electrostatically immobilize the investigated samples on the mica surface (this step may be done at room temperature or in a controlled temperature environment);
- Rinsing with ultra-pure deionized Milli-Q water (electroresistance above $18\, m\Omega\, cm^{-1}$);
- Drying under nitrogen flux;
- Promptly imaging using Tapping-Mode AFM.

Following the scheme, we managed to visualize with proper resolution the self-assembled nanostars deposited on the mica substrate. In order to reduce experimental problems related to adhesion of the sample on the AFM probe, we started the AFM investigation by using solutions of highly diluted DNA nanostars (i.e. 0.1 mg/ml). In fact, since the tip of the AFM probe and the mica substrate have similar surface chemistries, the cations and the DNA sample can also stick to the AFM probe in a similar manner as they adhere to the mica. All measurements were performed at room temperature.
Fig. 4.12 shows an example of good resolution images obtained by using TM-AFM. As it can be seen, after the incubation, isolated nanostars adhere to the mica substrate. In the white frame, panel b, one can clearly observe a branched structure (the area within this frame is shown at a greater magnification in panel c). The height profile along the white line (Fig. 4.12d) confirms that the observed structure is a DNA structure, being its height slightly lower than 2 nm, as expected for DNA deposited onto mica surfaces [113]. Since AFM measures topography, it actually collects matrices of data (x, y, z) relative to the scanned areas: a tridimensional graph can thus be plotted to have an

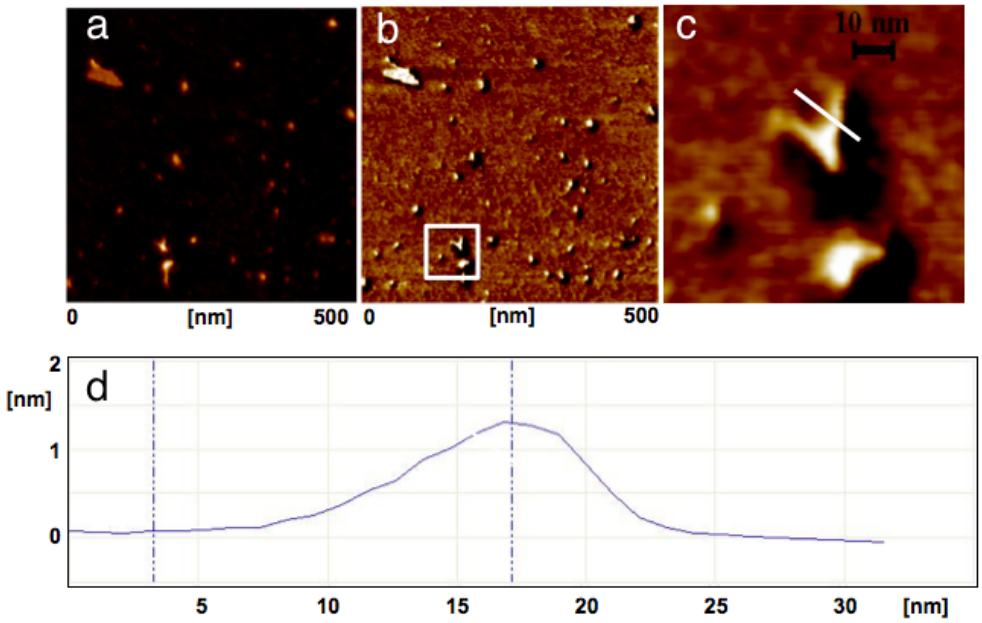

Figure 4.12: AFM images of isolated DNA nanostars: topography channel (a) and phase channel (b). The area within the white frame is shown at greater magnification in panel (c). Panel (d) shows the height profile along the white line in the image of panel (c).

accurate visualization of the investigated structures. Therefore, to better resolve the observed branched structure, a tridimensional plot is reported in Fig. 4.13.
Fig. 4.14 shows another example of high resolution AFM visualization of our nanostars.

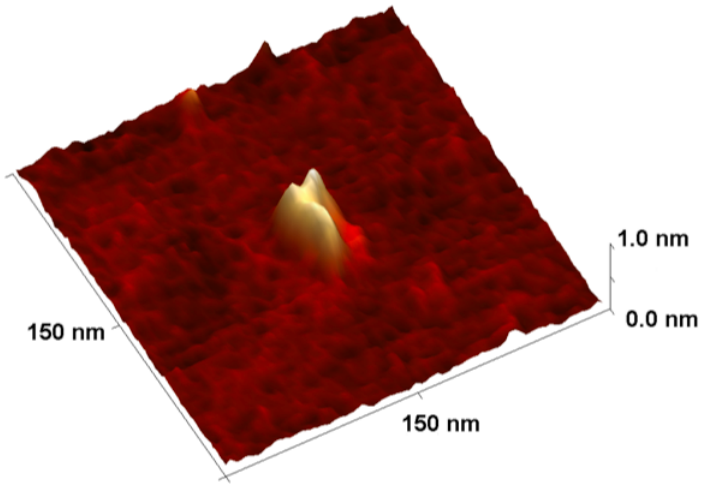

Figure 4.13: 3D visualization of an isolated $f = 3$ nanostar.

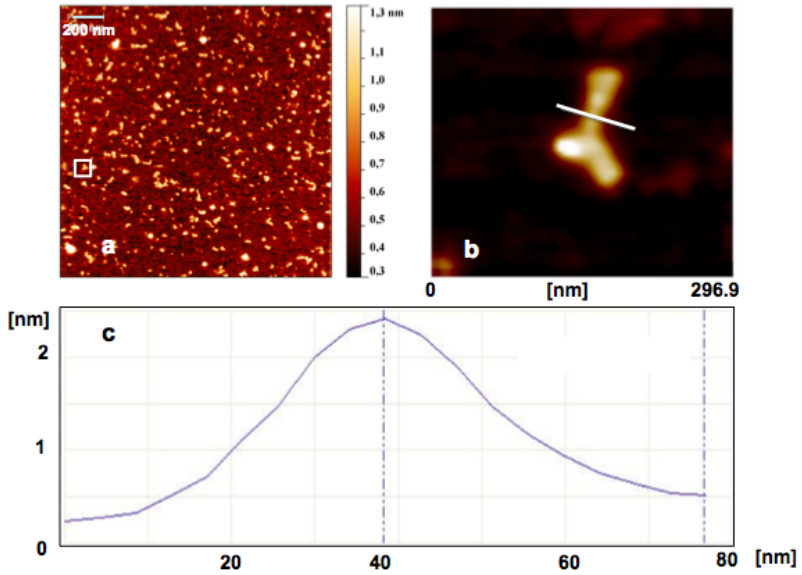

Figure 4.14: AFM images of isolated DNA nanostars: topography channel (a). The area within the white frame is shown at greater magnification in panel (b). Panel (c) shows the height profile along the white line in the image of panel (b).

As the DNA concentration is higher than the previous one (0.2 mg/ml), it is possible to observe a large number of branched DNA structures, isolated or bonded one to the other.

Again, in Fig. 4.14b, we show a magnification of a well-resolved trimeric structure, with the height profile relative to the white line (Fig. 4.14c). Even in this case, the height distribution is compatible with the expected one for DNA chains immobilized onto mica substrates. Interestingly, the tridimensional representation shown in Fig. 4.15 confirms the expected open and flat structure for the $f = 3$ nanostars, which can

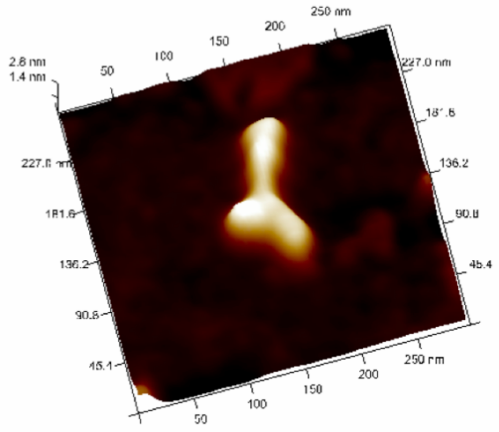

Figure 4.15: 3D visualization of an isolated $f = 3$ nanostar.

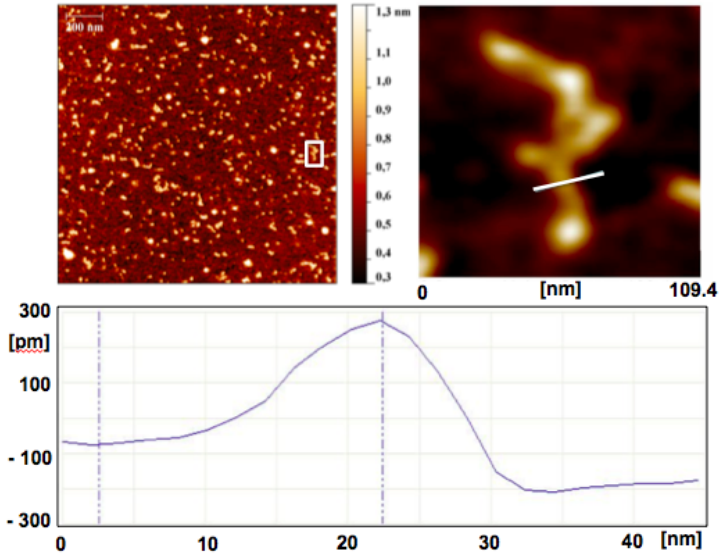

Figure 4.16: AFM images of two bonded DNA nanostars: topography channel (a). The area within the white frame is shown at greater magnification in panel (b). Panel (c) shows the height profile along the white line in the image of panel (b).

be reasonably ascribed to the electrostatic repulsion between the negatively charged double helical arms.
A careful look to Fig. 4.14, panel a, reveals that, even at such low concentration, some nanostars result bonded to the neighbouring ones. Even if complex aggregates are difficult to resolve, appearing as large clusters of amorphous and not well defined shapes, smaller aggregates (e.g. of only two nanostars) can be easily identified. A well-resolved example is reported in Fig. 4.16. Even in this case, the 3D reconstruction is helpful for visualizing the structural details of the two bonded nano-structures.

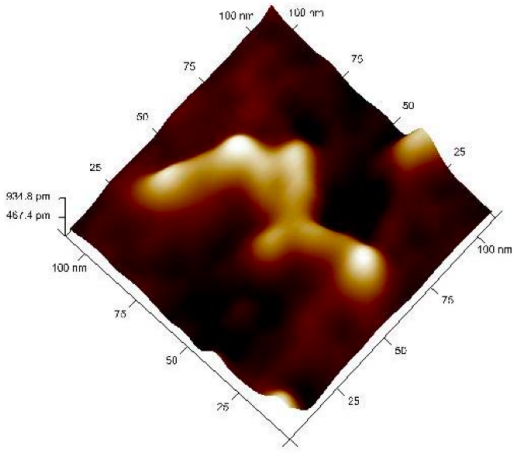

Figure 4.17: 3D visualization of two bonded $f = 3$ nanostars.

One fundamental point that need to be discussed involves the apparent sizes of the observed structures. In fact, due to the convolution with the tip of the AFM probe, the objects visualized through this technique tend to be larger than the real ones. Such a problem has been deeply investigated in the AFM field and it apparently originates from the geometry of the AFM probe tip itself which can directly affect the image resolution, thus creating imaging artifacts. Currently, the most common method to avoid the problem is to use appropriate AFM tips with a curvature radius smaller than the characteristic sizes of the investigated structures.
Following this line, we performed all the measurements using a tiny tip, with a very small radius of curvature (2 nm), which is particularly useful in preventing imaging artefacts related to the tip geometry. The selected tip significantly minimizes this effect, though the observed star-shaped DNA structures still appear slightly larger than they actually are.

Network of bonded DNA nanostars

Once visualized the isolated nanostars, we performed a set of measurements aimed at investigating the texture of the self-assembled network.
Indeed, as already discussed, each arm of the nanostars terminates with a self-complementary sequence which allows for the mutual association via Watson-Crick base pairing of the overhangs of close-by structures. Therefore, we expected that at sufficiently low temperature (i.e. lower than the melting temperature of the overhangs) a spanning network of bonded nanostars should be present in our samples.
Since, as shown by UV measurements, the melting temperatures crucially depend on the salt concentration, the samples for this investigation were prepared by using an electrolyte solution having 500 mM NaCl ionic strength, so that the network already forms at room temperature. Higher salt concentrations need to be avoided, as the presence of salt crystals may interfere with the AFM measurement, with the serious risk of irreparably damaging the tiny AFM tip.
With the same purpose of creating a network of bonded nanostars, we increased the DNA concentration so to have a much denser sample (the total DNA concentration is equal to 2.5 mg/ml).
Moreover, to ensure the proper formation of the spanning network, we slightly varied the preparation protocol, performing the deposition and incubation of the sample directly in an environment with a controlled temperature of $T = 4°C$.
By using these shrewdnesses, we managed to immobilize the network of bonded structures on the mica surface.
Fig. 4.18 shows an AFM topographic scan of the sample surface. As it can be seen, the topographic profile exhibits evident differences with respect to the previous samples. Indeed, while in the previous cases, samples were mainly characterized by the presence of individual nanostars (or small clusters of few aggregated ones), the present one clearly shows the coexistence of a network of bonded nanostars (white arrows) and of isolated ones (white squares). Such result nicely supported the expected temperature behaviour

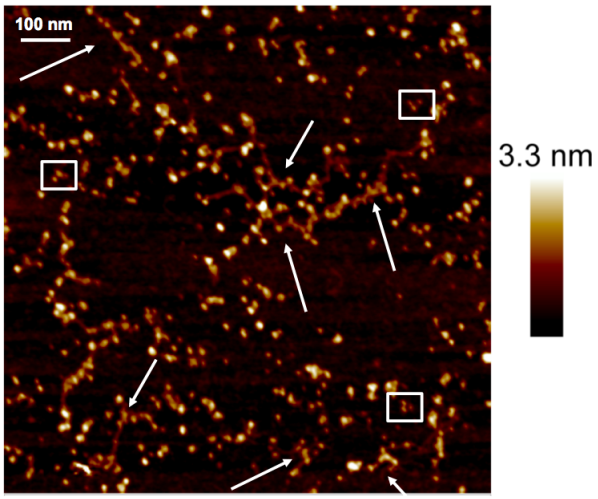

Figure 4.18: AFM topographical scan of a sample of $f = 3$ nanostars ($c_{DNA} = 2.5\,mg/ml$).

of the system, confirming the possibility of creating networks of self-assembled DNA structures by simply exploiting the Watson-Crick base pairing.
From the tridimensional plot (Fig. 4.19) one can accurately visualize the texture of the self-assembled network, which appears to be constituted of structures whose sizes are compatible with ones expected for our $f = 3$ nanostars.

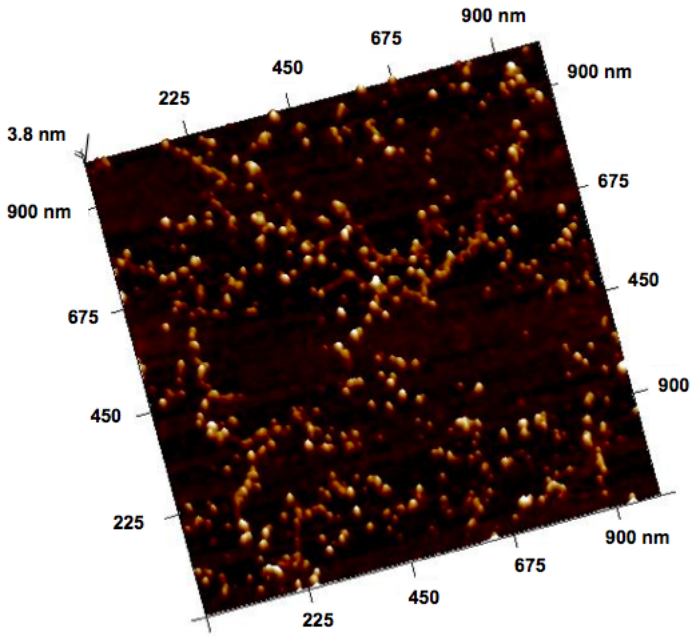

Figure 4.19: 3D visualization of a sample of $f = 3$ nanostars ($c_{DNA} = 2.5\,mg/ml$).

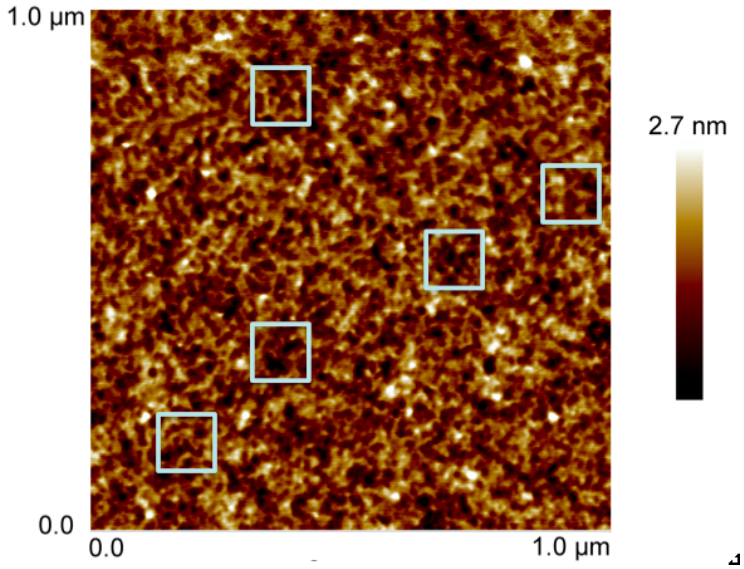

Figure 4.20: AFM topographical scan of a sample of $f = 3$ nanostars ($c_{DNA} = 9.0\,mg/ml$).

A further attempt to visualize the texture of the network of bonded nanostars was done by using a different strategy.
Specifically, we tried to significantly increase the DNA concentration up to $c_{DNA} = 9.0\,mg/ml$ (in 50 mM NaCl), where, as we will see in Chapter 5 and 6, we expected the formation of a stable DNA hydrogel at low enough temperatures.
Hence, as in the previous case, we performed the deposition and incubation of the sample directly in an environment with a controlled temperature of $T = 4°C$.
Once again, in line with the expectations, AFM reveals the presence of a network of bonded nanostars.
A topographical scan of the investigated sample is reported in Fig. 4.20.
As it can be seen, the difference with the previous sample, prepared at much lower DNA concentration, is evident. Indeed, in the present case, we can easily observe the occurrence of a network of much more tightly bonded DNA nanostars which is in line with the expected topography of biological hydrogels.
Trimeric entities are difficult to recognize in the thick texture of the gel. Nevertheless, some of them can hardly be observed in the regions where the texture of the network is less compact (white squares in Fig. 4.20).
Currently, we are working to analyze the periodicity of the image in order to quantitatively estimate the mesh size of the self-assembled hydrogel.
As shown in Fig. 4.21, the height distribution associated to the previous AFM scan is centered on a value which is compatible with the one expected for DNA nanostructures, thus confirming the formation of a gel entirely made by all-DNA particles.
By combining the precedent information, it was possible to obtained a tridimensional reconstruction of our DNA hydrogel (Fig. 4.22).

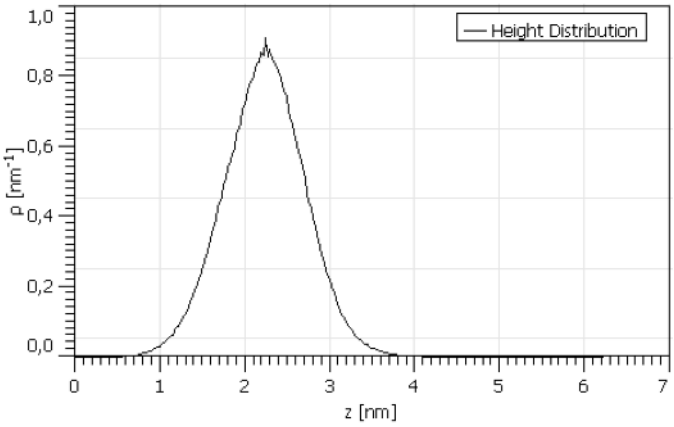

Figure 4.21: Height Distribution associated to the topographical scan of Fig. 4.20.

As it can be seen, the image appears slightly more noisy than the ones obtained for samples at lower DNA concentrations. Indeed, at such high DNA densities, the enhanced viscoelasticity of the sample hampered the successful execution of the measurement.

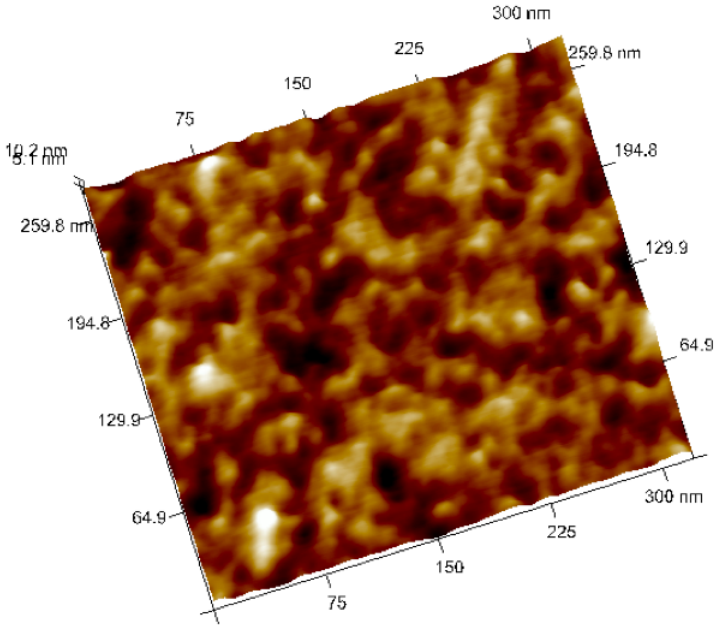

Figure 4.22: 3D visualization of a sample of $f = 3$ nanostars ($c_{DNA} = 9.0\,mg/ml$).

Chapter 5

DNA goes critical

"There is no such thing as a failed experiment,
only experiments with unexpected outcomes"

Richard Buckminster Fuller

One of the most intriguing peculiarities of our DNA nanostars is represented by the possibility of finely tuning their self assembling behaviour by simply changing the temperature of the system. In the previous chapter we have shown how this possibility can be experimentally proved: to this aim, we have introduced our limited-valence DNA nano-structures and systematically characterized their peculiar temperature behaviour. Here, instead, we address the fundamental issue of experimentally determining the phase diagram of such limited-valence DNA particles, with the specific purpose of testing recent theoretical predictions concerning the key role played by the valence on the phase behaviour of colloidal systems.
In order to do this, in the first section of this chapter we focus on the phase separation phenomena that we observed in our solutions of DNA nanostars (in a well-defined range of DNA concentrations) on cooling down the systems below a critical temperature value. Specifically, after showing empirical evidences confirming the occurrence of phase separation in our samples, we present an experimentally determined phase diagram for $f = 3$ and $f = 4$ nanostars.
Moreover, in the second section, we deeply investigate the critical behaviour of DNA samples, showing how scattering experiments can be used to directly monitor the critical phenomena, providing accurate estimates of important parameters, such as the critical temperature or the correlation length of the systems.
Eventually, in the last section, we discuss the results of a series of DLS measurements performed on critical samples which clearly indicates that the dynamics of our systems is surprisingly much richer than anticipated. Indeed, as the critical point is approached, the field correlation functions become characterized by a two-step relaxation process. Interestingly, the slow relaxation time exhibits an Arrhenius behaviour with no signs of criticality, thus demonstrating a novel scenario where the critical slowing down of the concentration fluctuations is enslaved to the large lifetime of the sticky bonds.

5.1 Phase behaviour of DNA nanostars

As already mentioned, one of our main goals was the experimental investigation of the phase behaviour of $f = 3$ nanostar systems.
To this aim, we systematically explored a large window of DNA densities in a rather wide range of temperatures to determine the region in which the system forms a supramolecular network, the region in which the network becomes nonergodic and the region in which the network formation is precluded by phase separation (a schematic representation of these regions is shown in Fig. 5.1).
By comparing the results of such investigation with the ones obtained by the research group of Prof. T. Bellini on $f = 4$ solutions, we were able to evaluate the role played by the valence on the phase behaviour of our systems.

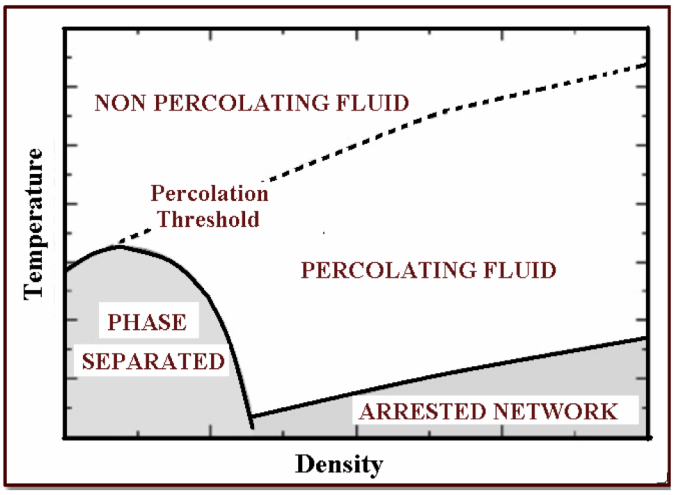

Figure 5.1: Schematic representation of the relevant thermodynamic and dynamic properties of network-forming limited-valence systems.

5.1.1 Meniscus visualization

On discussing the temperature behaviour of our systems (Sec. 4.1.1), we have shown that below a specific temperature value T_b (defined as the temperature at which 10% of the sticky ends are hybridized), the interactions between overhangs of different nanostars start becoming relevant. As a consequence, for $T < T_b$, a state can be found in which the nanostars are bound in a percolating network (which eventually arrests at very low temperatures).
In such a frame, phase-separation may open an even more interesting scenario. Indeed, if the DNA concentration of the investigated solution falls inside the window of concentrations (densities) at which phase separation is expected to occur (Fig. 5.1), at sufficiently low temperatures we should detect a phase-separation process inside our sample.

In order to verify this expected behaviour, we prepared a set of $f = 3$ samples at various DNA concentrations, ranging from 1.7 mg/ml to 6.5 mg/ml (the ionic strengths of the solutions were chosen to yield similar ionic conditions in all the samples despite the difference in the DNA concentrations. For all the samples here investigated, the resulting conterion concentration is about 50 mM NaCl).
At room temperature, all the samples remained homogeneous with no detectable sign of phase separation. Anyhow, by decreasing the temperature below a specific DNA concentration-dependent value, we discovered a dim meniscus of phase separation between two phases differing in nanostars concentration. Visual inspection of the meniscus and of its temperature dependence provided a qualitative characterization of the coexisting densities, allowing for a preliminary localization of the region of instability.
To speed up the observed macroscopic process of phase separation and to properly visualize the coexisting phases, samples were centrifuged at 3000g for several hours, by using a refrigerated/heated centrifuge (EPPENDORF 5702 RH), helpful for achieving a sharper meniscus inside the samples. The use of a temperature-controlled centrifuge allowed to determine, for each investigated DNA concentration, a specific value of temperature T^* such that, samples centrifuged at $T < T^*$ developed a clear meniscus, while samples centrifuged at $T > T^*$, did not exhibit any sign of phase separation.
It is worth to mention that, while in solutions of $f = 4$ nanostars the difference in density between the two coexisting phases was large enough to enable an easy visualization of the meniscus by naked eye, in the case of the solutions of $f = 3$ structures, the visual inspection of the meniscus was much harder and not always possible.
To overcome such difficult, samples were visualized using a Leica Fluorescence Microscope (CCD Zeiss AxioCam ICc3 Digital Camera) endowed with a 20x objective which allowed for a high resolution visualization of the meniscus inside the samples (Fig. 5.2).

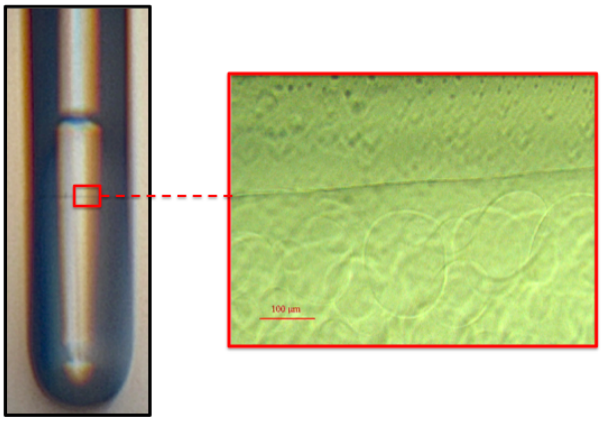

Figure 5.2: Fluorescence microscope visualization of the meniscus (Mag 20x). On cooling, all investigated samples were found to phase separate into coexisting small droplets, providing evidence of a phase separation process between two phases differing in particle concentration.

5.1.2 Phase Diagram

Once located the region of instability for $f = 3$ nanostars, in collaboration with the group of Prof. Bellini, it was possible to directly evaluate the coexisting concentrations via UV absorption.
Specifically, by measuring the absorbance at 260 nm for different temperatures, we managed to determine the temperature-dependence of the DNA concentration in the two phases for both $f = 3$ and $f = 4$ nanostars and to build the phase diagram reported in Fig. 5.3 [114]. As mentioned, all the measurements here presented refer to nanostar solutions having an ionic strength of approximately 50 mM NaCl.
Operatively, to determine such phase diagram, identically prepared samples of $f = 4$ and $f = 3$ DNA nanostars were inserted into capillaries and cooled down to the target temperatures. After a 4 hour-centrifugation at 3000g, each capillary was cut in sections and for each of them the DNA concentration was determined by measuring the absorbance at 260 nm with a Thermo Scientific NanoDropTM 1000 Spectrophotometer (all the measurements were performed in the Department of Medical Biotechnology and Translational Medicine, University of Milan).
As it can be seen, the range of DNA concentrations where phase separation takes place is rather limited and it significantly decreases on going from $f = 4$ to $f = 3$.

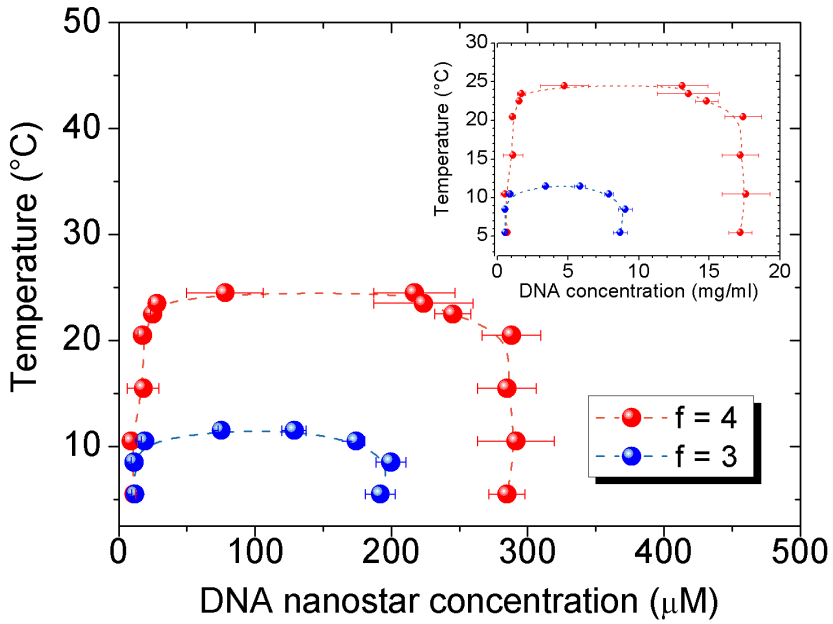

Figure 5.3: Experimentally determined consolution curve for nanostars with $f = 3$ (blue dots) and $f = 4$ (red dots) in the temperature - nanostar concentration plane. The inset shows the same consolution curve as a function of the total DNA concentration (mg/ml) of the solutions.

Indeed, our data indicate that the dense phase at coexistence for $f = 4$ and $f = 3$ nanostars have markedly different DNA concentration, in good agreement with the theoretical predictions [16] based on Werheim thermodynamics perturbation theory. Interestingly, the concentration of the dense phase for both systems is comparable to the concentration of regular networks in which DNA nanostars are fully-bonded with f neighbours each. Indeed, simple geometrical considerations indicate that the DNA concentration of such networks is rather small and strongly depends on the nanostar valence. For instance, a diamond lattice formed by $f = 4$ nanostars in which all paired arms were perfectly aligned would have a DNA concentration of $c_{DNA} \approx 13.3\, mg/ml$ (this clearly represents a low estimate, since any bending fluctuation of the bonded nanostar arms may reduce their distance, increasing the concentration). Our findings thus indicate that the dense fluid phase has indeed a density comparable to the fully bonded network state.
Moreover, we also found that the critical temperature of the system significantly decreases upon lowering the valence, varying from $T_C \sim 25$°C for $f = 4$ nanostars to $T_C \sim 11$°C for $f = 3$ ones.
Therefore, besides providing the first experimental observation of a critical behaviour in DNA solutions, such results nicely confirm the theoretical and numerical predictions [16] concerning the role of the valence on the phase behaviour of limited-valence systems. Indeed, in line with the expectations, the region of instability is found to significantly shrink upon decreasing the valence and the critical parameters of the system (i.e. temperature and nanostar concentration) appear to be strongly dependent on f.

5.2 Critical Behaviour

The experimentally determined consolution curve (Fig. 5.3) necessarily terminates, at high temperature, in a critical point, which marks the divergence of the concentration fluctuations. Therefore, in order to characterize the critical behaviour of our DNA nanostars and to provide evidence that the observed phase separation originates from a second-order critical phenomenon, we investigated the amplitude and the dynamics of the pre-transitional concentration fluctuations by studying the amplitude and the intensity fluctuations of the light scattered by the solutions.
Specifically, a solution of $f = 3$ nanostars was prepared at the critical concentration (i.e., according to the experimental phase diagram, at $c_c = 4.5\, mg/ml$) and, starting from high temperatures, the temperature of the system was slowly cooled down to approach T_c. Measurements were done via static and dynamic light scattering, for different angles covering the wave-vector range $8.2\, \mu m^{-1} < q < 30.6\, \mu m^{-1}$. This experimental approach takes advantage of the large refractive index of DNA, enabling an effective detection of concentration fluctuations. All the measurements were performed in the one-phase region, by firstly thermalizing the sample at 45°C for 2 hours and then progressively cooling it in steps. After changing temperature, the sample was allowed to thermalize for approximately 2 hours before running measurements.

5.2.1 T-dependence of the scattering intensity along the critical isochore

As discussed in Sec. 3.1.4, the Ornstein-Zernike theory of dynamic critical phenomena predicts that the scattered intensity $I(q)$, for small values of q, is properly described by a Lorentzian shape (in addition to a small non-critical background component I_{nc}):

$$I(q) = \frac{I_L(0)}{1 + q^2\xi^2} + I_{nc} \tag{5.1}$$

where the zero-wavevector Lorentzian component $I_L(0)$ and the correlation length ξ diverge as power laws $I_L(0) = I_0(T/T_c - 1)^{-\gamma}$and $\xi = \xi_0(T/T_c - 1)^{-\nu}$ with Ising critical exponents $\gamma = 1.237$ and $n = 0.630$ [115]. I_0 and ξ_0 provide the reference values of the critical scattering intensity and of the thermal correlation length far from the critical point, while I_{nc} accounts for the (small) non-critical component of the scattered intensity.
Such equation properly expresses the dependence of the scattering intensity on the temperature and on the scattering wavevector in the critical region and it can thus be used to accurately estimate important critical parameters such as T_c.
In order to do this, as already mentioned, the intensity scattered by a solution of $f = 3$ nanostars (prepared at the critical concentration) was detected at different angles by cooling down the system along the critical isochore (Fig. 5.4).
The simultaneous best fit of the scattered intensity at all the measured T and q values provided a robust estimate for the four fitting parameters T_c, ξ_0 , I_0 and I_{nc}.

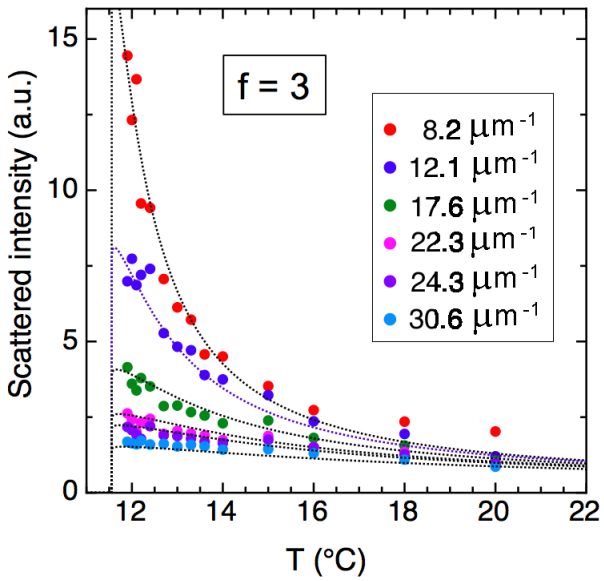

Figure 5.4: Intensity scattered by solutions of $f = 3$ nanostars at the critical density. Measurements were performed at different scattering angles. Lines represent the lorentzian fit (Eq. 1). Figure from [114].

An analogous analysis has been performed on solutions of $f = 4$ nanostars.
The resulting values for the critical temperatures are: $T_c = 11.6 \pm 0.1\,^{\circ}C$ and $Tc = 25.5 \pm 0.1\,^{\circ}C$ for $f = 3$ and $f = 4$, respectively.
The best fit yields $\xi_0 = 3.2$ nm and $\xi_0 = 1.9$ nm for $f = 3$ and $f = 4$, respectively. These values are in the range of the hydrodynamic radius of the nanostar (≈ 4.5 and 4.7 nm for $f = 3$ and $f = 4$) and reflect the different critical density of the two systems, smaller in the case of $f = 3$.

Critical opalescence

The marked increase of the intensity as the critical temperature is approached provides a clear evidence of the growth of critical concentration fluctuations. In fact, as already discussed, sufficiently close to a critical point, the correlation length of a system may significantly increase, becoming as large as the wavelength of the light used to investigate the sample. In this condition, density inhomogeneities in the scattering medium diffuse light strongly, thus causing a critical opalescence phenomenon, which can be easily detected in critical samples.
Fig. 5.5 shows the time fluctuations of the intensity scattered at 90° by the solution of $f = 3$ nanostars at the critical concentration.
As it can be seen, on cooling down the system from high temperature, the intensity fluctuations become progressively more and more pronounced. In proximity of the critical point (T=12.7°C), we can clearly detect the onset of critical fluctuations, signaling the imminent phase separation of the sample.

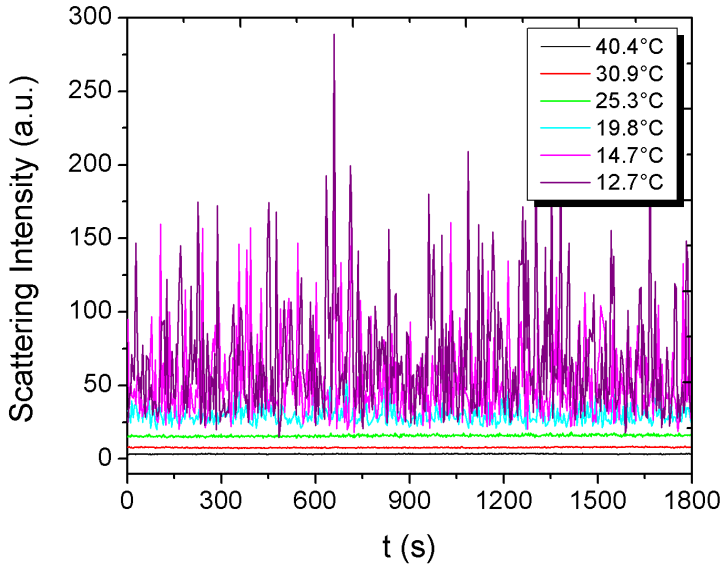

Figure 5.5: Fluctuations of the intensity scattered at 90° by a solution of $f = 3$ nanostars at the critical density. Close to the critical point, critical opalescence enhances the fluctuations.

5.3 Dynamic Behaviour

Once characterized the critical behaviour of DNA nanostar systems, we focussed our attention on the experimental investigation of their dynamics. Specifically, through dynamic light scattering it was possible to characterize the collective density fluctuations of the systems in a wide region of temperatures and densities. Indeed, the shape of the correlation functions, associated to the quantitative information inferred from the scattering intensity, allowed to accurately quantify the approach to the gel state as well as the approach to the thermodynamic instability at low densities.

5.3.1 Field autocorrelation functions for $f = 3$ nanostars

Fig. 5.6 shows a set of field autocorrelation functions, reflecting the kinetics of the DNA concentration fluctuations, measured via dynamic light scattering at the critical concentration. Analogous measurements were performed on several solutions at various DNA concentrations, by firstly thermalizing the samples at 45°C for 2 hours and then slowly decreasing the temperature by steps.
As can be seen, the dynamic behaviour of the system is characterized by the emergence of a two-step relaxation function, with an intermediate plateau whose amplitude grows progressively on cooling.

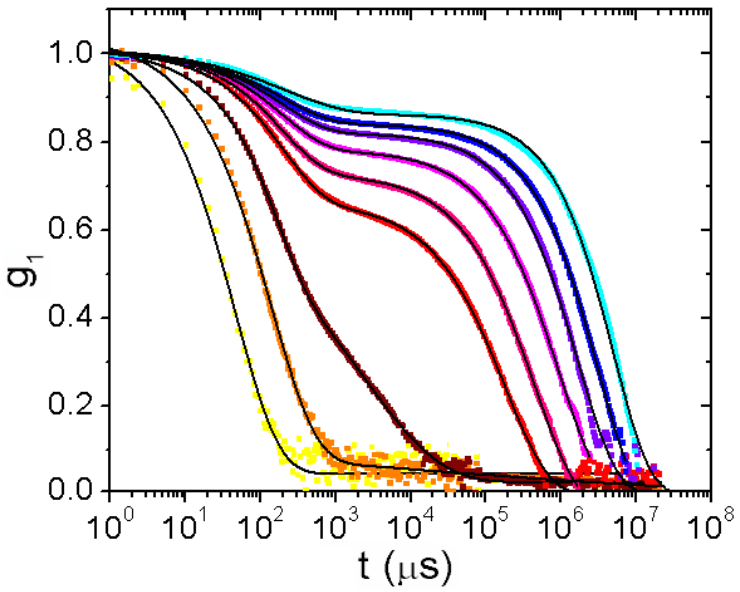

Figure 5.6: Field correlation functions for $f = 3$ nanostars detected at 90° at the critical concentration. Measurements were performed at various temperatures: T = 40.4, 30.9, 25.3, 19.8, 18.1, 16.6, 14.7, 13.7, 12.7 °C (symbols). Data are fitted to a single stretched exponential for T =40.4°C and to a sum of two stretched exponentials for the other Ts (lines).

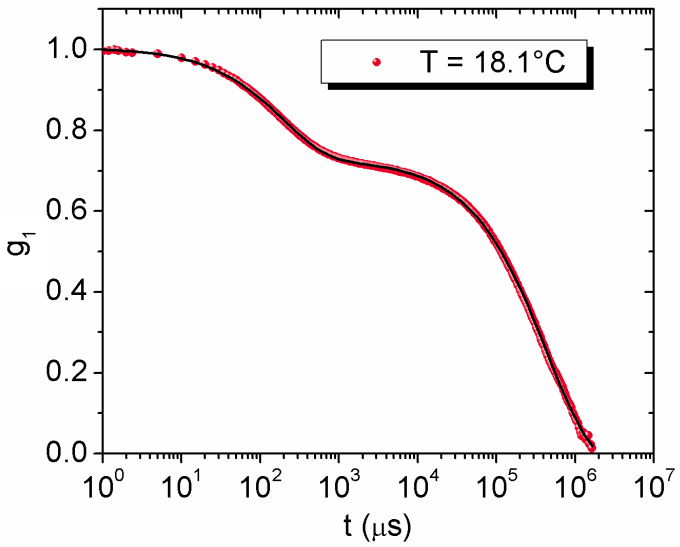

Figure 5.7: Example of two-step correlation function (dots) for $f = 3$ nanostars at at the critical concentration. The black line indicates the double stretched exponential fit (Eq. 5.2)

This suggests that initially the correlations decay in a frozen environment, with a timescale significantly different from the slow-process. Only for long time, the structure relaxes the correlations to zero.
It was found that the observed two step correlation functions can be well fitted to the sum of two stretched exponentials:

$$g1(\tau) = A_f \cdot e^{-(\frac{\tau}{\tau_f})^{\beta_f}} + A_s \cdot e^{-(\frac{\tau}{\tau_s})^{\beta_s}} \tag{5.2}$$

where A_f, τ_f and β_f represent respectively the amplitude, the characteristic time and the stretching exponent associated to the fast relaxation process. Analogous notation holds for the slow component.
Fig. 5.7 shows an example of correlation function (dots) and double stretched exponential fit (line).
A closer inspection to the observed behaviour of the field correlation functions enables to interpret the dynamics of the system: at the highest temperatures explored, the correlation function is a simple exponential (as expected for freely diffusing particles), thus confirming the existence of a range in which the constructs are formed and their interaction is weak.
Instead, as the critical point is approached, the field correlation functions become characterized by a two-step relaxation process, with the appearance of a plateau whose height (the so-called non-ergodicity factor in glass physics [116]) increases on cooling. Such behaviour clearly reflects the onset of the programmed attractive interactions between DNA overhangs, which gradually increase as the temperature is lowered, leading

to the formation of progressively larger clusters of bonded nanostars whose size diverges at the percolation line. Close to the critical point, which is always located inside the percolation region [117], an infinite cluster is present. The decay of density correlations is thus enslaved to the restructuring time of such infinite cluster and hence controlled by the bond lifetime.

5.3.2 Anomalous dynamic behaviour of nanostar solutions

As seen in the previous section, while $I(q)$ follows what expected from the Ornstein-Zernike theory of the scattering amplitude (Sec. 3.1.4), the dynamic behaviour of system appears to be much richer than anticipated. Indeed, according to the theory of dynamic critical phenomena, we would expect an exponential decay of the correlation functions characterized by a single characteristic time diverging as power-law upon approaching the critical point (the so-called critical slowing down).
Here, instead, we found a two-step relaxation of the correlation functions. Moreover, by fitting the observed curves to the double stretched exponential of eq. 5.2, we discovered an even more surprising behaviour of the characteristic times relative to the two decorrelating processes.
Specifically, as the temperature decreases, the two characteristic times behave very differently (Fig. 5.8). At high temperature, the dynamics is the one expected for independent, free-diffusing DNA nanostars, with a single, exponential decay process with a characteristic time in agreement with what expected from the nanostar radius.

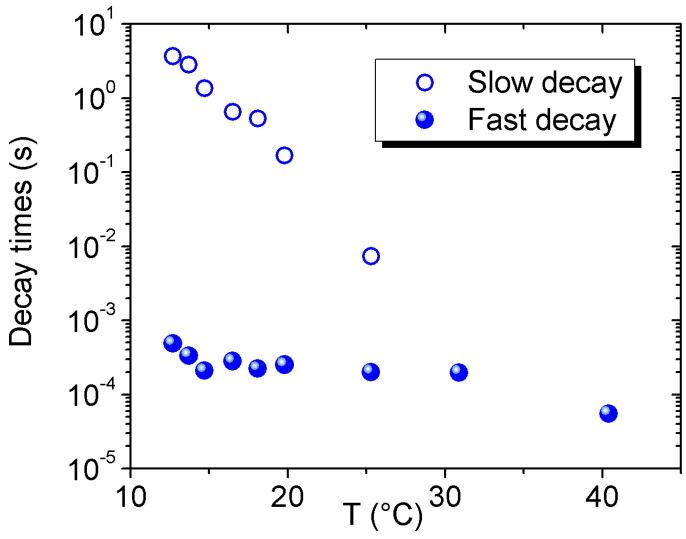

Figure 5.8: T-dependence of the decay times. At high T the system exhibits a single decay, with a decay time indicating a hydrodynamic radius of 4.0 nm, consistent with expectations for independent nanostars. At lower Ts a second, slower, decay arises (open symbols).

As the temperature is lowered, such relaxation develops continuously into the fast component, with the characteristic time of the fast relaxation changing only very mildly, similarly to what expected for the temperature dependence of free diffusion.
Quite different is the behaviour of τ_s, which slows down by nearly three orders of magnitude in a continuous fashion.
As it can be seen, τ_s does not show the power-law divergence which is expected for the critical slowing down.
Fig. 5.9 shows, instead, that the characteristic time of the slow relaxation process behaves surprisingly as an Arrhenius activated process:

$$\tau = \tau_0 e^{-\frac{\Delta G}{k_B T}} \tag{5.3}$$

where τ_0 is the characteristic time found in the limit of high temperatures.
Interestingly, by fitting the slope of $ln(\tau_s)$ as a function of 1/T, it was possible to the determine ΔH, the enthalpic component of ΔG.
Specifically, for the investigated solutions of $f = 3$ nanostars we found ΔH = 82 kcal/mol. Such value corresponds to approximately 1.8 times the enthalpic component expected for the binding of the sticky overhangs (see Sec. 4.1.2).
To extract the entropic component of ΔG associated to the slow relaxation, it was necessary to have an independent estimate of τ_0. A very simple choice is to assume $\tau_0 = \tau_f$, which leads to ΔS = 266 cal/(mol K). Such value corresponds to about 2 times the entropic component expected for the binding of the sticky overhangs (see Sec. 4.1.2), in line with what obtained for the enthalpic component.

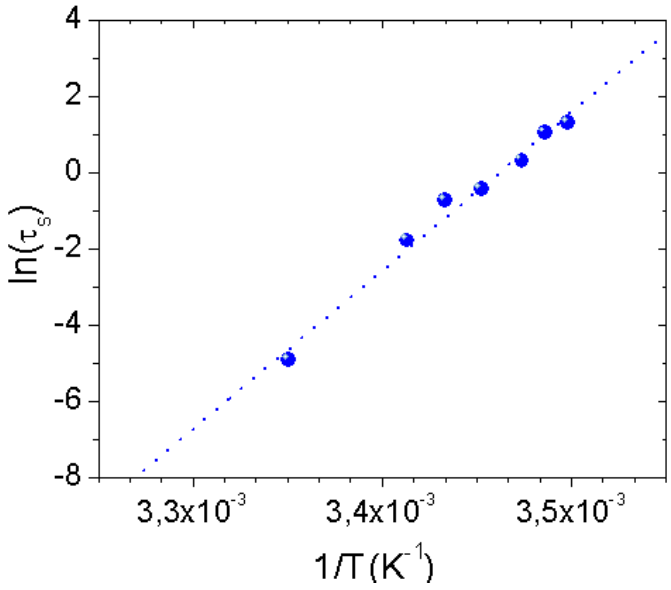

Figure 5.9: $ln(\tau_s)$ plotted as function of 1/T (full symbols) and fitted by an Arrhenius law (dashed line).

	$f = 3$	$f = 4$
ΔH [kcal/mol]	82	120
ΔS [cal/(mol K)]	266	386
Number of bonds	~ 2	~ 3

Table 5.1: Experimental estimates of ΔH and ΔS for $f = 3$ and $f = 4$ systems.

An analogous study was parallely done on the $f = 4$ system. The results of both analyses are reported in Table 5.1.
Thus, the analysis of the activated dynamics clearly indicates that as critical fluctuations start to develop, ergodicity is achieved via the breaking of the bonds between nanostars.
Local disruptions of bonds may enable the readjustment of the network of bonded structures either through nanostars evaporating away from the network and reconnecting elsewhere or through the rearrangements of network portions which are made flexible by the opening of bonds. The kinetics of this process is limited by the rate of unbinding events and it is thus slower than the free diffusion of the structures, being the lifetime of short-paired oligonucleotides easily spanning into the millisecond regime.
Thus, the analysis of the activated slowing down consistently indicates that to achieve ergodicity, the system undergoes readjustments that involve the breaking of a number of bonds which is lower than the particle valence. This notion makes good physical sense because breaking events take place more probably where the network is weakest, and less probably involve the disconnection of fully bonded nanostars.
Therefore, as observed, the characteristic time of the slow process, which is closely associated to the dynamics of critical density fluctuations of DNA nanostars, decay with a T-dependence that shows no sign of criticality as the critical point is approached.
We interpret the dominance of the activated dynamics over the conventional slowing down as a consequence of the long lifetime of the bonds between DNA structures, which is larger than the time necessary for free structures to diffuse over distances comparable to ξ. In this conditions, the decay of density correlations hinges on the restructuring of the large clusters and it is thus determined by the bond lifetime.
The critical slowing down in this system is thus confined in a temperature interval around T_c, where the collective diffusional time across ξ becomes larger than the activated bond rupture. Simple estimates indicate that such interval is too narrow to be experimentally accessed with our instrumentation (refer to [114] for further insigths).
The breakdown of dynamic universality here observed has strong analogies with the behaviour of polymeric solutions in the proximity of their critical demixing point: upon approaching the critical point, such systems feature a double relaxation and follow an unconventional critical dynamics [118, 119].
In these systems, as in ours, the dynamic behaviour is modified because of the presence of slow microscopic mechanical relaxations that overshadow the collective dynamics.

Such anomalous kinetic behaviour may extend in a large range of temperatures, including temperatures close to the critical point where the critical behaviour is typically expected, while the cross-over to the conventional slowing down is pushed to temperatures so close to T_c to be practically undetectable.

5.3.3 *T*-dependence of the other fitting parameters

Once clarified the behaviour the characteristic times associated to the fast and to slow relaxation processes of the correlation functions, it is worth to investigate the temperature dependence of the other fitting parameters.
Specifically, in the following, we discuss the behaviour of the decay amplitudes and of the stretching exponents associated to both the slow and to the fast processes of the decorrelation.

Amplitudes of the decorrelating processes

Fig. 5.10 shows the temperature dependence of the decay amplitudes associated to the fast and to the slow correlating process of decorrelation.
As it can be seen, upon lowering the temperature, the two parameters shows consistently opposite trends: while the amplitude of the slow relaxation increases up to approximately 0.9, the amplitude associated to the fast one decreases till around 0.1.
Clearly, such amplitudes are related to the importance of the corresponding relaxation processes: from the observed behaviour we can thus confirm our interpretation, already evident from the correlation functions, that at sufficiently low temperatures, the dominant process of decorrelation is the one associated to the slow relaxation.

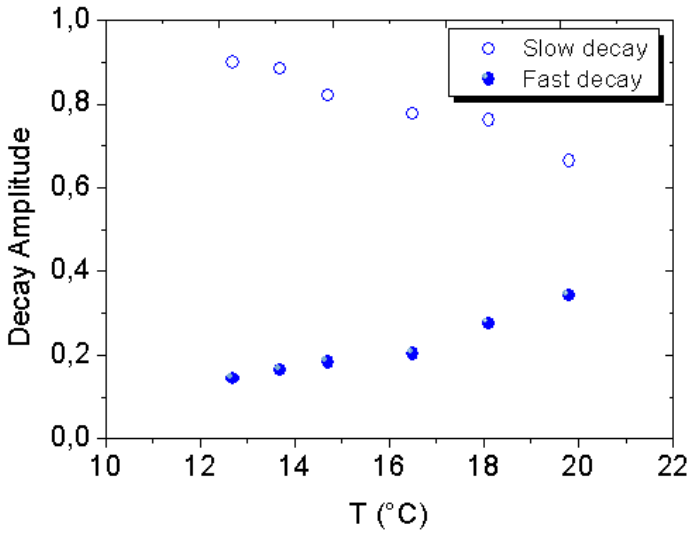

Figure 5.10: T-dependence of the amplitude for the fast and for the slow relaxation process.

Stretching exponents

It also interesting to investigate the temperature dependence of the stretching exponents β_s and β_f associated respectively to the slow and fast relaxation processes of the field correlation functions.
As it can be seen from Fig. 5.11, even in this case, we can observe a markedly different behaviour of the exponents associated to the two decay processes.
Specifically, as the temperature is gradually lowered, β_f progressively decreases from around 0.75 to a value of approximately 0.6, on approaching the critical temperature.
At the same time, β_s exhibits a moderate increase from around 0.75 to approximately 0.85.
Interestingly, we can interpret the decreasing of the stretching exponent associated to the fast relaxation as an evidence of an increasing polydispersity in sizes in the isotropic ergodic phase: indeed, on approaching the critical point, we expect that progressively larger clusters of bonded DNA nanoconstructs form on gradually cooling down the system to low temperatures.

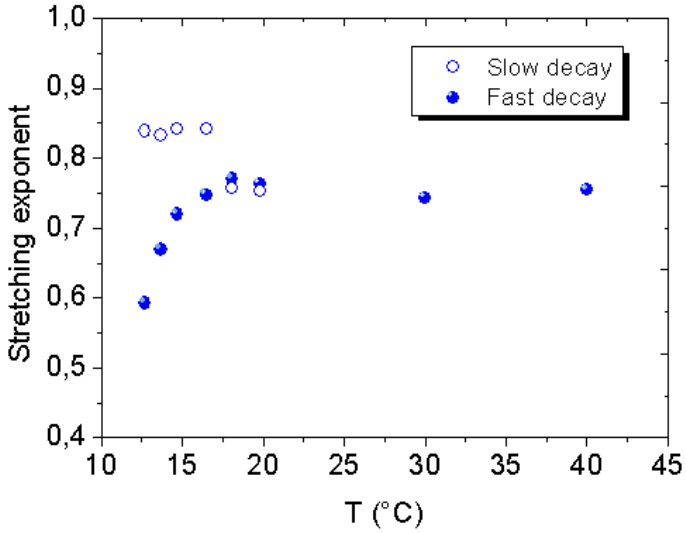

Figure 5.11: T-dependence of the stretching exponents for the fast and for the slow relaxation process.

Chapter 6

Salt effects on the nanostar dynamics

In this chapter, we present a study of the ionic strength effect on the gelation process of $f = 3$ nanostars.
The phase diagram reported in the previous chapter shows that the range of DNA concentrations where phase separation takes place is rather limited and decreases on going from $f = 4$ to $f = 3$. Since, as discussed, the concentrations of the dense phase are rather low, our solutions of DNA nanostars offer the promising chance of experimentally investigating the region of the phase diagram where equilibrium gelation should occur. Indeed, as explained in Sec. 1.1.4, when phase separation is not intervening, the gel state can be reached continuously from an ergodic phase through a series of equilibrium states, always allowing an equilibration time (longer than the bond lifetime) for the system to rearrange itself. Hence, through a careful equilibration procedure down to very low temperatures, almost-ideal gel states might become experimentally accessible.
It is known that the ionic-strength affects the binding-unbinding equilibrium of the DNA strands, by modifying the bonding free energy. Indeed, DNA strands are charged polymers and, if the terminal binding sequence would be missing, would repeal each other. Such repulsive interaction is progressively screened by the addition of salt, resulting in a more favorable binding condition. Indeed, as discussed, the melting transition of DNA strands is affected by the ionic strength in a predictable way [62, 64]. The ability to modulate the melting temperature of the overhangs with salt offers the possibility to investigate the role of the bond lifetime (which as we have seen is sensitive to temperature) on the behaviour of the correlation functions. Specifically we wanted to clarify whether the ionic strength can have an effective part on the rupture of the sticky bonds, thus allowing for the possibility of finely tuning their lifetime. We have thus performed a series of DLS experiments on $f = 3$ systems at high concentrations (i.e. at DNA densities which are outside the gas-liquid coexistence region) with the specific aim of directly investigating the dynamics of equilibrium gels. Such measurements were carried out on samples with different salt concentrations in order to experimentally evaluate the effects of the ionic strength on the dynamic behaviour of the system. The results of such investigations are summarized in the this chapter, reporting an overview on the dynamics of equilibrium gels in different ionic strength conditions.

6.1 Behaviour of $f = 3$ nanostars in the dense region

In the previous chapter we focussed on the dynamic behaviour of the $f = 3$ system on approaching the critical point. In that case, all the DLS measurements were performed at DNA concentrations which were inside the gas-liquid coexistence region, where at sufficiently low temperatures we expected phase separation. Here, instead, we address the problem of equilibrium gelation, by exploring the region of the phase diagram which is outside the phase boundary. Indeed, according to the topological phase diagram reported in Fig. 1.5, the equilibrium gel state can be reached continuously from the ergodic phase only in the region of the phase diagram where phase separation does not intervene. In order to characterize the dynamics of the equilibrium gel state, samples were prepared at a sufficiently high DNA concentration, where the system should not be subject to phase separation anymore. Specifically, on the basis of the experimental phase-diagram discussed in the previous chapter, we choose a DNA concentration value, $c_{DNA} = 9\,mg/ml$ (dashed line in Fig. 6.1), which was a good compromise between the necessity to work outside the phase boundary and the impossibility of preparing too dense samples due to the high viscosity of ds-DNA. To obtain a complete characterization of the system, encompassing the effects of the ionic strength on the dynamics, we investigated via DLS the behaviour of $f = 3$ nanostars at various salt concentrations. In particular, we prepared four samples having the same DNA concentration $c_{DNA} = 9\,mg/ml$ and gradually increasing ionic strength, i.e. 50, 70, 100, 150 mM NaCl (assuming again that each phosphate dissociates one cation).

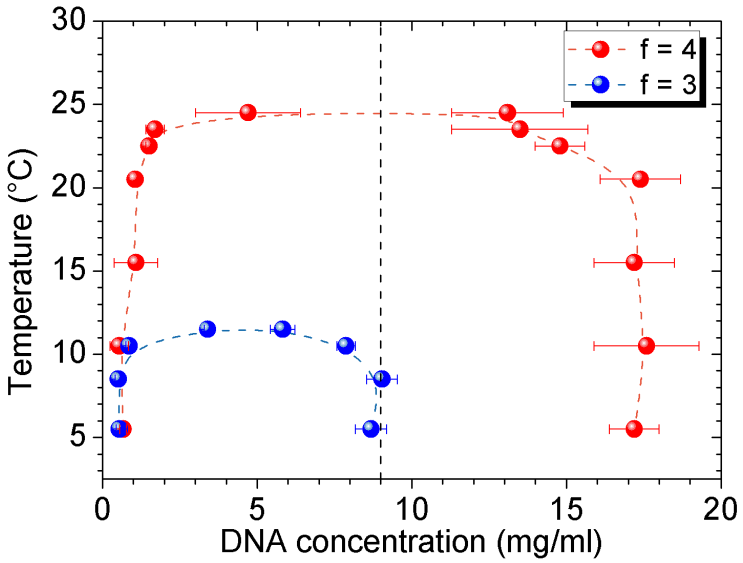

Figure 6.1: Experimental phase diagram for $f = 3$ and $f = 4$ DNA nanostars. The black dashed line indicates the working DNA concentration (outside the phase boundary for $f = 3$).

6.1.1 Static Behaviour

In order to compare the static behaviour of DNA samples at different salt concentrations, we investigated their scattering intensities as a function of the temperature. Specifically, for each sample, we performed a systematic cooling ramp: after equilibrating the solution at 40°C for 2 hours, we slowly cooled down the system in steps to the lowest possible temperature (water condensation on the walls of the optical chamber prevented measurements at temperatures lower than 7°C).
Data collected at 90° for the different samples are reported in Fig. 6.2.
As it can be seen, samples at 50, 70, 100 mM NaCl exhibit a similar behaviour, characterized by a very mild intensity growth on approaching lower and lower temperatures. On the contrary, the sample at 150mM NaCl shows a marked increase in the scattering intensity as the temperature is cooled down, somehow reminiscent of the previously observed divergence in critical samples. This anomalous behaviour clearly suggests that, even at such a high DNA concentration, the system with the higher ionic strength feels the increase of compressibility associated to the near-by phase-separation.
Indeed, it is worth to remember that the experimental phase diagram reported in Fig. 6.1 refers to samples having a resulting ionic strength of 50mM NaCl. It is rather reasonable that a change in the ionic strength of the medium might affect the phase diagram, implying modifications of the phase boundary. In fact, besides shifting all the melting temperatures (and consequently even the critical ones) to higher values,

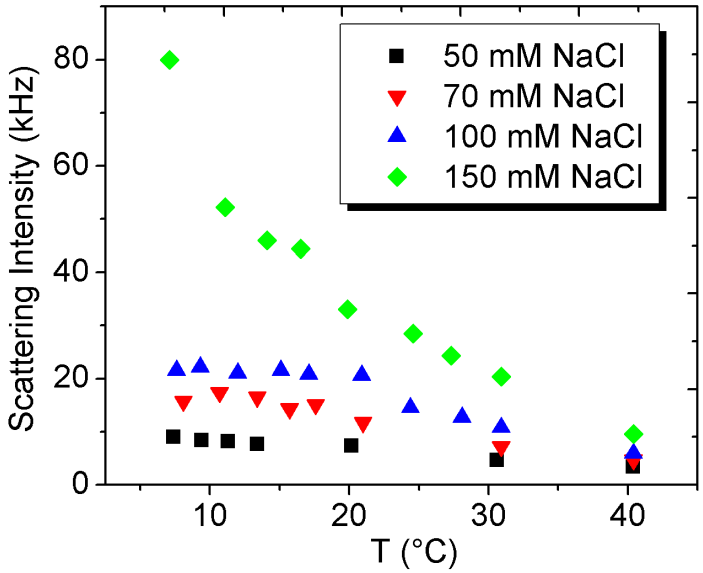

Figure 6.2: T-dependence of the scattering intensities collected at 90° for $f = 3$ nanostars in different ionic strength conditions.

increasing the ionic strength of the solutions may also imply an increase in both the critical densities and in the density of the coexisting liquid phase. Indeed, as already mentioned, adding salt results in an effective screening of the negative charges of the DNA phosphate groups, which in turn reduces the electrostatic repulsion between the double helical arms of the nanostars, enhancing the structure flexibility. This may probably imply a more compact conformation of the nanostars at high salt concentrations which can be seen as an effective shrinking of their sizes. As a consequence, varying the ionic strength of the systems effectively affects the phase diagram, involving changes in both critical temperatures and critical densities.
The observed behaviour of the scattering intensity is consistent with this scenario. Since the investigated range of salt concentrations is rather limited, we only have slightly modifications of the instability region and samples at 50, 70, 100 mM NaCl result all located outside the phase boundary where they do not undergo phase separation.
Anyhow, the effects of the salt are evident in the sample with the higher ionic strength which, despite being prepared at the same DNA concentration as the others, falls close (and perhaps even inside) the phase boundary. Moreover, the T-dependence of the scattering intensity at different salt concentrations confirms the role played by the ionic strength in shifting the melting temperatures of the systems. Indeed, by comparing the intensities scattered by the different samples at the same temperature value, one can easily observe how the scattering intensity progressively increases on increasing the ionic strength (i.e. at the same T, the sample with the higher ionic strength scatters more light than the others do). In fact, at the same T value, the number of bonded overhangs it is supposed to be larger in samples with higher ionic strength (since, as shown by the UV measurements discussed in chapter 4, the melting temperature of the sticky ends is shifted upward on increasing the salt concentration), thus giving rise to large clusters of bonded nanostars. Besides giving important indications on how the system behaviour is affected by the ionic strength, the scattering intensity can be further exploited to investigate the approach to the equilibrium gel states. Indeed, neglecting the sample at 150 mM NaCl which is affected by the phase-separation, a closer look at the T-dependence of the scattering intensity for the other samples reveals a very interesting behaviour.
Specifically, as expected for systems approaching the gel state from the ergodic phase, the intensity scattered by the solutions initially increases as the system is slowly cooled down and it later saturates, stabilizing on a constant value at sufficiently low temperatures (Fig. 6.3). The achievement of the plateau nicely signals the approach to the equilibrium "ideal" gel state [55]: a further decrease in the temperature does not affect the scattered intensity anymore. From a microscopic point of view, the independence of the scattered intensity from temperature is an indication that the structure of the system does not evolve any longer. The system has possibly reached the fully bonded configuration, in which all trimers are part of the same spanning infinite cluster.
Fig. 6.3 suggests that, consistently with the previously discussed behaviour, samples with higher ionic strength reach the gel state before the others (i.e. at higher temperatures). For instance, while the sample having 50 mM NaCl ionic strength shows a mild

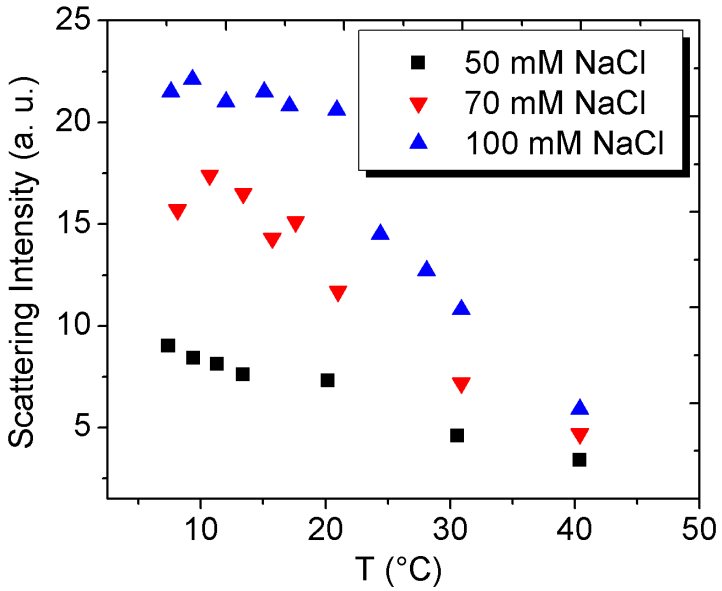

Figure 6.3: T-dependence of the scattering intensities collected at 90° for $f = 3$ nanostars in different ionic strength conditions.

intensity growth even at very low temperatures (below 10°C), which barely stabilizes on a plateau value, the sample at 100 mM NaCl exhibits a nearly constant scattering intensity for all the investigated temperatures below 21°C, suggesting that it has already approached the arrested gel state. The progressive growth of the low-temperature scattered intensity with salt indicates that the final gel structure is sensitive to the ionic strength. Such value (related to the gel compressibility) indicate the different proximity of the sample to the close-by spinodal line, where the scattered intensity at small wavevector would diverge.

6.1.2 Dynamic Behaviour

In order to systematically characterize the dynamics of the system in the dense region, all the samples were investigated via dynamic light scattering measurements in a wide range of temperatures, roughly from 40°C to 7°C. Specifically, we performed a series of cooling ramps, starting from the high temperature ergodic phase in which nanostars are formed but weekly interacting (i.e. T = 40°C) and slowly cooled down the system in steps, always allowing an equilibration time of approximately 2 hours. In the following we discuss the families of field correlation functions relative to the samples at the four different salt concentrations. All the reported measurements were performed at a fixed scattering angle of 90°.

Field correlation functions for $f = 3$ nanostars in 50mM NaCl

Fig. 6.4 shows a set of field correlation functions for $f = 3$ structures at $c_{DNA} = 9$mg/ml in 50 mM NaCl. In strong analogy with the set of critical samples discussed in chapter 5, the high temperature curve (T = 40.4°C) exhibits a major, rather noisy, decay which gradually turns into a two-step relaxation process as the system is cooled down. As it can be seen from Fig. 6.4, for all the investigated temperature, the two step relaxation can be well fitted to the sum of two stretched exponential. Interestingly, as for the critical samples, one can clearly observe the insurgence of a plateau whose height f_q progressively increases on cooling.
Anyhow, the amplitude of the slow relaxation, i.e. f_q, results much smaller than in the critical case. Unfortunately, as already mentioned, experimental limitations due to water condensation on the glass walls of the VAT prevented the measurements at temperatures lower than 7°C. Such low temperature data would have been particularly useful to completely characterize the behaviour of f_q as a function of the temperature.

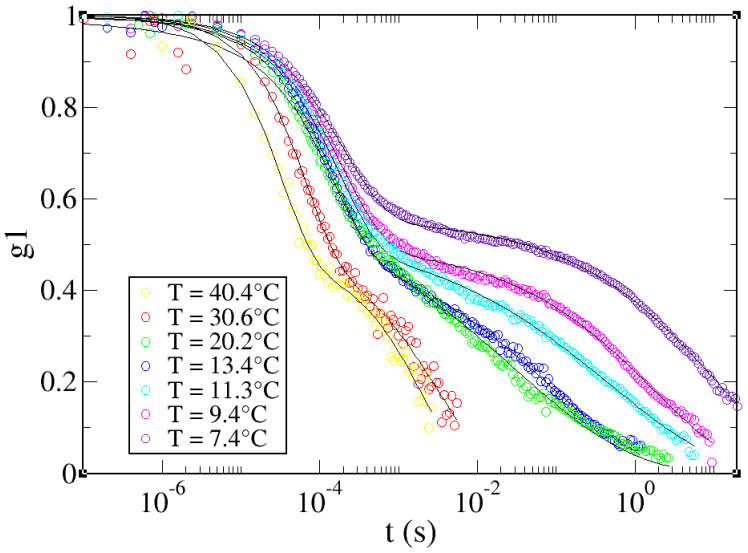

Figure 6.4: Field correlation functions for $f = 3$ nanostars ($c_{DNA} = 9\,\frac{mg}{ml}$; 50mM NaCl). Data are fitted to a sum of two stretched exponentials (lines).

Field correlation functions for $f = 3$ nanostars in 70 mM NaCl

Fig. 6.5 shows a set of field correlation functions for $f = 3$ structures at $c_{DNA} = 9$mg/ml in 70 mM NaCl. From a first glance to the curves, one can immediately note that the behaviour of the system is completely analogous to the one found in the 50mM NaCl sample. Anyhow, it is possible to observe a slight shift in the temperatures with respect to the previous case, which can be easily ascribed to the addition of salt.

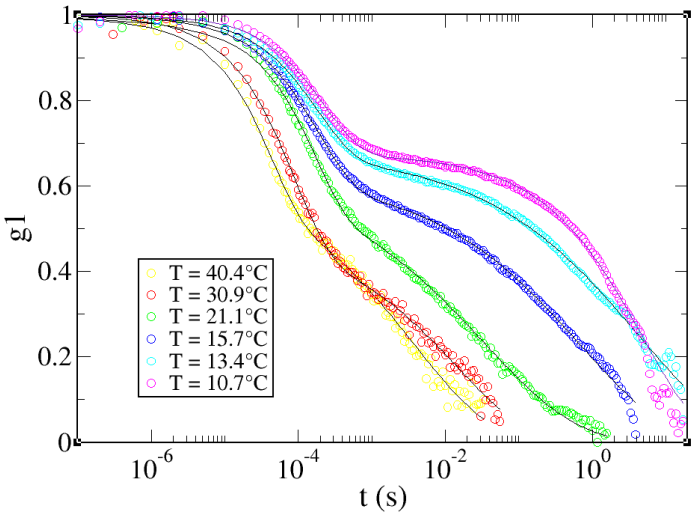

Figure 6.5: Field correlation functions for $f = 3$ nanostars ($c_{DNA} = 9\,\frac{mg}{ml}$; 70mM NaCl). Data are fitted to a sum of two stretched exponentials (lines).

Field correlation functions for $f = 3$ nanostars in 100 mM NaCl

Fig. 6.6 shows a set of field correlation functions for $f = 3$ structures at $c_{DNA} = 9$mg/ml in 100 mM NaCl. The further addition of salt nicely confirms the already observed trend. Since all the melting temperatures are shifted upward, we can now investigate the T-dependence of f_q without the need to go to very low T values.

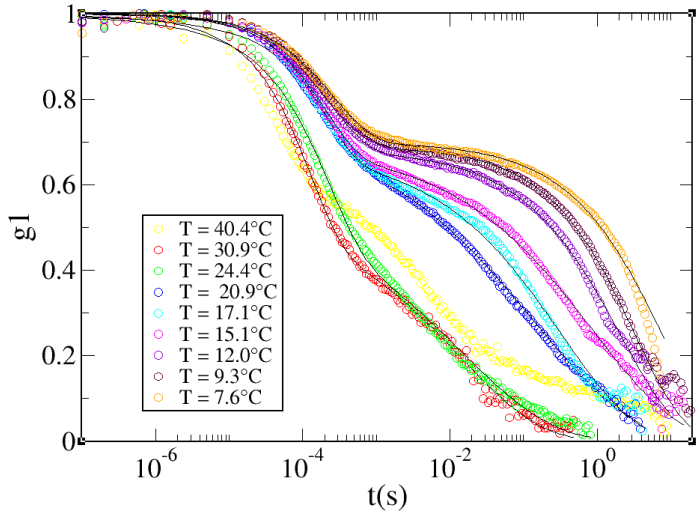

Figure 6.6: Field correlation functions for $f = 3$ nanostars ($c_{DNA} = 9\,\frac{mg}{ml}$; 100 mM NaCl). Data are fitted to a sum of two stretched exponentials (lines).

Field correlation functions for $f = 3$ nanostars in 150mM NaCl

Fig. 6.7 shows a set of field correlation functions for $f = 3$ structures at $c_{DNA} = 9$mg/ml in 150 mM NaCl.
A first evident difference with the samples at lower ionic strength is given by the amplitude of the slow relaxation, which appears much larger than in the previous cases.
It is important to remind that, according to the anomalous T-dependence of the scattered intensity, this sample should be critical. For such reason, eventual anomalies in the dynamic behaviour of this sample with respect to the others must be ascribed to its tendency to phase separate.
Nevertheless, it still gives important information on how the dynamics of the systems is affected by the ionic strength and it can be thus used for comparative analyses with the different samples.
For instance, from a qualitative comparison between the various curves at different salt concentrations, one can immediately note that correlation functions, having the same plateau height, decay to zero at shorter times in samples with higher salt concentrations with respect to the others[1].
To better characterize the differences among the various samples and to quantitatively evaluate the effects of the ionic strength on the system dynamics, we systematically analyzed the T-dependence of the various fitting parameters for the different salt concentrations.
The results of such analyses are discussed in the next section, where we give a summarizing overview of the observed trends.

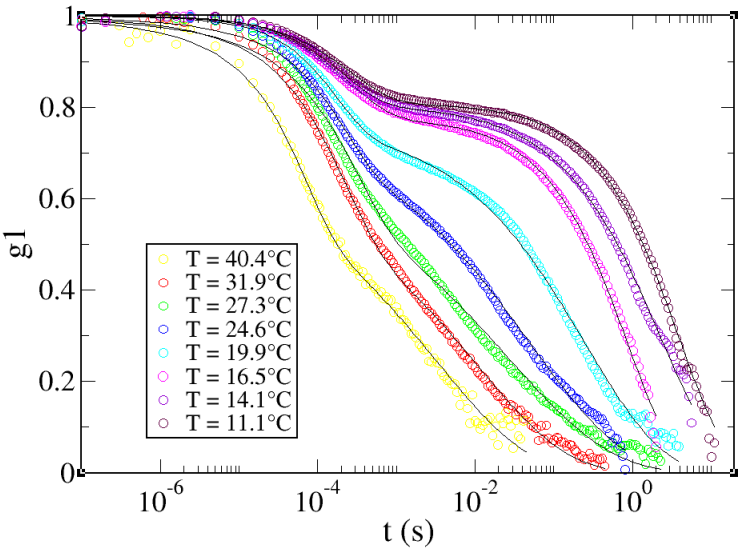

Figure 6.7: Field correlation functions for $f = 3$ nanostars ($c_{DNA} = 9\,\frac{mg}{ml}$; 150mM NaCl). Data are fitted to a sum of two stretched exponentials (lines).

[1]For a deepening on this point refer to Sec. 6.3.2.

Percolation threshold

An interesting common feature of all the investigated families of field correlation functions is represented by the appearance of a curve, at a specific temperature value, which exhibits an evident logarithmic decay in an intermediate time interval (Fig. 6.8).
A closer inspection to the each set of correlation functions reveals that such curve signals the crossover from the high temperature behaviour, characterized by freely diffusing individual structures, to the low temperature one, where the insurgence of the plateau suggests the progressive formation of a spanning network of bonded nanostars. Therefore, it is tempting to associate the temperature value Tp at which the logarithmic decay is observed provides an experimental estimate of the percolation threshold — as sampled at the experimental wavevector — for our samples. Indeed:

- when $T > T_P$ the system is in a high-temperature ergodic state, in which the DNA nanostars are well formed but not (or weekly) interacting;

- when $T < T_P$ a percolating network of bonded structures progressively forms (as the number of bonded overhangs gradually increases), leading to an arrested gel state at sufficiently low temperatures.

As a consequence, by plotting the experimental T_P values as a function of the salt concentration of our samples, it is possible to provide an estimate of the ionic strength dependence of the percolation threshold for $f = 3$ nanostars. As shown in 6.9, data suggest a nearly linear dependence of the percolation threshold on the salt concentration.

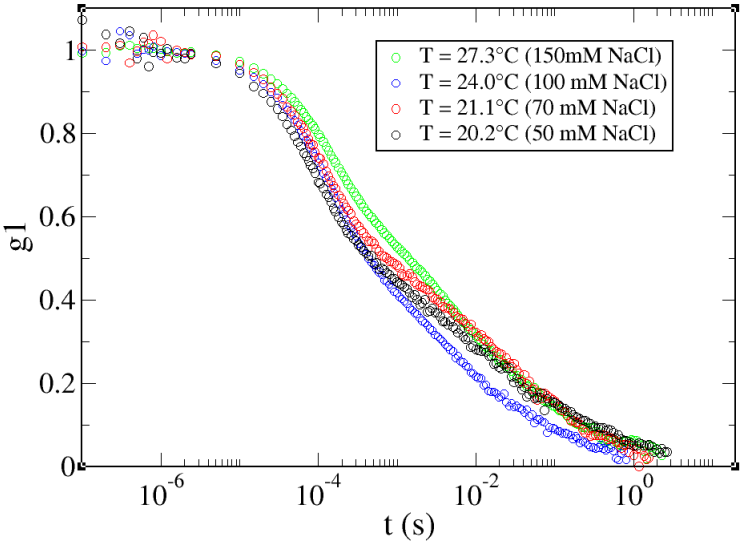

Figure 6.8: Field correlation functions for $f = 3$ nanostars, at various salt concentrations, exhibiting a nearly logarithmic decay.

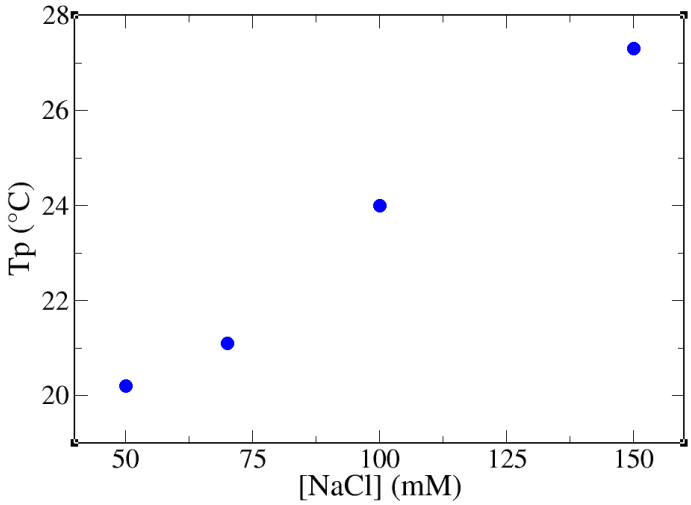

Figure 6.9: Experimental percolation threshold as a function of the ionic strength.

Furthermore, the percolation threshold is located at higher temperatures for samples having higher ionic strength, thus confirming once again the expected behaviour.
At high salt concentrations, the interactions between different overhangs starts earlier, thus shifting the formation of the spanning network (and consequently the dynamic arrest) to higher temperatures.

6.2 Ionic strength dependence of the fitting parameters

In analogy with the analysis done for the critical samples, we systematically investigated the dependence of the fitting parameters from both the temperature and the ionic strength. Specifically, we focussed on the characteristic times of the two relaxation processes, on the stretching exponents of the double stretched exponential used to fit the correlation functions and, eventually, on the amplitude of the slow relaxation, i.e. on the non-ergodicity factor of our systems.

6.2.1 Decay times

As already mentioned in the previous section, all the field correlation functions for $f = 3$ nanostars in the dense region can be well fitted to a double stretched exponential. Therefore, analogously to the critical samples, the dynamic behaviour of the system can be described by two characteristic times, one associated to the fast relaxation and the other associated to slow one.
Fig. 6.10 shows the decay times obtained for all of the investigated salt concentrations.

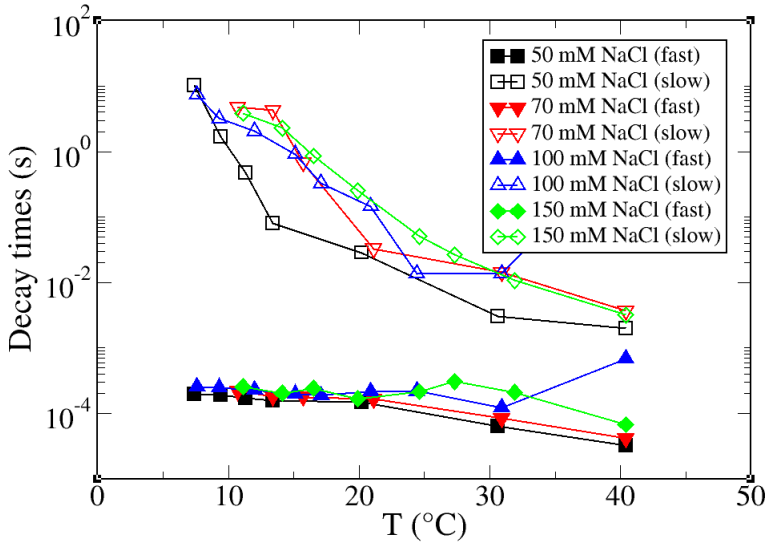

Figure 6.10: T-dependence of the decay times for the two relaxation processes at various salt concentrations (50, 70, 100, 150 mM NaCl).

As it can be seen, the characteristic times of the fast relaxation processes are nearly the same for all the investigated salt concentrations. Specifically, except for a noisy region at high temperatures, their trends do not exhibit a marked dependence from the temperature, being essentially flat at all the temperatures explored. Interestingly, such behaviour is actually very similar to the one that we would expect for the freely diffusing nanostars.
On the contrary, the characteristic times of the slow processes reveal a more interesting scenario.
Indeed, as for the critical samples, we observe that, in all the investigated samples, τ_s slows down by nearly three orders of magnitude as the temperature is lowered.
Anyhow, since the experimental data result much more noisy than in the critical case, it is difficult to state whether the ionic strength could systematically affect the slope of the growth. Nevertheless, an interesting trend emerges from the plot: for a fixed temperature value, samples having different ionic strength decay with rather different characteristic times. In particular, for a given temperature value, samples with the higher salt concentrations decay at longer times with respect to the others.
This means that, for the same temperature value, the sample with the higher salt concentration will be closer to the arrested gel state than the others. Once again, this behaviour can be explained by considering that all the characteristic temperatures of the system are moved upwards by the addition of salt.
Anyhow, considering that, in our interpretation, τ_s should be regulated by the lifetime of the duplexes that form between overhangs, a proper evaluation of whether the bond lifetime is influenced by the ionic strength can be only done by directly comparing the decay times of different correlation functions having the same f_q (refer to Sec. 6.3.2).

6.2.2 Stretching exponents

The temperature dependence of the stretching exponents for all the investigated salt concentrations is reported in Fig. 6.11.
As it can be seen, the stretching exponents for the fast relaxation are all close to 1 at high temperatures (neglecting the out of trend point relative to the 100mM NaCl sample) and they slightly decrease approaching 0.8 as the temperature is lowered.
Again, such behaviour reveals the increase in the polydispersity of the isotropic phase, caused by the gradual formation of larger and larger clusters of bonded DNA nanostars.
Since the T-dependence is nearly the same for all the investigated salt concentrations, β_f results independent from the ionic strength of the solutions.
On the contrary, the dependence on the ionic strength is evident for the stretching exponential associated to the slow relaxation. Indeed, for each salt concentration, the T-dependence of β_s is essentially the same: at high temperature, the stretching exponents are rather small, being in the range 0.2 - 0.4 for all the salt concentrations (neglecting the out of trend point at 50 mM NaCl) and their values progressively increase as the temperature of the system is lowered. Anyhow, such increase appears to be highly sensitive to the ionic strength of the solutions being rather unclear in the case of 50 mM NaCl (where at very low T, the maximum value reached by β_s is 0.4) and very well pronounced in the case of 150 mM NaCl, where β_s reaches values around 0.7 on decreasing the temperature.
As the stretching exponent gives an indication of the steepness of the relaxation process, its ionic strength dependence clearly suggests that upon decreasing the temperature, the slow decay becomes significantly steeper for samples at high salt concentrations

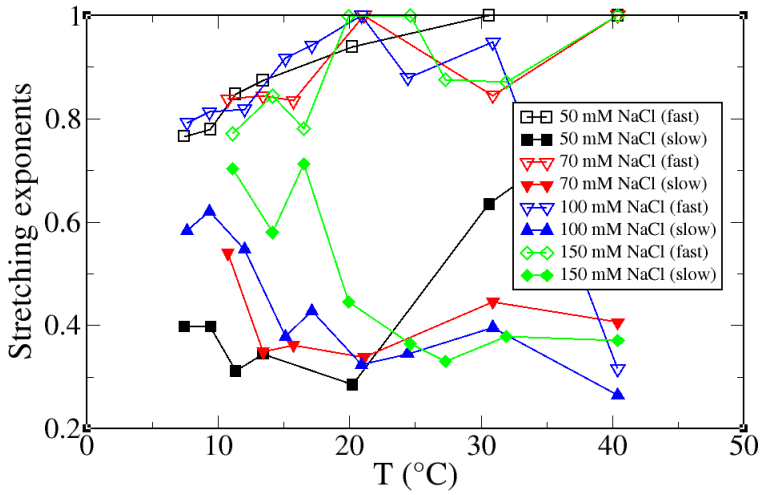

Figure 6.11: T-dependence of the stretching exponents associated to the two relaxation processes at various salt concentrations (50, 70, 100, 150 mM NaCl).

with respect to the others.
The increase of β_s on cooling reflects an homogenization of the slow decay process, which could have a microscopic interpretation in the completion of the aggregation process on cooling associated to the approach toward the equilibrium gel.
It is interesting to observe also that a rise in the stretching exponent associated to a progressive slowing down of the dynamics has been observed in strong glass network formers, suggesting perhaps that network molecular glass formers should be considered more as gel-forming liquids (despite the different bond-breaking time-scale) than as excluded volume caged glasses.

6.2.3 Non ergodicity factor

An important parameter that we studied as a function of the temperature for different salt concentrations is given by the amplitude of the slow relaxation process, i.e. what we called, in analogy to glass physics, the non-ergodicity factor.
Indeed, as already mentioned, at sufficiently low temperatures, the dominant process of decorrelation in our DNA nanostar systems is the one associated to the slow relaxation of the correlation functions.
For such reason we focussed on its temperature dependence, investigating how it is affected by the ionic strength. The results of such investigation are reported in Fig.6.12.
At all the investigated salt concentrations, the systems exhibits a similar behaviour, characterized by a progressive growth of f_q as T is lowered. Such trend is not well-defined in the 50mM NaCl sample, which shows a rather noisy temperature behaviour

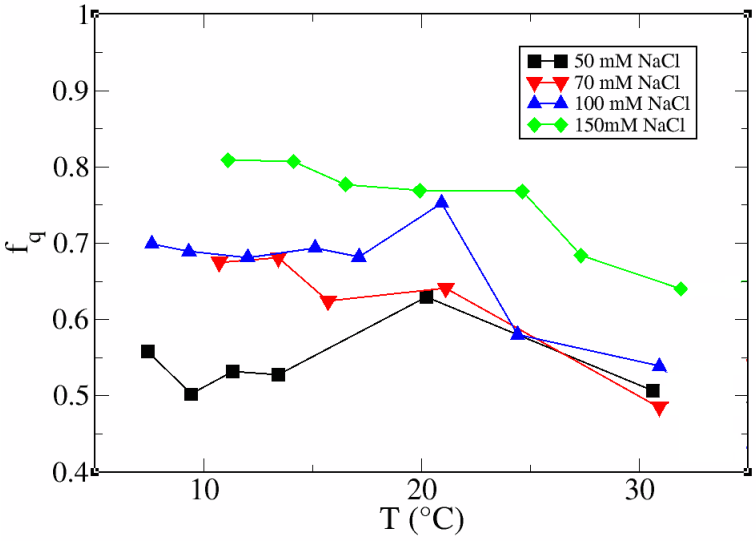

Figure 6.12: T-dependence of the experimental non-ergodicity factor at various salt concentrations (50, 70, 100, 150 mM NaCl).

(moreover, for such sample, we can observe the presence of a markedly out of trend point at 20.2°C probably due to the effects on the fitting process of irregularities in the correlation function on crossing the percolation threshold).
Interestingly, at sufficiently low temperatures, the f_q values for the samples having 70mM and 100mM NaCl ionic strength superimpose.
Unfortunately, due to the already mentioned experimental limitations, we could not explore the behaviour of f_q at $T < 7$°C. Such information would have been particularly useful for the sample having 50mM NaCl ionic strength: indeed, from the observed experimental scenario we cannot exclude that at low enough temperatures, f_q associated to this sample would also reach higher values, possibly superimposing to the other observed trends.
A separate discussion is instead necessary for the 150mM NaCl sample which present markedly higher f_q values, analogous to the ones observed in critical samples, thus suggesting once again its likely tendency to phase separate.

6.3 Comparative analysis as a function of the ionic strength

In the first section of this chapter we have separately shown different sets of correlation functions relative to samples having increasing ionic strength.
Anyhow, a much more effective way to visualize the effects that the addition of salt has on the dynamics of the $f = 3$ system can be achieved by directly comparing the experimental curves obtained at the different salt concentrations.
In line with this idea, we performed a comparative analysis of the data relative to the various salt concentrations, following two different approaches:

- in the first one, we simultaneously compared all the field autocorrelation functions from different data sets taken at the same temperature value (or in a narrow interval of temperatures around it);
- in the second one, we simultaneously compared all the field autocorrelation functions from different data sets having the same plateau height (i.e. the same f_q).

In the following, we give a brief overview on the main results of such analysis.

6.3.1 Field correlation functions at the same temperature

Field correlation functions relative to the samples at the four different salt concentrations were visually compared by plotting together curves taken at nearly the same temperature. Specifically, such analysis was done around four temperature values:

- $\mathbf{T \sim 30}$**°C**: Due to the low signal/noise ratio at 40°C, the obtained field correlation functions resulted very noisy and the comparison among curves taken at such temperature became meaningless. Therefore, to properly evaluate the effect of the ionic strength on the high-temperature dynamics of the system, we compared correlation functions taken at around 30°C (Fig. 6.13);
- $\mathbf{T \sim 20}$**°C**: As already seen, for the majority of the samples, the percolation threshold is located around this temperature. It may be thus worth to investigate how the different systems behave in the proximity of such value (Fig. 6.14);
- $\mathbf{T \sim 13°C}$: At such temperature value, the two step relaxation of the correlation functions is well defined for all the investigated salt concentrations. Therefore, it is interesting to compare the different curves to observe how the amplitudes of the decorrelation processes are affected by the ionic strength. (Fig. 6.15);
- $\mathbf{T \sim 10}$**°C**: At such low temperature value, all the correlation functions have already developed a marked plateau: the comparative analysis at approximately 10°C is thus useful to clarify the behaviour of f_q as a function of the ionic strength (Fig. 6.16).

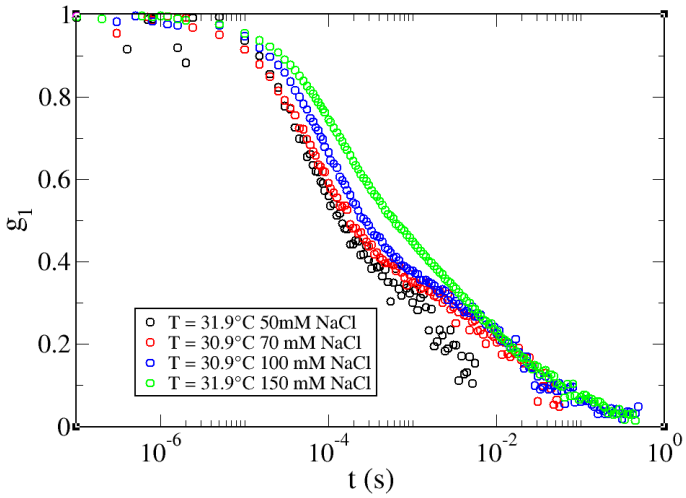

Figure 6.13: Field correlation functions for $f = 3$ nanostars at $T \sim 30°C$, in various salt concentrations (50, 70, 100, 150 mM NaCl).

From the comparison of the correlation functions taken at approximately 30°C, a well defined trend with the ionic strength is clearly observable. Specifically, the curves appear to be progressively shifted towards longer correlation times as the ionic strength of the sample is enhanced, thus confirming once again the role played by the addition of salt in shifting upwards all the characteristic temperatures of the system. Consistently, the analogous comparison at 20°C corroborates such scenario: while samples at the lower salt concentration (50, 70 mM NaCl) exhibit the logarithmic decay of the correla-

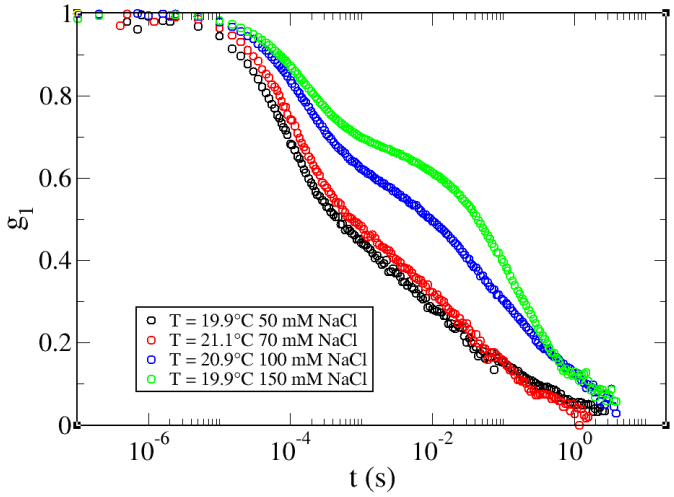

Figure 6.14: Field correlation functions for $f = 3$ nanostars at $T \sim 20°C$, in various salt concentrations (50, 70, 100, 150 mM NaCl).

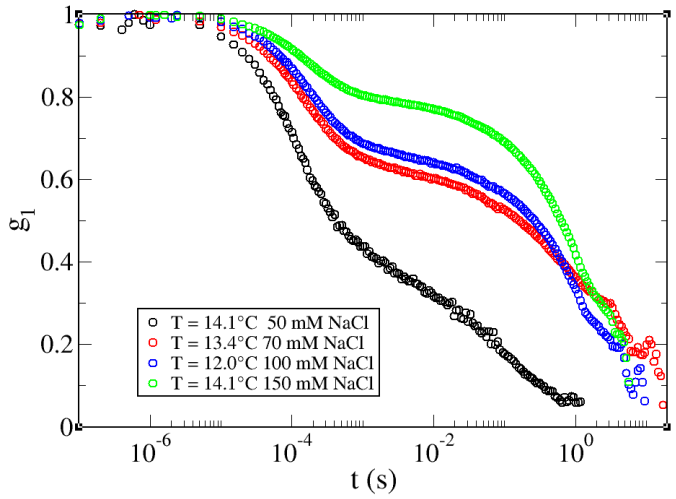

Figure 6.15: Field correlation functions for $f = 3$ nanostars at $T \sim 13°C$, in various salt concentrations (50, 70, 100, 150 mM NaCl).

tion functions, which suggests the crossing of the percolation threshold, samples having higher ionic strength have already developed a sort of plateau, signaling the imminent approach to the gel state. The same trend is analogously observed at 13°C and 10°C, where the height of the plateau clearly suggests that, at the same temperature, samples with the higher ionic strength have a larger number of bonded nano-structures, due to the shift in the melting temperatures of the overhangs caused by the addition of salt.

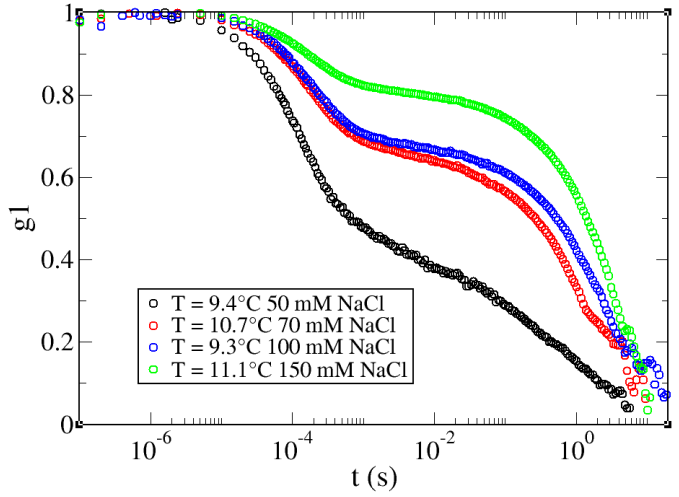

Figure 6.16: Field correlation functions for $f = 3$ nanostars at $T \sim 10°C$, in various salt concentrations (50, 70, 100, 150 mM NaCl).

6.3.2 Field correlation functions having the same f_q

Field correlation functions having the same plateau height (relative to samples at different salt concentrations) were compared in order to understand whether the ionic strength could somehow affects the lifetime of the sticky bonds.
Indeed, as discussed in chapter 5, the decay time associated to the slow decorrelation process should be regulated by the lifetime of the sticky bonds which form between different nanostars. If such interpretation is correct, then a proper way to evaluate the effects of the ionic strength on the bond lifetime is to consider only the correlation functions which exhibit the same f_q and to systematically compare the τ_s values associated to such decays. The eventual ionic strength dependence of these decay times should clarify whether the bond lifetime can be tuned by changing the salt concentration.
Such method for comparatively analyzing the curves is particularly robust, since it is completely independent from the temperature (i.e. we do not need to pay attention to the melting temperature shifts caused by the variations in the ionic strength).
Fig. 6.17 shows a comparison between two field correlation functions relative to the samples having 50 mM and 70 mM ionic strength with comparable non ergodicity factors. As it can be seen, the sample with the higher ionic strength decays to zero at much shorter times than the other one. Therefore, if our interpretation of τ_s is correct, this behaviour is clearly suggesting that modulation of the ionic strength can be a powerful handle for tuning the bond-lifetime between different nanostars and estimate its effect on the decay of the correlation functions at comparable network structure. We use the word "comparable" to remind that salt also modulates the location of the phase-coexistence and of the compressibility of the gel. For a proper comparison, one

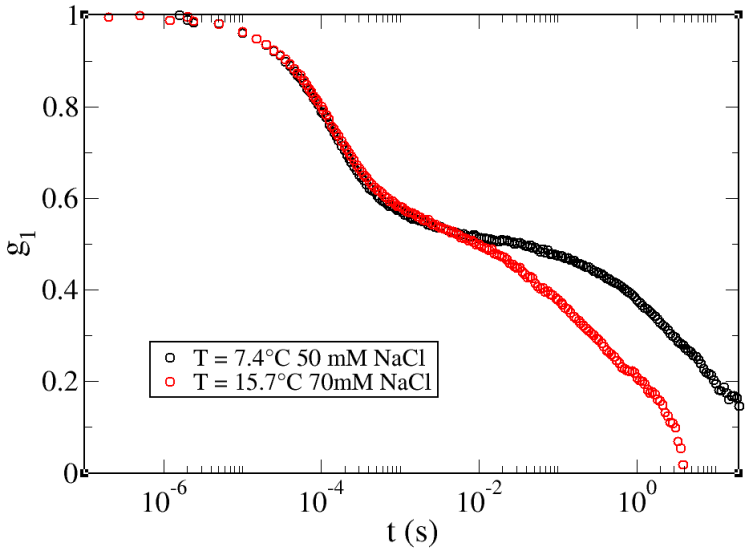

Figure 6.17: Field correlation functions for $f = 3$ nanostars having $f_q \sim 0.55$, at two different salt concentrations (50, 70 mM NaCl).

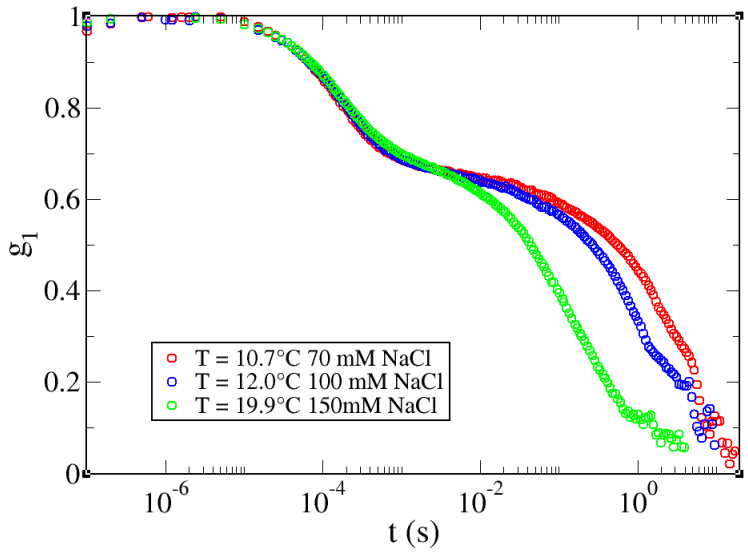

Figure 6.18: Field correlation functions for $f = 3$ nanostars having $f_q \sim 0.65$, at three different salt concentrations (70, 100, 150 mM NaCl).

should perhaps modulate the sample overall DNA concentration.
A further example of correlation functions with different ionic strength but comparable f_q is reported in 6.18, where three experimental curves having nearly the same f_q (and respectively relative to the 70, 100 and 150 mM NaCl samples) are plotted simultaneously.
The observed trend confirms the expected dependence on the salt concentration, thus supporting our interpretation: the gradual addition of salt reduces the lifetime of the sticky bonds, progressively anticipating the decay of the density correlation functions. Indeed, as previously seen, the decay of density correlations hinges on the restructuring of the network and it is thus determined by the bond lifetime.
Therefore, such results nicely show that it is possible to tune the bond lifetime, and hence the dynamic behaviour of the system, by simply varying the ionic strength of the medium.

6.4 Experimental evidence of equilibrium gelation

As a conclusive consideration, it is worth to remark the importance of the present study in the experimental investigation of equilibrium gelation. In fact, via dynamic light scattering measurements, we deeply explored the dynamics of equilibrium gels, thus confirming that such states can be effectively reached from the high-temperature ergodic phase through a series of equilibrium states.
For instance, a beautiful example of equilibrium gelation is shown by the dynamic behaviour of the sample having 100mM NaCl ionic strength.

Indeed, as already discussed, the salt concentration of this sample is sufficiently high to shift the approach to the gel state at temperatures which are easily experimental accessible and, at the same time, sufficiently low to avoid phase separation.
Therefore, performing a temperature ramp from high temperature, allowing the system to equilibrate for long enough time at each cooling step (nearly 2 hours), provided the unprecedented opportunity to explore the dynamics of the system which leads to the formation of the equilibrium gel.
A summarizing view of the results of such investigation are reported in Fig. 6.19.

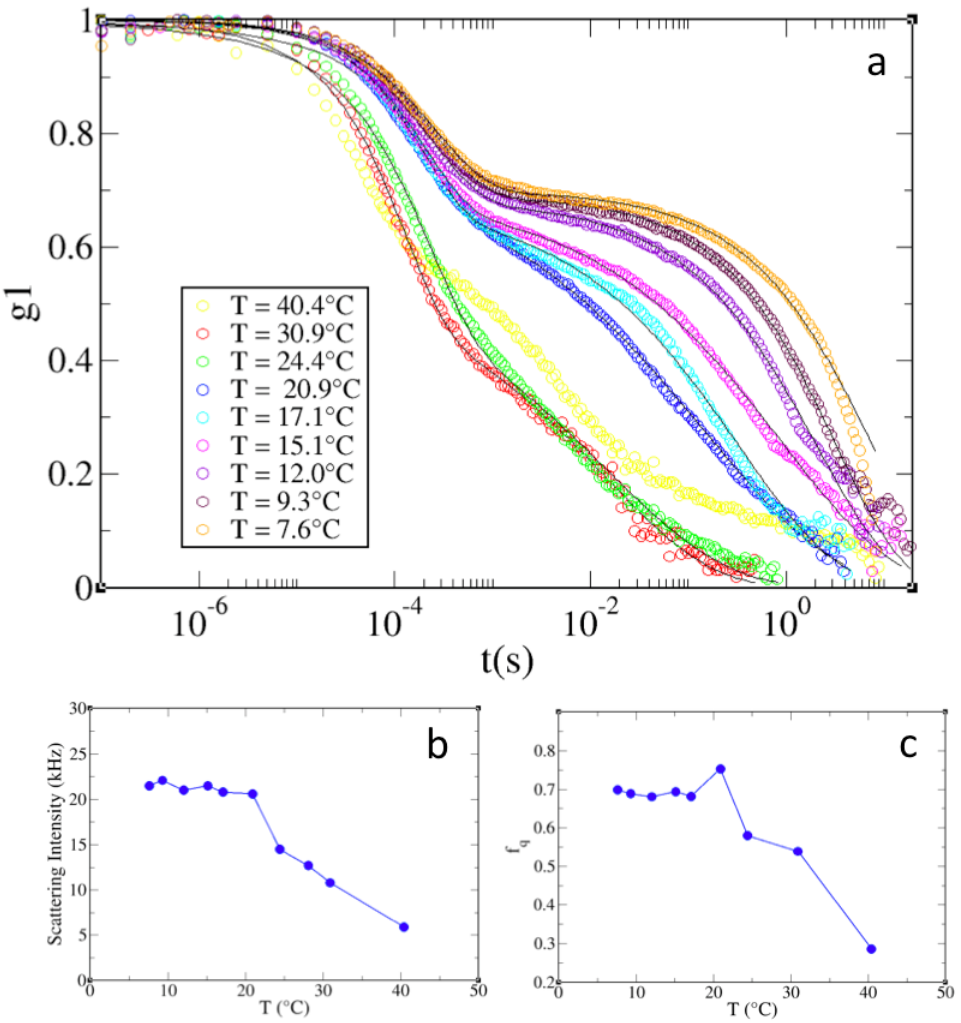

Figure 6.19: Equilibrium gelation in a sample of $f = 3$ nanostars ($c_{DNA} = 9\,\frac{mg}{ml}$; 100 mM NaCl): a) Field correlation functions detected at 90°. b) T-dependence of the scattering intensity detected at 90°. c) T-dependence of f_q.

As it can be seen, the field autocorrelation functions together with the temperature-

dependence of scattering intensity and of the non-ergodicity factor, consistently indicate the imminent approach to the gel state (at temperatures lower than 15°C).
Indeed, on approaching the gel state, it is possible to observe a concomitant change in all the observed trends:

- the intensity autocorrelation functions do not evolve anymore, or they only show minor variations, on further lowering the temperature (in particular, the amplitude of the slow decorrelating process does not change anymore with T);
- the scattering intensity stops growing, saturating on a specific value;
- the non-ergodicity factor stabilizes on a temperature-indipendent value (consistently with the observed behaviour of the field correlation functions).

Conclusions

"The important thing is
not to stop questioning"

Albert Einstein

In the present thesis we addressed the issue of experimentally determining the phase diagram of limited-valence particles, with the specific aim of testing recent theoretical predictions on the phase behaviour of reduced valence systems.
In order to do this, we realized self-assembling DNA nanostars having a well defined valence ($f = 3$) and systematically investigated their collective behaviour in a wide range of temperatures and densities.
Interestingly, we found that solutions of such particles undergo phase separation.
From a comparative analysis with the results on $f = 4$ nanostar solutions, we discovered that, as expected, the critical parameters (temperature and nanostar concentration) crucially depend on the valence, causing a significant shrinking of the region of thermodynamic instability when the valence is reduced.
Thus, besides confirming the theoretical predictions on the key role played by the valence on the phase behaviour of limited-valence system, our result also represent, to the best of our knowledge, the first experimental detection of a critical phenomenon in DNA solutions.
Moreover, we also characterized the critical dynamics of the system, finding a surprising anomalous behaviour.
Indeed, upon approaching the critical point from high temperature, the scattered light intensity diverges with a power-law, whereas the field autocorrelation function shows a plateau followed by a slow relaxation process.
Interestingly, the slow relaxation time exhibits an Arrhenius behaviour with no signs of criticality, demonstrating a novel scenario where the critical slowing down of the concentration fluctuations is enslaved to the large lifetime of the sticky bonds.
Furthermore, we performed a systematic investigation of equilibrium gelation processes. Indeed, being the concentrations of the dense phase at coexistence rather low, our solutions of DNA nanostars offer the promising chance of experimentally investigating the region of the phase diagram where equilibrium gelation should take place. Indeed, when phase separation is not intervening, the gel state can be reached continuously from an ergodic phase through a series of equilibrium states, always allowing an equilibration time (longer than the bond lifetime) for the system to rearrange itself. Hence, through a

careful equilibration procedure down to very low temperatures, we showed that almost-ideal gel states can become experimentally accessible.
Eventually, we also investigated the ionic strength effect on the gelation process of $f = 3$ nanostars. Indeed, we wanted to clarify whether the ionic strength could have an effective part on the rupture of the bonds between nanostars, thus allowing for the possibility of finely tuning their lifetime.
Experimental data nicely confirmed the expected dependence on the salt concentration: the gradual addition of salt reduces the lifetime of the sticky bonds, progressively anticipating the decay of the density correlation functions. Therefore, such data clearly showed that it is possible to tune the bond lifetime, and hence the dynamic behaviour of the system, by simply varying the ionic strength of the medium.
Ultimately, the total set of experimental results here reported nicely demonstrate that DNA nanostars are powerful particles for investigating the phase behaviour of systems in which it is possible to tune binding selectivity (via the DNA sequence), strength of interaction (via the DNA length) and valence.
Key in this application is the strong temperature dependence of the DNA duplex binding strength, which enables exploring a wide range of bond energies and bond lifetimes, as no other model system does.
We foresee that a large variety of issues in statistical physics can be experimentally addressed through the use of DNA supermolecules, including re-entrant behaviours induced by competitive interactions [14, 15, 120] and higher order network-network critical points [86].
Notably, a topic that could be worth to investigate using our limited-valence DNA nanostars is the gelling by heating scenario predicted by Roldán-Vargas et al. [120].
Indeed, in their work, the authors introduce a simple model, consisting of a binary mixture of limited-valence particles, in which the designed competition between entropy and potential energy causes the system to show a re-entrant behaviour, providing the remarkable possibility of forming a gel upon heating. In fact, thanks to the specific nature of the particle interactions (in particular, the number and geometry of the patches as well as their interaction energies), the system behaves as a fluid both at high and at low temperatures, whereas it forms a thermo-reversible gel at intermediate temperatures.
Therefore, we plan to use our solutions of DNA nanostars with limited-valence to experimentally mimic this predicted behaviour by simply adding to them specific DNA single strands, designed on purpose to generate the desired competitive interactions.
Eventually, another open issue which could be experimentally investigated by using our limited-valence DNA nanostars is the outstanding possibility of obtaining liquid phases more stable than crystal ones at low temperature, a scenario only achievable in reduced-valence systems, as recently predicted by F. Smallenburg and F. Sciortino [121].

Bibliography

[1] Watson, J. D., and F. H. C. Crick. "A structure for deoxyribose nucleic acid." Nature 171 (1953).

[2] Seeman, Nadrian C. "DNA in a material world." Nature 421.6921 (2003): 427-431.

[3] Condon, Anne. "Designed DNA molecules: principles and applications of molecular nanotechnology." Nature Reviews Genetics 7.7 (2006): 565-575.

[4] Seeman, Nadrian C. "Nucleic acid junctions and lattices." Journal of theoretical biology 99.2 (1982): 237-247.

[5] Bellini, Tommaso, Roberto Cerbino, and Giuliano Zanchetta. "DNA-Based soft phases." Liquid Crystals. Springer Berlin Heidelberg, (2012): 225-279.

[6] Liu, Dage, et al. "DNA nanotubes self-assembled from triple-crossover tiles as templates for conductive nanowires." Proceedings of the National Academy of Sciences of the United States of America 101.3 (2004): 717-722.

[7] Liu, Haipeng, et al. "Two-dimensional (2D) DNA crystals assembled from two DNA strands." Biomacromolecules 6.6 (2005): 2943-2945.

[8] Zheng, Jianping, et al. "From molecular to macroscopic via the rational design of a self-assembled 3D DNA crystal." Nature 461.7260 (2009): 74-77.

[9] Wei, Bryan, Mingjie Dai, and Peng Yin. "Complex shapes self-assembled from single-stranded DNA tiles." Nature 485.7400 (2012): 623-626.

[10] Maye, Mathew M., et al. "Stepwise surface encoding for high-throughput assembly of nanoclusters." Nature materials 8.5 (2009): 388-391.

[11] Maffeo, Christopher, Binquan Luan, and Aleksei Aksimentiev. "End-to-end attraction of duplex DNA." Nucleic acids research 40.9 (2012): 3812-3821.

[12] Bellini, Tommaso, et al. "Liquid crystal self-assembly of random-sequence DNA oligomers." Proceedings of the National Academy of Sciences 109.4 (2012): 1110-1115.

[13] Largo, Julio, Francis W. Starr, and Francesco Sciortino. "Self-assembling DNA dendrimers: A numerical study." Langmuir 23.11 (2007): 5896-5905.

[14] Russo, J., et al. "Reentrant phase diagram of network fluids." Physical review letters 106.8 (2011): 085703.

[15] Angioletti-Uberti, Stefano, Bortolo M. Mognetti, and Daan Frenkel. "Re-entrant melting as a design principle for DNA-coated colloids." Nature materials 11.6 (2012): 518-522.

[16] Bianchi, Emanuela, et al. "Phase diagram of patchy colloids: towards empty liquids." Physical review letters 97.16 (2006): 168301.

[17] Ruzicka, Barbara, et al. "Observation of empty liquids and equilibrium gels in a colloidal clay." Nature materials 10.1 (2010): 56-60.

[18] Zaccarelli, Emanuela. "Colloidal gels: Equilibrium and non-equilibrium routes." Journal of Physics: Condensed Matter 19.32 (2007): 323101.

[19] Zhang, Zhenli, and Sharon C. Glotzer. "Self-assembly of patchy particles." Nano Letters 4.8 (2004): 1407-1413.

[20] Frenkel, Daan. "Soft condensed matter." Physica A: Statistical Mechanics and its Applications 313.1 (2002): 1-31.

[21] Cipelletti, Luca, and Laurence Ramos. "Slow dynamics in glassy soft matter." Journal of Physics: Condensed Matter 17.6 (2005): R253.

[22] Likos, Christos N. "Soft matter with soft particles." Soft Matter 2.6 (2006): 478-498.

[23] Deraguin, B. V., and L. D. Landau. "Theory of the stability of strongly charged lyophobic sols and of the adhesion of strongly charged particles in solution of electrolytes." Acta Physicochim: USSR 14 (1941): 633-662.

[24] Asakura, Sho, and Fumio Oosawa. "Interaction between particles suspended in solutions of macromolecules." Journal of Polymer Science 33.126 (1958): 183-192.

[25] Sciortino, Francesco. "Gel-forming patchy colloids and network glass formers: thermodynamic and dynamic analogies." The European Physical Journal B 64.3-4 (2008): 505-509.

[26] Sun, Yugang, and Younan Xia. "Shape-controlled synthesis of gold and silver nanoparticles." Science 298.5601 (2002): 2176-2179.

[27] Roh, Kyung-Ho, David C. Martin, and Joerg Lahann. "Biphasic Janus particles with nanoscale anisotropy." Nature Materials 4.10 (2005): 759-763.

[28] Dendukuri, Dhananjay, et al. "Continuous-flow lithography for high-throughput microparticle synthesis." Nature materials 5.5 (2006): 365-369.

[29] Yin, Yadong, et al. "Template-assisted self-assembly: a practical route to complex aggregates of monodispersed colloids with well-defined sizes, shapes, and structures." Journal of the American Chemical Society 123.36 (2001): 8718-8729.

[30] Manoharan, Vinothan N., Mark T. Elsesser, and David J. Pine. "Dense packing and symmetry in small clusters of microspheres." Science 301.5632 (2003): 483-487.

[31] Lu, Yu, Yadong Yin, and Younan Xia. "Three-Dimensional Photonic Crystals with Non-spherical Colloids as Building Blocks." Advanced materials 13.6 (2001): 415-420.

[32] Liddell, Chekesha M., and Christopher J. Summers. "Monodispersed ZnS dimers, trimers, and tetramers for lower symmetry photonic crystal lattices." Advanced Materials 15.20 (2003): 1715-1719.

[33] Cho, Young-Sang, et al. "Self-organization of bidisperse colloids in water droplets." Journal of the American Chemical Society 127.45 (2005): 15968-15975.

[34] Glotzer, S. C., M. J. Solomon, and Nicholas A. Kotov. "Self-assembly: From nanoscale to microscale colloids." AIChE Journal 50.12 (2004): 2978-2985.

[35] Glotzer, Sharon C., and Michael J. Solomon. "Anisotropy of building blocks and their assembly into complex structures." Nature materials 6.8 (2007): 557-562.

[36] Bowden, Ned B., et al. "Molecule-mimetic chemistry and mesoscale self-assembly." Accounts of chemical research 34.3 (2001): 231-238.

[37] Zerrouki, Djamal, et al. "Preparation of doublet, triangular, and tetrahedral colloidal clusters by controlled emulsification." Langmuir 22.1 (2006): 57-62.

[38] Sciortino, Francesco, et al. "Routes to colloidal gel formation." Computer physics communications 169.1 (2005): 166-171.

[39] Sciortino, Francesco, and Piero Tartaglia. "Glassy colloidal systems." Advances in physics 54.6-7 (2005): 471-524.

[40] Zaccarelli, E., et al. "Model for reversible colloidal gelation." Physical review letters 94.21 (2005): 218301.

[41] Wilber, Alex W., et al. "Reversible self-assembly of patchy particles into monodisperse icosahedral clusters." The Journal of chemical physics 127.8 (2007): 085106-085106.

[42] Doye, Jonathan PK, et al. "Controlling crystallization and its absence: proteins, colloids and patchy models." Physical Chemistry Chemical Physics 9.18 (2007): 2197-2205.

[43] Hill T. L." An Introduction to Statistical Thermodynamics" (NewYork:Dover) 1987

[44] Cates, Michael E., et al. "Theory and simulation of gelation, arrest and yielding in attracting colloids." Journal of Physics: Condensed Matter 16.42 (2004): S4861.

[45] Charbonneau, P., and D. R. Reichman. "Systematic characterization of thermodynamic and dynamical phase behavior in systems with short-ranged attraction." Physical Review E 75.1 (2007): 011507.

[46] Hurtado, Pablo I., Ludovic Berthier, and Walter Kob. "Heterogeneous diffusion in a reversible gel." Physical review letters 98.13 (2007): 135503.

[47] Puertas, Antonio M., Matthias Fuchs, and Michael E. Cates. "Comparative simulation study of colloidal gels and glasses." Physical review letters 88.9 (2002): 098301.

[48] Liu, Y., and Ras B. Pandey. "Computer-simulation studies of kinetic gelation." Physical Review B 55.13 (1997): 8257.

[49] Del Gado, Emanuela, et al. "A unifying model for chemical and colloidal gels." EPL (Europhysics Letters) 63.1 (2003): 1.

[50] Del Gado, Emanuela, et al. "Slow dynamics in gelation phenomena: From chemical gels to colloidal glasses." Physical Review E 69.5 (2004): 051103.

[51] Saika-Voivod, I., et al. "Effect of bond lifetime on the dynamics of a short-range attractive colloidal system." Physical Review E 70.4 (2004): 041401.

[52] Zaccarelli, Emanuela, et al. "Activated bond-breaking processes preempt the observation of a sharp glass-glass transition in dense short-ranged attractive colloids." Physical review letters 91.10 (2003): 108301.

[53] Zaccarelli, Emanuela, Francesco Sciortino, and Piero Tartaglia. "Numerical study of the glass–glass transition in short-ranged attractive colloids." Journal of Physics: Condensed Matter 16.42 (2004): S4849.

[54] Kraft DJ, Groenewold J, Kegel WK. Colloidal molecules with well-controlled bond angles. Soft Matter 2009;5:3823–6.

[55] Zaccarelli, E., et al. "Model for reversible colloidal gelation." Physical review letters 94.21 (2005): 218301.

[56] Moreno, A. J., et al. "Energy landscape of a simple model for strong liquids." Physical review letters 95.15 (2005): 157802.

[57] Zaccarelli, Emanuela, et al. "Gel to glass transition in simulation of a valence-limited colloidal system." The Journal of chemical physics 124 (2006): 124908.

[58] Wertheim, M. S. "Fluids with highly directional attractive forces. I. Statistical thermodynamics." Journal of Statistical Physics 35.1-2 (1984): 19-34.

[59] Wertheim, M. S. "Fluids with highly directional attractive forces. IV. Equilibrium polymerization." Journal of Statistical Physics 42.3-4 (1986): 477-492.

[60] Sciortino, Francesco, and Emanuela Zaccarelli. "Reversible gels of patchy particles." Current Opinion in Solid State and Materials Science 15.6 (2011): 246-253.

[61] SantaLucia, John. "A unified view of polymer, dumbbell, and oligonucleotide DNA nearest-neighbor thermodynamics." Proceedings of the National Academy of Sciences 95.4 (1998): 1460-1465.

[62] SantaLucia Jr, John, and Donald Hicks. "The thermodynamics of DNA structural motifs." Annu. Rev. Biophys. Biomol. Struct. 33 (2004): 415-440.

[63] Manyanga, Fidelis, et al. "Origins of the “Nucleation” Free Energy in the Hybridization Thermodynamics of Short Duplex DNA†." The Journal of Physical Chemistry B 113.9 (2009): 2556-2563.

[64] Owczarzy, Richard, et al. "Effects of sodium ions on DNA duplex oligomers: improved predictions of melting temperatures." Biochemistry 43.12 (2004): 3537-3554.

[65] Yakovchuk, Peter, Ekaterina Protozanova, and Maxim D. Frank-Kamenetskii. "Base-stacking and base-pairing contributions into thermal stability of the DNA double helix." Nucleic acids research 34.2 (2006): 564-574.

[66] Seeman, Nadrian C. "Nanomaterials based on DNA." Annual review of biochemistry 79 (2010): 65.

[67] Um, Soong Ho, et al. "Dendrimer-like DNA-based fluorescence nanobarcodes." Nature Protocols 1.2 (2006): 995-1000.

[68] Li, Yougen, et al. "Controlled assembly of dendrimer-like DNA." Nature materials 3.1 (2003): 38-42.

[69] MLA Roh, Young Hoon, et al. "Engineering DNA-based functional materials." Chemical Society Reviews 40.12 (2011): 5730-5744.

[70] Alivisatos, A. Paul, et al. "Organization of'nanocrystal molecules' using DNA." (1996): 609-611.

[71] Zheng, Ming, et al. "Structure-based carbon nanotube sorting by sequence-dependent DNA assembly." Science 302.5650 (2003): 1545-1548.

[72] Niemeyer, Christof M., et al. "Oligonucleotide-directed self-assembly of proteins: semisynthetic DNA—streptavidin hybrid molecules as connectors for the generation of macroscopic arrays and the construction of supramolecular bioconjugates." Nucleic Acids Research 22.25 (1994): 5530-5539.

[73] Kallenbach, Neville R., Rong-Ine Ma, and Nadrian C. Seeman. "An immobile nucleic acid junction constructed from oligonucleotides." Nature 305 (1983): 829-831.

[74] Seeman, Nadrian C. "DNA nanotechnology: novel DNA constructions." Annual Review of Biophysics and Biomolecular Structure 27.1 (1998): 225-248.

[75] Wang, Xing, and Nadrian C. Seeman. "Assembly and characterization of 8-arm and 12-arm DNA branched junctions." Journal of the American Chemical Society 129.26 (2007): 8169-8176.

[76] Chen, Junghuei, and Nadrian C. Seeman. "Synthesis from DNA of a molecule with the connectivity of a cube." Nature 350.6319 (1991): 631-633.

[77] Zhang, Yuwen, and Nadrian C. Seeman. "Construction of a DNA-truncated octahedron." Journal of the American Chemical Society 116.5 (1994): 1661-1669.

[78] Li, Yougen, et al. "Controlled assembly of dendrimer-like DNA." Nature materials 3.1 (2003): 38-42.

[79] Nishikawa, Makiya, et al. "Enhanced immunostimulatory activity of oligodeoxynucleotides by Y-shape formation." Immunology 124.2 (2008): 247-255.

[80] Sa-Ardyen, Phiset, Alexander V. Vologodskii, and Nadrian C. Seeman. "The flexibility of DNA double crossover molecules." Biophysical journal 84.6 (2003): 3829-3837.

[81] Winfree, Erik, et al. "Design and self-assembly of two-dimensional DNA crystals." Nature 394.6693 (1998): 539-544.

[82] He, Yu, et al. "Self-assembly of hexagonal DNA two-dimensional (2D) arrays." Journal of the American Chemical Society 127.35 (2005): 12202-12203.

[83] Yan, Hao, et al. "DNA-templated self-assembly of protein arrays and highly conductive nanowires." Science 301.5641 (2003): 1882-1884.

[84] Zhang, Chuan, et al. "Conformational flexibility facilitates self-assembly of complex DNA nanostructures." Proceedings of the National Academy of Sciences 105.31 (2008): 10665-10669.

[85] He, Yu et al., “Sequence symmetry as a tool for designing DNA nanostructures.” Angew Chem Int Edit (2005), 44: 6694 – 6696.

[86] He, Yu, et al. "Hierarchical self-assembly of DNA into symmetric supramolecular polyhedra." Nature 452.7184 (2008): 198-201.

[87] Yan, Hao, et al. "Directed nucleation assembly of DNA tile complexes for barcode-patterned lattices." Proceedings of the National Academy of Sciences 100.14 (2003): 8103-8108.

[88] Rothemund, Paul WK. "Folding DNA to create nanoscale shapes and patterns." Nature 440.7082 (2006): 297-302.

[89] Andersen, Ebbe S., et al. "Self-assembly of a nanoscale DNA box with a controllable lid." Nature 459.7243 (2009): 73-76.

[90] Douglas, Shawn M., et al. "Self-assembly of DNA into nanoscale three-dimensional shapes." Nature 459.7245 (2009): 414-418.

[91] Han, Dongran, et al. "DNA origami with complex curvatures in three-dimensional space." Science 332.6027 (2011): 342-346.

[92] Um, Soong Ho, et al. "Enzyme-catalysed assembly of DNA hydrogel." Nature materials 5.10 (2006): 797-801.

[93] Park, Nokyoung, et al. "A cell-free protein-producing gel." Nature materials 8.5 (2009): 432-437.

[94] Elghanian, Robert, et al. "Selective colorimetric detection of polynucleotides based on the distance-dependent optical properties of gold nanoparticles." Science 277.5329 (1997): 1078-1081.

[95] Park, Sung Yong, et al. "DNA-programmable nanoparticle crystallization." Nature 451.7178 (2008): 553-556.

[96] Nykypanchuk, Dmytro, et al. "DNA-guided crystallization of colloidal nanoparticles." Nature 451.7178 (2008): 549-552.

[97] B.J. Berne and R. Pecora. “Dynamic light scattering”. Wiley, New York, 1976.

[98] P. Pusey. “Introduction to Scattering Experiments”. Elsevier Sciences B.V., 2002. in “Neutrons, X-rays and Light: Scattering methods applied to Soft Condensed Matter”, P. Lindner and T. Zemb eds.

[99] H. Eugene Stenley. Introduction to Phase transitions and Critical Phenomena”. Oxford University Press, New York, 1987.

[100] Tataurov, Andrey V., Yong You, and Richard Owczarzy. "Predicting ultraviolet spectrum of single stranded and double stranded deoxyribonucleic acids." Biophysical chemistry 133.1 (2008): 66-70.

[101] Thomas, René. "The denaturation of DNA." Gene 135.1 (1993): 77-79.

[102] Mergny, Jean-Louis, and Laurent Lacroix. "Analysis of thermal melting curves." Oligonucleotides 13.6 (2003): 515-537.

[103] P. Eaton and P. West. “Atomic Force Microcopy”. Oxford Univ Press (Txt), 2010

[104] Binnig, Gerd, et al. "Surface studies by scanning tunneling microscopy." Physical Review Letters 49. (1982): 57–61

[105] Binnig, Gerd, Calvin F. Quate, and Ch Gerber. "Atomic force microscope." Physical Review Letters 56.9 (1986): 930.

[106] Lyubchenko, Yuri, et al. "Atomic force microscopy of long DNA: imaging in air and under water." Proceedings of the National Academy of Sciences 90.6 (1993): 2137-2140.

[107] Hansma, Helen G. "Surface biology of DNA by atomic force microscopy." Annual review of physical chemistry 52.1 (2001): 71-92.

[108] Lyubchenko, Yuri L. "DNA structure and dynamics." Cell biochemistry and biophysics 41.1 (2004): 75-98.

[109] Hamon, Loïc, et al. "High-resolution AFM imaging of single-stranded DNA-binding (SSB) protein—DNA complexes." Nucleic acids research 35.8 (2007): e58.

[110] Cheng, Hao, et al. "Polynucleotide adsorption to negatively charged surfaces in divalent salt solutions." Biophysical journal 90.4 (2006): 1164-1174.

[111] Mizuno, Rika, et al. "Synthesis and AFM visualization of DNA nanostructures." Thin solid films 464 (2004): 459-463.

[112] He, Yu, et al. "Hierarchical self-assembly of DNA into symmetric supramolecular polyhedra." Nature 452.7184 (2008): 198-201.

[113] Rippe, Karsten, Norbert Mücke, and Jörg Langowski. "Superhelix dimensions of a 1868 base pair plasmid determined by scanning force microscopy in air and in aqueous solution." Nucleic acids research 25.9 (1997): 1736-1744.

[114] Biffi, Silvia, et al. "Phase behavior and critical activated dynamics of limited-valence DNA nanostars." Proceedings of the National Academy of Sciences 110.39 (2013): 15633-15637.

[115] Pelissetto, Andrea, and Ettore Vicari. "Critical phenomena and renormalization-group theory." Physics Reports 368.6 (2002): 549-727.

[116] K. Binder and W. Kob, Glassy Materials And Disordered Solids: An Introduction to Their Statistical Mechanics (World Scientific Publishing Company, 2005).

[117] A. Coniglio and W. Klein. Clusters and Ising Critical Droplets: A Renormalization Group Approach, J. Phys. A 13: 2775, 1980

[118] Tanaka, Hajime, Yohei Nakanishi, and Naoko Takubo. "Nonuniversal nature of dynamic critical anomaly in polymer solutions." Physical Review E 65.2 (2002): 021802.

[119] Kostko, A. F., M. A. Anisimov, and J. V. Sengers. "Dynamic crossover to tricriticality and anomalous slowdown of critical fluctuations by entanglements in polymer solutions." Physical Review E 66.2 (2002): 020803.

[120] Roldan-Vargas, Sandalo, et al. "Gelling by Heating." arXiv preprint arXiv:1303.2582 (2013).

[121] Smallenburg, Frank, and Francesco Sciortino. "Liquids more stable than crystals in particles with limited valence and flexible bonds." Nature Physics 9.9 (2013): 554-558.

List of Publications

1. Bomboi, F, Bonincontro A., La Mesa C., Tardani F. "Interactions between single-walled carbon nanotubes and lysozyme." Journal of colloid and interface science 355.2 (2011): 342-347.

2. Biffi, S. , Cerbino, R. Bomboi, F., Paraboschi, E. M., Asselta, R., Sciortino, F., Bellini, T. "Phase behavior and critical activated dynamics of limited-valence DNA nanostars." Proceedings of the National Academy of Sciences 110.39 (2013): 15633-15637.

3. Bomboi, F., Tardani F., Gazzoli, D., Bonincontro A., La Mesa, C. "Lysozyme binds onto functionalized carbon nanotubes." Colloids and Surfaces B: Biointerfaces (2013).

4. Amaduzzi, F., Bomboi, F., Bonincontro, A., Bordi F., Casciardi, S., Chronopoulou, L., Diociaiuti, M., Mura, F., Palocci C., Sennato S. "Chitosan–DNA complexes: Charge inversion and DNA condensation." Colloids and Surfaces B: Biointerfaces 114 (2014): 1-10.

5. Bordi, F., Chronopoulou, L., Palocci, C., Bomboi, F., Di Nitto, A., Ascenzioni, F., Sennato, S. “Chitosan-DNA complexes: effect of molecular parameters on the efficiency of delivery.” Colloids and Surfaces A: Physicochemical and Engineering Aspects, in press.

6. L. Rovigatti, F. Bomboi and F. Sciortino, “Accurate phase diagram of tetravalent DNA nanostars”, ready for submission.